



Max-Planck-Institut für Metallforschung
Stuttgart

Thermodynamic and Kinetic Studies on the Thermal Stability of Amorphous Si-(B-)C-N Ceramics

Amir Hossein Tavakoli

Dissertation
an der
Universität Stuttgart

Bericht Nr. 229
Oktober 2010

Thermodynamic and Kinetic Studies on the Thermal Stability of Amorphous Si-(B-)C-N Ceramics

**Von der Fakultät Chemie der Universität Stuttgart
zur Erlangung der Würde eines Doktors der Naturwissenschaften (Dr. rer. nat.)
genehmigte Abhandlung**

vorgelegt von

Amir Hossein Tavakoli

aus Teheran/Iran

Hauptberichter: Prof. Dr. J. Bill
Mitberichter: Prof. Dr. G. D. Sorarù
Prüfungsvorsitzender: Prof. Dr. E. J. Mittemeijer

Tag der mündlichen Prüfung: 01.10.2010

**INSTITUT FÜR MATERIALWISSENSCHAFT DER UNIVERSITÄT STUTTGART
MAX-PLANCK-INSTITUT FÜR METALLFORSCHUNG IN STUTTGART**

Stuttgart, 2010

Table of contents

1. General Introduction	7
1.1. Thermal stability of Si-(B-)C-N ceramics	7
1.2. Thermodynamic analysis	8
1.3. Mass loss during annealing	17
1.4. Structural transformations induced by annealing	19
1.5. Outline of the thesis	23
References	25
2. Effect of boron on the crystallization of amorphous Si-(B-)C-N polymer-derived ceramics	29
2.1. Introduction	30
2.2. Experimental procedures	31
2.2.1. Precursors synthesis, thermolysis, and post-annealing	31
2.2.2. Measurement techniques	32
2.3. Thermodynamic modeling	32
2.3.1. Amorphous phase “am-SiCN”	32
2.3.2. Crystallization	34
2.4. Results	35
2.4.1. Characteristics of the as-obtained ceramics	35
2.4.2. Crystallization	36
2.4.3. Thermodynamic computations	40
2.5. Discussion	42
2.6. Summary and conclusions	47
Acknowledgements	48
References	49
3. Quantitative XRD analysis and modeling of crystallization Process in amorphous Si-B-C-N polymer-derived ceramics	53
3.1. Introduction	54
3.2. Experimental Procedures	55
3.2.1. Precursor synthesis, thermolysis, and post-annealing	55

3.2.2. Chemical and thermal analysis	56
3.2.3. X-ray diffraction analysis	56
3.3. Modeling of metastable phase equilibria	57
3.3.1. Amorphous phase “am-SiCN”	57
3.3.2. Nanocrystalline phases (NC-SiC, NC-Si ₃ N ₄)	58
3.4. Results and Discussion	60
3.4.1. Thermal stability of the as-thermolyzed ceramics	60
3.4.2. Isochronal investigation of structural evolution	62
3.4.3. Metastable phase fraction diagrams	67
3.4.4. Discussion on the consistency of experimental analysis and modeling	72
3.5. Summary and Conclusions	74
Acknowledgements	75
References	76
4. Crystallization kinetics of Si₃N₄ in Si–B–C–N polymer-derived ceramics	79
4.1. Introduction	80
4.2. Experimental Procedures	81
4.2.1. General remarks	81
4.2.2. X-ray diffraction analysis	82
4.2.3. TEM investigations	82
4.3. Results and Discussion	83
4.3.1. Course of crystallization	83
4.3.1.1. Growing amount of crystalline Si ₃ N ₄	83
4.3.1.2. Growth of crystallite dimensions	85
4.3.2. Kinetic analysis of crystallization	89
4.4. Discussion	92
4.5. Summary and conclusions	96
Acknowledgements	97
References	97
5. Kinetic effect of boron on the crystallization of Si₃N₄ in Si–B–C–N polymer-derived ceramics	101
5.1. Introduction	102

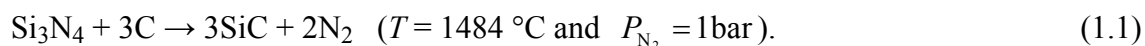
5.2. Experimental procedures	103
5.2.1. General remarks	103
5.2.2. X-ray diffraction analysis	103
5.3. Results	104
5.3.1. Course of crystallization	104
5.3.1.1. Growing amount of crystalline Si ₃ N ₄	104
5.3.1.2. Crystallite size analysis	108
5.3.2. Kinetic analysis of crystallization	110
5.4. Discussion	114
5.5. Summary and conclusions	118
Acknowledgements	120
References	120
6. Kinetic effect of boron on the thermal stability of Si-(B-)C-N	
polymer-derived ceramics	123
6.1. Introduction	124
6.2. Experimental Procedures	126
6.2.1. Precursors synthesis and thermolysis	126
6.2.2. Measurement techniques	126
6.2.2.1. Chemical composition	126
6.2.2.2. Mass loss measurements	126
6.2.2.3. Microstructure examination	127
6.3. Results and analysis	127
6.3.1. Characteristics of the as-thermolyzed ceramics	127
6.3.2. Phase equilibria and reactions expected	
during thermal treatment	128
6.3.3. Course of isothermal Si ₃ N ₄ degradation	129
6.3.3.1. Isothermal mass loss	130
6.3.3.2. Structural transformations	131
6.3.4. Kinetic analysis of the Si ₃ N ₄ degradation	133
6.4. Discussion	137
6.5. Summary and conclusions	141
Acknowledgements	142

References	142
7. Summary	145
7.1. Introduction	145
7.2. Thermodynamic calculations	147
7.3. Experimental procedures	147
7.4. Results and discussion	148
8. Zusammenfassung	153
8.1. Einleitung	153
8.2. Thermodynamische Berechnungen	155
8.3. Experimentaltteil	156
8.4. Ergebnisse und Diskussion	156
Acknowledgements	163
List of publications	165
Curriculum Vitae	167

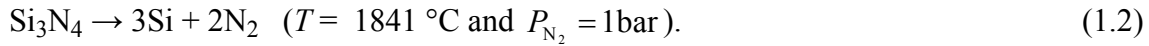
General Introduction

1.1. Thermal stability of Si–(B–)C–N ceramics

Si–(B–)C–N precursor-derived ceramics (PDCs) reveal well known unique structural features of glass-like, near ordered and/or nanocrystalline character. The most significant property of these materials is their extraordinary thermal stability which usually do not show essential mass loss during annealing up to 1600 °C and outstanding representatives withstand at temperatures above 2000°C without essential sign of decomposition. Moreover, Si₃N₄ is observed in these materials even at temperatures above 1841°C (decomposition temperature of Si₃N₄) [1-9]. In addition, these materials are distinguished by relatively high crystallization temperatures (for Si–C–N ceramics above 1400 °C and in the case of Si–B–C–N ceramics even higher) that considerably exceed the known crystallization temperatures of amorphous SiC ($T_{cr} \sim 1000$ °C) [10] and Si₃N₄ ($T_{cr} \sim 1200$ °C) [11]. These observations are really striking taking into account that the thermal stability of the Si–C–N PDCs of compositions located generally within the range of the ternary phase equilibrium SiC-Si₃N₄-C in the Si–C–N system should be essentially limited by the reaction of Si₃N₄ with carbon [12]:



An enhancement of the thermal stability of Si–C–N PDCs can be expected due to use of particular polymer precursors thermolyzed to compositions containing only SiC and Si₃N₄ [13]. In such a case, because of missing free carbon, the thermal decomposition of Si₃N₄ should determine the stability of the composite material [12]:



Actually much more significant improvement of the thermal stability has been achieved by modification of Si–C–N PDCs with boron. Thus Si–B–C–N PDCs can be regarded as high performance ceramics with potential applications as bulk materials, coatings, and fibers (see e.g. [1,3,8,14-22]). Various routes for the synthesis of proper precursors have been reported during the last two decades in order to prepare ceramics with high thermal stability against degradation (see Table 1.1).

In the following section (1.2), the thermodynamic computations of phase equilibria corresponding to Si–(B–)C–N systems are shown to clarify predicted phase changes during thermal treatment. Afterward in section 1.3, the available experimental data are reviewed to reveal factors affecting mass loss during annealing. To provide better insight into the phase evolution in these materials, information about structural transformations accompanying annealing are presented in section 1.4. The outline of the present Ph.D. thesis is given in the last section (1.5).

1.2. Thermodynamic analysis

Thermodynamic analysis comprehends computations of phase equilibria which could rationalize structural changes in consequence of thermal treatment. Recent development of the CALculation of PHase Diagrams (CALPHAD) method [41] allows such analysis also in the case of multi-component systems like Si–B–C–N PDCs. The corresponding phase diagrams have been computed using the Thermo-Calc software [42] together with the thermodynamic descriptions assessed for stable phases in this system [43]. Fig. 1.1 shows calculated phase equilibria of isothermal sections in the ternary Si–C–N system. In these diagrams the reaction paths (arrows) are indicated for ceramics with different C/Si ratios. According to these computations, the Si_3N_4 should disintegrate by an invariant reaction with carbon at the temperature $T = 1484 \text{ }^\circ\text{C}$ and decompose at $T = 1841 \text{ }^\circ\text{C}$ (Eqs. (1.1) and (1.2)). In connection with the reaction (1.1), all PDCs with a ratio $\text{C/Si} > 1$ decompose at $1484 \text{ }^\circ\text{C}$ into graphite and silicon carbide with simultaneous loss of mass due to release of nitrogen. In contrary the PDCs with a

Table 1.1. Investigated Si-B-C-N PDCs for assessment of the thermal stability

No.	Procedure of precursor preparation	Theoretical formula of as-obtained precursor	Thermolysis condition (temp., time, atmosphere)	Empirical formula of as-obtained ceramic	Max. Temp. of stability	Ref.
1	Modification of polyhydridopolysilazane with borazine	$\text{Si}_{1,0}\text{B}_{0,4}\text{C}_{1,0}\text{N}_{1,2}\text{H}_{4,7}$	1400 °C, 1h, Ar	$\text{Si}_{2,3}\text{B}_{0,5}\text{C}_{1,0}\text{N}_{2,9}$	~ 1500 °C	6,24
2		$\text{Si}_{1,0}\text{B}_{1,7}\text{C}_{1,0}\text{N}_{2,6}\text{H}_{6,2}$		$\text{Si}_{1,9}\text{B}_{2,6}\text{C}_{4,8}\text{N}_{4,8}$	~ 1750 °C	
3	Synthesis of the single-source precursor ($\text{C}_3\text{Si-NH-BCl}_2$) followed by ammonolysis of the as-obtained monomer with methylamines	(6.2 wt.% B)	1450 °C, 4h, Ar	(9.6 wt.%)	1000-1900 °C	7,25, 26
4	Hydroboration of dichloromethylvinylsilane followed by ammonolysis of the as-obtained monomer	$\text{Si}_{3,0}\text{B}_{1,0}\text{C}_{8,2}\text{N}_{2,0}\text{H}_{2,0}$	1000 °C, 1h, Ar	$\text{Si}_{3,0}\text{B}_{1,0}\text{C}_{4,3}\text{N}_{2,0}$	~ 2000 °C	8,14, 27
5	Hydroboration of dichloromethylvinylsilane followed by ammonolysis of the as-obtained monomers and dichloromethylvinylsilane	(2.2 wt.% B)		(3.1 wt.% B)	~ 1600 °C	
6	Hydroboration of dichloromethylvinylsilane followed by ammonolysis of the as-obtained monomers and further hydroboration subsequently	(14.2 wt.% B)	1000 °C, 1h, Ar	(16.3 wt.% B)	~ 1700 °C	14, 27
7	Ammonolysis of dichlorovinylsilane followed by hydroboration of the as-obtained polymer	(15.7 wt.% B)		(18 wt.% B)	~ 1500 °C	
8		$\text{Si}_{3,0}\text{B}_{1,0}\text{C}_{9,0}\text{N}_{6,0}\text{H}_{1,5}$		---	~ 1600 °C	
9	Hydroboration of vinyl-substituted polysilylcarbodi-imide	$\text{Si}_{3,0}\text{B}_{1,0}\text{C}_{12,0}\text{N}_{6,0}\text{H}_{2,1}$	1100 °C, ---, Ar	---		28, 29
10		$\text{Si}_{3,0}\text{B}_{1,0}\text{C}_{10,5}\text{N}_{9,0}\text{H}_{1,2}$		---	~ 1500 °C	
11	Synthesis of the single-source precursor (1-(trichlorosilyl)-1-(dichloroboryl)ethane) followed by ammonolysis of the as-obtained monomers with methylamines	---	1500 °C, 3h, N_2	(15.3 wt.%)	1200-2000 °C	30

(continued)

Table 1.1. Investigated Si–B–C–N PDCs for assessment of the thermal stability

No.	Procedure of precursor preparation	Theoretical formula of as-obtained precursor	Thermolysis condition (temp., time, atmosphere)	Empirical formula of as-obtained ceramic	Max. Temp. of stability	Ref.
12	Ammonolysis of $\{B[C_2H_4SiHCl_2]_3\}_n$	$Si_{3,0}B_{1,1}C_{6,5}N_{3,0}H_{20}$		$Si_{3,0}B_{1,2}C_{4,9}N_{3,1}$	~ 1980 °C	
13	Hydroboration of $\{B[C_2H_4Si(H)NH]_3\}_n$	$Si_{3,0}B_{1,1}C_{6,2}N_{3,2}H_{18}$	1100 °C, 3h, Ar	$Si_{3,0}B_{1,1}C_{5,3}N_{3,0}$		18
14	Hydroboration of $\{B[C_2H_4Si(H)(NH)]_{1,5}\}_n$	$Si_{3,0}B_{1,1}C_{6,2}N_{4,3}H_{17}$		$Si_{3,0}B_{1,1}C_{3,0}N_{4,0}$	~ 1450 °C	
15		$Si_{1,0}B_{0,1}C_{3,0}N_{1,0}H_{6,4}$		$Si_{1,0}B_{0,1}C_{1,5}N_{1,0}$	~ 1650 °C	
16		$Si_{1,0}B_{0,2}C_{3,2}N_{1,1}H_{7,6}$		$Si_{1,0}B_{0,2}C_{1,6}N_{1,0}$	≥ 1650 °C	20
17	Ammonolysis of dichloromethylvinylsilane followed by hydroboration of the as-obtained polymer	$Si_{1,0}B_{0,3}C_{3,0}N_{1,0}H_{7,3}$	1400 °C, 2h, Ar	$Si_{1,0}B_{0,3}C_{1,7}N_{1,0}$		
18		$Si_{1,0}B_{0,4}C_{3,1}N_{1,0}H_{7,6}$		$Si_{1,0}B_{0,4}C_{1,7}N_{1,0}$	~ 1900 °C	
19		$Si_{1,0}B_{0,1}C_{2,0}N_{0,9}H_{5,3}$		$Si_{1,0}B_{0,1}C_{1,6}N_{1,0}$	~ 1630 °C	
20		$Si_{1,0}B_{0,2}C_{2,1}N_{1,1}H_{5,8}$		$Si_{1,0}B_{0,2}C_{1,6}N_{1,0}$	~ 1670 °C	
21	Ammonolysis of dichlorovinylsilane followed by hydroboration of the as-obtained polymer	$Si_{1,0}B_{0,3}C_{1,9}N_{1,1}H_{5,9}$	1400 °C, 2h, Ar	$Si_{1,0}B_{0,3}C_{1,6}N_{1,0}$	~ 1700 °C	31
22		$Si_{1,0}B_{0,4}C_{2,0}N_{1,0}H_{6,4}$		$Si_{1,0}B_{0,4}C_{1,6}N_{1,1}$	≥ 1700 °C	

(continued)

Table 1.1. Investigated Si–B–C–N PDCs for assessment of the thermal stability

No.	Procedure of precursor preparation	Theoretical formula of as-obtained precursor	Thermolysis condition (temp., time, atmosphere)	Empirical formula of as-obtained ceramic	Max. Temp. of stability	Ref.
23	Hydroboration of dichlorophenylvinylsilane followed by ammonolysis of the as-obtained monomers	$\text{Si}_{2,7}\text{B}_{1,0}\text{C}_{23,0}\text{N}_{3,0}\text{H}_{32,0}$		$\text{Si}_{2,9}\text{B}_{1,0}\text{C}_{14,0}\text{N}_{2,9}$		
24	Hydroboration of dichlorophenylvinylsilane followed by ammonolysis of the as-obtained monomers and subsequent dehydrocoupling reaction in the presence of phenylsilane	$\text{Si}_{3,9}\text{B}_{1,0}\text{C}_{15,0}\text{N}_{3,1}\text{H}_{28,0}$	1050 °C, 4h, Ar	$\text{Si}_{3,9}\text{B}_{1,0}\text{C}_{11,0}\text{N}_{3,2}$	2000-2200 °C	32
25	Similar to precursor No. 20 but using different solvent during ammonolysis	$\text{Si}_{5,7}\text{B}_{1,0}\text{C}_{25,0}\text{N}_{2,9}\text{H}_{36,0}$		$\text{Si}_{5,3}\text{B}_{1,0}\text{C}_{19,0}\text{N}_{3,4}$		
26	Ammonolysis of dichlorodivinylsilane followed by hydroboration of the as-obtained oligomer	$\text{Si}_{1,9}\text{B}_{1,2}\text{C}_{7,5}\text{N}_{1,9}\text{H}_{1,55}$		$\text{Si}_{1,9}\text{B}_{1,3}\text{C}_{4,9}\text{N}_{1,9}$	~ 1800 °C	
27	Polymerization of dichlorodivinylsilane with cyanamide followed by hydroboration of the as-obtained polymer	$\text{Si}_{1,5}\text{B}_{1,0}\text{C}_{7,2}\text{N}_{2,9}\text{H}_{1,21}$		$\text{Si}_{1,5}\text{B}_{1,0}\text{C}_{4,8}\text{N}_{2,7}$	~ 1420 °C	
28	Ammonolysis of chlorotrivinylsilane followed by hydroboration of the as-obtained polymer	$\text{Si}_{1,3}\text{B}_{1,6}\text{C}_{10,1}\text{N}_{2,9}\text{H}_{2,12}$	1400 °C, ---, Ar	$\text{Si}_{1,3}\text{B}_{1,6}\text{C}_{5,7}\text{N}_{1,4}$		33, 34
29	Synthesis of bis(trivinylsilyl)amine from trivinylsilylamine followed by hydroboration of the as-obtained material	$\text{Si}_{1,5}\text{B}_{1,5}\text{C}_{9,1}\text{N}_{8,1}\text{H}_{1,81}$		$\text{Si}_{1,5}\text{B}_{1,4}\text{C}_{6,3}\text{N}_{8}$	2000-2150 °C	
30	Polymerization of chlorotrivinylsilane with cyanamide followed by hydroboration of the as-obtained polymer	$\text{Si}_{1,3}\text{B}_{1,3}\text{C}_{8,6}\text{N}_{1,3}\text{H}_{1,57}$		$\text{Si}_{1,3}\text{B}_{1,3}\text{C}_{6,0}\text{N}_{1,3}$		
31	Hydroboration of allyldichloromethylsilane followed by ammonolysis of the as-obtained monomers	$\text{Si}_{3,0}\text{B}_{1,3}\text{C}_{13,8}\text{N}_{3,3}\text{H}_{3,5,6}$		$\text{Si}_{2,2}\text{B}_{9,47}\text{N}_{2,1}$	~ 1800 °C	
32	Precursor 31 with using THF solvent and less reaction temperature and time	$\text{Si}_{3,0}\text{B}_{1,1}\text{C}_{13,4}\text{N}_{3,0}\text{H}_{3,3,3}$	1400 °C, ---, Ar	$\text{Si}_{2,1}\text{B}_{1,0}\text{C}_{4,9}\text{N}_{2,0}$		35
33	ammonolysis of allyldichloromethylsilane followed by hydroboration of the as-obtained polymer	$\text{Si}_{3,0}\text{B}_{1,1}\text{C}_{13,8}\text{N}_{3,6}\text{H}_{3,2}$		$\text{Si}_{2,4}\text{B}_{8,45}\text{N}_{2,3}$	~ 2000 °C	

(continued)

Table 1.1. Investigated Si-B-C-N PDCs for assessment of the thermal stability

No.	Procedure of precursor preparation	Theoretical formula of as-obtained precursor	Thermolysis condition (temp., time, atmosphere)	Empirical formula of as-obtained ceramic	Max. Temp. of stability	Ref.
34	Hydroboration of dichloromethylvinylsilane followed by ammonolysis of the as-obtained monomers	$\text{Si}_{12,7}\text{B}_{1,0}\text{C}_{9,1}\text{N}_{3,1}\text{H}_{22,0}$	1700 °C, 4h, Ar	$\text{Si}_{2,7}\text{B}_{1,0}\text{C}_{5,1}\text{N}_{2,5}$	~ 2000 °C	36
35			25-1050 °C, NH_3 , 1050 °C, 4h, NH_3 ; 1050 °C, 4h, Ar	$\text{Si}_{2,3}\text{B}_{1,0}\text{C}_{0,3}\text{N}_{3,6}$	~ 1600 °C	
36		$\text{Si}_{6,0}\text{B}_{1,1}\text{C}_{10,1}\text{N}_{3,6}\text{H}_{35,3}$		$\text{Si}_{6,0}\text{B}_{1,1}\text{C}_{10,0}\text{N}_{3,4}$	~ 1850 °C	
37	Thermally induced hydroboration of oligovinylsilane with tris(hydrodicosilyl)borane	$\text{Si}_{6,0}\text{B}_{1,1}\text{C}_{14,0}\text{N}_{3,3}\text{H}_{42,6}$	1400 °C, 2h, Ar	$\text{Si}_{6,0}\text{B}_{1,2}\text{C}_{11,5}\text{N}_{3,2}$	~ 2000 °C	18
38		$\text{Si}_{6,0}\text{B}_{1,0}\text{C}_{18,8}\text{N}_{4,1}\text{H}_{47,4}$		$\text{Si}_{6,0}\text{B}_{1,4}\text{C}_{10,3}\text{N}_{5,3}$	~ 1450 °C	
39		$\text{Si}_{3,0}\text{B}_{1,0}\text{C}_{6,5}\text{N}_{1,0}\text{H}_{20,0}$		---		
40		$\text{Si}_{3,0}\text{B}_{1,0}\text{C}_{7,0}\text{N}_{2,0}\text{H}_{19,0}$		---	1950-2000 °C	
41	Dehydrocoupling reaction of tri(hydrodicosilyl)ethylborane and cyanamide	$\text{Si}_{3,0}\text{B}_{1,0}\text{C}_{7,5}\text{N}_{3,0}\text{H}_{18,0}$	1400 °C, 3h, Ar	---	~ 1720 °C	37
42				$\text{Si}_{3,0}\text{B}_{1,0}\text{C}_{8,0}\text{N}_{4,0}\text{H}_{17,0}$	---	
43		$\text{Si}_{3,0}\text{B}_{1,0}\text{C}_{8,5}\text{N}_{5,0}\text{H}_{16,0}$		---	~ 1670 °C	
44		$\text{Si}_{3,0}\text{B}_{1,0}\text{C}_{9,0}\text{N}_{6,0}\text{H}_{15,0}$		---		

(continued)

Table 1.1. Investigated Si–B–C–N PDCs for assessment of the thermal stability

No.	Procedure of precursor preparation	Theoretical formula of as-obtained precursor	Thermolysis condition (temp., time, atmosphere)	Empirical formula of as-obtained ceramic	Max. Temp. of stability	Ref.
45	Wurtz-type coupling and subsequent ammonolysis of 1,3-dichloro-1,3-dimethyldisilazane with dichloromethylsilane followed by hydroboration of the as-obtained polymer	$\text{Si}_{1,0}\text{B}_{0,4}\text{C}_{1,1}\text{N}_{0,5}\text{H}_{4,2}$		$\text{Si}_{1,0}\text{B}_{0,4}\text{C}_{1,0}\text{N}_{0,6}$	1800-2000 °C	
46		$\text{Si}_{1,0}\text{B}_{0,5}\text{C}_{1,1}\text{N}_{0,6}\text{H}_{4,1}$	1450 °C, ---, Ar	$\text{Si}_{1,0}\text{B}_{0,6}\text{C}_{0,9}\text{N}_{0,7}$	~ 1500 °C	38
47	Wurtz-type coupling and subsequent ammonolysis of 1,3-dichloro-1,3-dimethyldisilazane with dichlorosilane followed by hydroboration of the as-obtained polymer	$\text{Si}_{1,0}\text{B}_{0,5}\text{C}_{0,7}\text{N}_{0,9}\text{H}_{3,2}$		$\text{Si}_{1,0}\text{B}_{0,5}\text{C}_{0,7}\text{N}_{1,0}$	~ 1800 °C	
48	Gas-to gel transformation of polymeric $\text{Si}_{3,0}\text{B}_{1,0}\text{C}_{10,0}\text{N}_{3,7}\text{H}_{50}$ waste gas followed by dehydrocoupling reaction with phenylsilane	$\text{Si}_{4,8}\text{B}_{1,0}\text{C}_{21,0}\text{N}_{3,5}\text{H}_{36}$	1050 °C, 4h, Ar	$\text{Si}_{5,3}\text{B}_{1,0}\text{C}_{19,0}\text{N}_{3,7}$	2000-2200 °C	39
49	Hydroboration of dichloromethylvinylsilane followed by aminolysis of the as-obtained monomers	$\text{Si}_{3,0}\text{B}_{1,0}\text{C}_{14,5}\text{N}_{4,4}\text{H}_{36,3}$	25-200 °C (curing): 1000 °C, 0.5h, N ₂ ; 1400 °C, 2h, Ar	$\text{Si}_{3,0}\text{B}_{1,0}\text{C}_{5,0}\text{N}_{2,4}$	~ 1700 °C	23
50		$\text{Si}_{1,0}\text{B}_{0,7}\text{C}_{3,2}\text{N}_{0,8}\text{H}_{6,1}$		$\text{Si}_{1,0}\text{B}_{0,7}\text{C}_{2,9}\text{N}_{0,7}$	~ 1800 °C	
51	Reaction of poly[1, 2-ethynediyl-(methylsilylene)] with borazine	$\text{Si}_{1,0}\text{B}_{1,2}\text{C}_{3,0}\text{N}_{1,3}\text{H}_{6,5}$	1400 °C, 2h, Ar	$\text{Si}_{1,0}\text{B}_{1,2}\text{C}_{2,7}\text{N}_{1,3}$	~ 1500 °C	40
52		$\text{Si}_{1,0}\text{B}_{1,2}\text{C}_{3,0}\text{N}_{1,3}\text{H}_{6,5}$		$\text{Si}_{1,0}\text{B}_{3,0}\text{C}_{2,8}\text{N}_{3,0}$	~ 1600 °C	

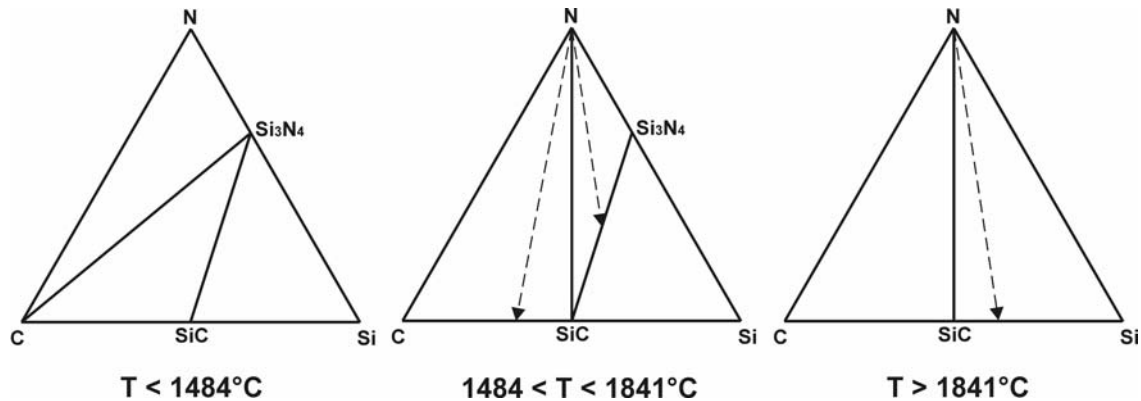


Fig. 1.1. Isothermal sections in the Si-C-N system. The reaction paths are indicated for PDCs with ratios $C/\text{Si} > 1$ and $C/\text{Si} < 1$ separately [43].

ratio $C/\text{Si} < 1$ decompose at this temperature into SiC and Si_3N_4 under release of nitrogen and subsequently, residual Si_3N_4 decomposes into liquid silicon and nitrogen gas according to the reaction (1.2). Phase compositions and quantitative mass balance along these reaction paths can be analysed by means of phase fraction diagrams. Examples of such diagrams computed for a PDC with the ratio $C/\text{Si} = 1.6$ and 34 at.% of nitrogen corresponding to polyvinylsilazane (VT50, Hoechst AG, Germany), and the ratio $C/\text{Si} = 0.90$ and 17 at.% of nitrogen corresponding to polyhydridomethylsilazane (NCP200, Nichimen Corp., Japan) are presented in Fig. 1.2(a) and Fig. 1.2(b), respectively.

Considering Si-B-C-N PDCs, it should be mentioned that thermodynamic computations for the Si-B-C-N system can hardly account for an apparent effect of boron on the thermal stability. Because in this case, experimentally observed domains (see section 1.4 for more information) are considered to be composed of boron nitride (BN) and graphite (C) as separated phases and moreover BN and Si_3N_4 are treated as non-interacting phases. According to these thermodynamic computations, boron does not affect either the temperature of disintegration of Si_3N_4 by reaction with carbon, or the decomposition temperature of Si_3N_4 . This is demonstrated by the phase fractions displayed in Fig. 1.3 which has been computed for boron containing ceramics. Fig. 1.3(a) represents a ceramic with the ratio $C/\text{Si} = 1.6$, 10 at.% of boron and 24 at.% of

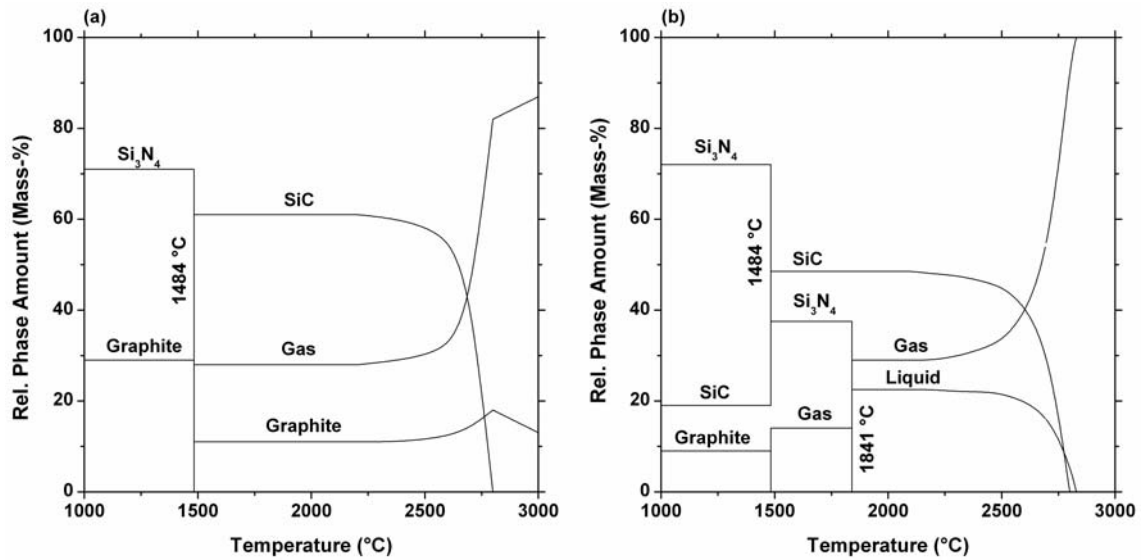


Fig. 1.2. Phase fraction diagrams computed for Si-C-N ceramics with ratios $C/Si = 1.6$ (a) and $C/Si = 0.9$ (b).

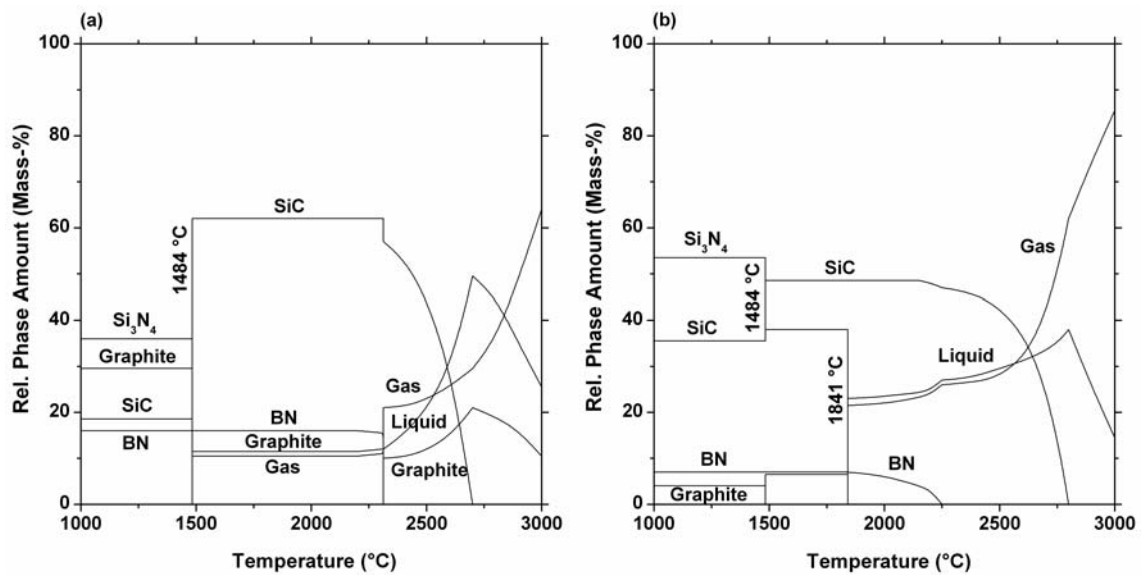


Fig. 1.3. Phase fraction diagrams computed for two Si-B-C-N ceramics with the ratio $C/Si = 1.6$ and 10 at.% of boron (a), and with the ratio $C/Si = 0.9$ and 5 at. % of boron (b).

nitrogen whereas Fig. 1.3(b) represents a ceramic with the ratio $C/Si = 0.9$, 5 at.% of boron and 12 at. % of nitrogen. However, looking at the microstructure of the high temperature stable SiBCN PDCs (Fig. 1.4), an ‘encapsulation effect’ has been assumed. Accordingly, silicon nitride grains are encapsulated with B-N-C turbostratic layers,

which act as a diffusion barrier and thus cause an effective increase of the partial pressure of nitrogen in the vicinity of Si_3N_4 . Considering Eq. (1.1), Si_3N_4 is stabilized against decomposition by this effect [12,19]. A further factor affecting the thermal stability is the decrease of the carbon activity according to the dissolution of carbon in the B–N–C layers [12,43]. Results of the thermodynamic computation presented in form of an activity versus temperature diagram quantify these effects on the phase equilibria, as shown in Fig. 1.5. At a nitrogen partial pressure of 1 bar the reaction temperature (reaction (1.1)) increases from 1484 °C at an activity $a(\text{C}) = 1$ to 1841 °C at an activity $a(\text{C}) = 0.1$. At this temperature, Si_3N_4 decomposes (Eq. 1.2) as indicated by the horizontal line. At an increased nitrogen pressure of 10 bar the reaction with carbon proceeds first at temperature of 1680 °C for $a(\text{C}) = 1$ and increases to 2034 °C at $a(\text{C}) = 0.17$. Finally, Si_3N_4 decomposes at this temperature. These results represent a very plausible explanation of the observed high-temperature stability of precursor-derived Si–B–C–N ceramics. However, it has to be emphasized that the actual internal pressure of nitrogen and carbon activities in the Si–B–C–N ceramics are not known exactly, and thus the nitrogen pressure of 10 bar, as well as the continuous change of the carbon activity have been assumed rather arbitrary for the calculations. Nevertheless, such a thermodynamic analysis can show qualitatively the effects and tendencies of materials behaviour.

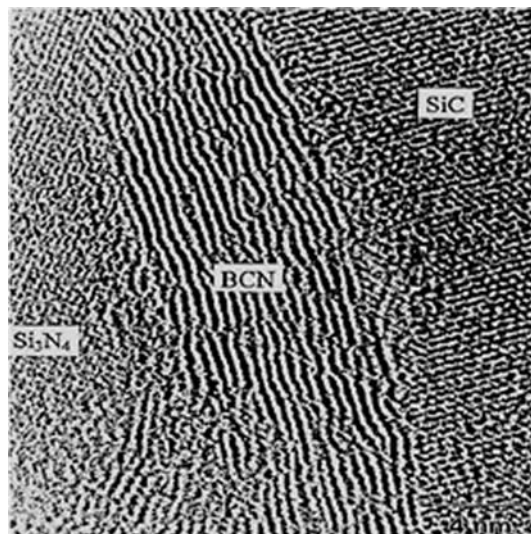


Fig. 1.4. HRTEM image of a Si–B–C–N ceramic with 1.8 at.% B. SiC and Si_3N_4 are surrounded by turbostratic BNC_x layers [44].

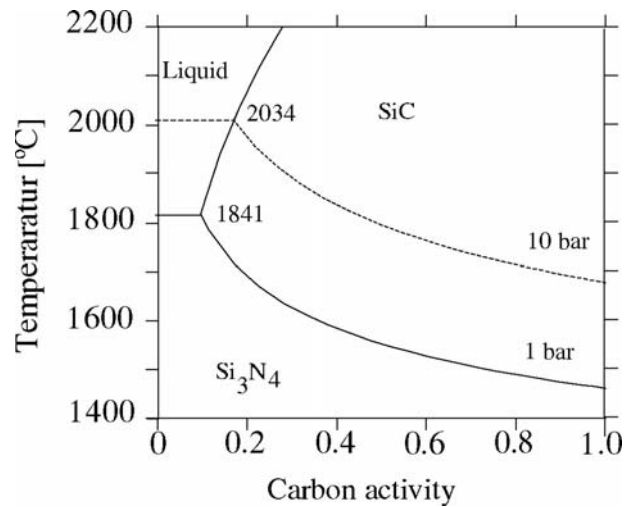


Fig. 1.5. Temperature-activity diagram of the Si-C-N system showing the effect of the carbon activity and nitrogen partial pressure on the thermal stability of Si-(B-)C-N PDCs [43].

1.3. Mass loss during annealing

The composition and molecular structure of the polymer precursor and thermolysis conditions determine the chemical composition of the resulting ceramic which is one essential factor affecting the thermal stability of the Si-B-C-N PDCs. This statement can be directly accomplished considering the summary of the experimental results obtained during the past two decades of research (see Table 1.1). The information included in this Table can be recapitulated as follows:

- For a special case of Si₃N₄-free Si-B-C-N PDCs with a B/N ratio $\cong 1$ (see Table 1.1, No. 28-30, 39, 50, and 52) the onset of mass loss has been observed at temperatures above 2000 °C in agreement with the expected stability of SiC and BN [43,45].
- Ceramics with a composition located in the range of the four-phase equilibria Si₃N₄-SiC-BN-C reveal a major role of boron [14,24,27]. Materials with a low (~ 3 wt.%) or a high (16-18 wt.%) amount of boron (see Table 1.1, No. 5-7) are less stable against thermal degradation whereas ceramics with a medium concentration around 6 wt.% B (see Table 1.1, No. 4) exhibit an extraordinary stability up to 2000 °C. This correlation of the boron content and thermal stability is illustrated well in Fig. 1.6 which shows the results of thermo-gravimetric measurements for PDCs with

different boron concentrations and similar Si/C/N ratio (see Table 1.1, No. 19-22) [31].

- To a large extent the thermal stability is also controlled by the carbon and nitrogen content of the polymer-derived ceramics. The increase of the amount of nitrogen and the decrease of the carbon fraction in ceramics with a similar Si/B ratio causes generally deterioration of the thermal stability (Table 1.1, No. 13, 14, 34 and 35) [18,36]. The particularly important role of free-carbon is demonstrated by the poor stability of ceramics without free-carbon (Table 1.1, No. 46, 47) and much better stability of PDCs with high carbon concentration (Table 1.1, No. 23-25 and 48) [32,38,39]. Decreased atomic diffusivity of silicon has been proposed as one plausible reason to explain the stabilizing influence of free-carbon on Si_3N_4 [32,46]. In contrary, an increase of the nitrogen content of ceramics with similar Si/B/C ratio causes a decrease of the thermal stability (Table 1.1, No. 36-38 and 40-44) [18,37].

In addition to the composition, structural properties and their change with temperature affect the thermal stability of PDCs. In this connection it was shown that ceramics with higher specific surface area start to decompose at lower temperatures and with higher rates. Such an effect demonstrates an evident decrease of the thermal stability connected with a decrease of the size of the ceramic particles (see Fig. 1.7) [47]. A similar dependence of the thermal stability on the particle size and the surface area has also been observed for PDCs of the SiCO system [48,49].

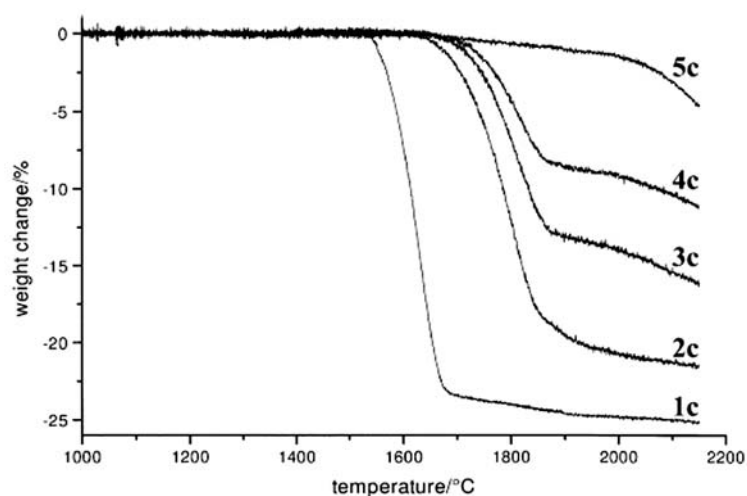


Fig. 1.6. High temperature thermogravimetry of ceramics with similar Si/C/N ratio and different boron content: (1c) 0 at. % B, (2c) 3.6 at. % B, (3c) 5.0 at. % B, (4c) 6.9 at. % B, and (5c) 9.0 at. % B [31].

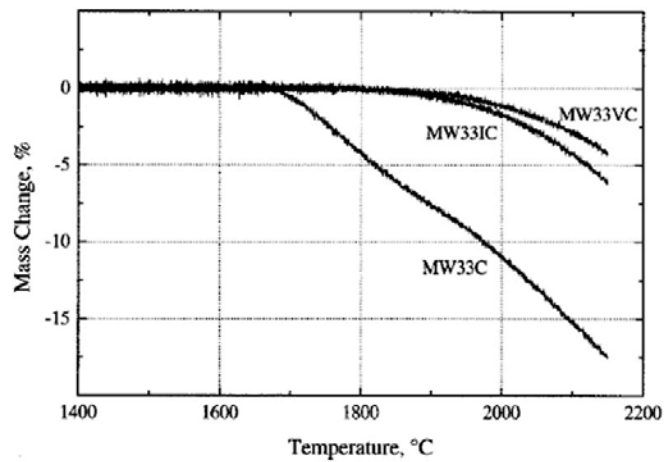


Fig. 1.7. High temperature thermogravimetry of Si-B-C-N ceramic powders with different particle sizes: (MW33VC) > 315 μm , (MW33IC) 80-315 μm , and (MW33C) 32-80 μm [47].

1.4. Structural transformations induced by annealing

An especially important feature of PDCs is their unique amorphous character and an apparent relation between the stability against thermal degradation and the resistance of this structure against crystallization. Crystallization and thermal degradation of Si_3N_4 occur at a similar range of temperature as reported for many Si-(B-)C-N PDCs [25,27,31,33,37,50,51]. This observation indicates a possible correlation of crystallization and thermal stability. Indeed, crystallization and degradation of the Si_3N_4 in the Si-B-C-N system are both temperature and time dependent effects, and both processes are influenced by the composition as well. Altogether, the important role of structural transformations induced by annealing is pointed out by these findings. Thus, crystallization of Si_3N_4 is retarded with an increase of the boron content if the Si/C/N ratio is fixed [20,31]. The typical TEM micrographs and elemental distribution images are shown in Fig. 1.8 corresponding to a Si-B-C-N ceramic after annealing at 1800°C for 10 h [52]. The elemental maps (Fig. 1.8(b)-(e)) depict the distribution of nitrogen, boron, carbon and silicon within a material made of silicon carbide and silicon nitride nano-crystallites, which are embedded in an amorphous BNC_x matrix.

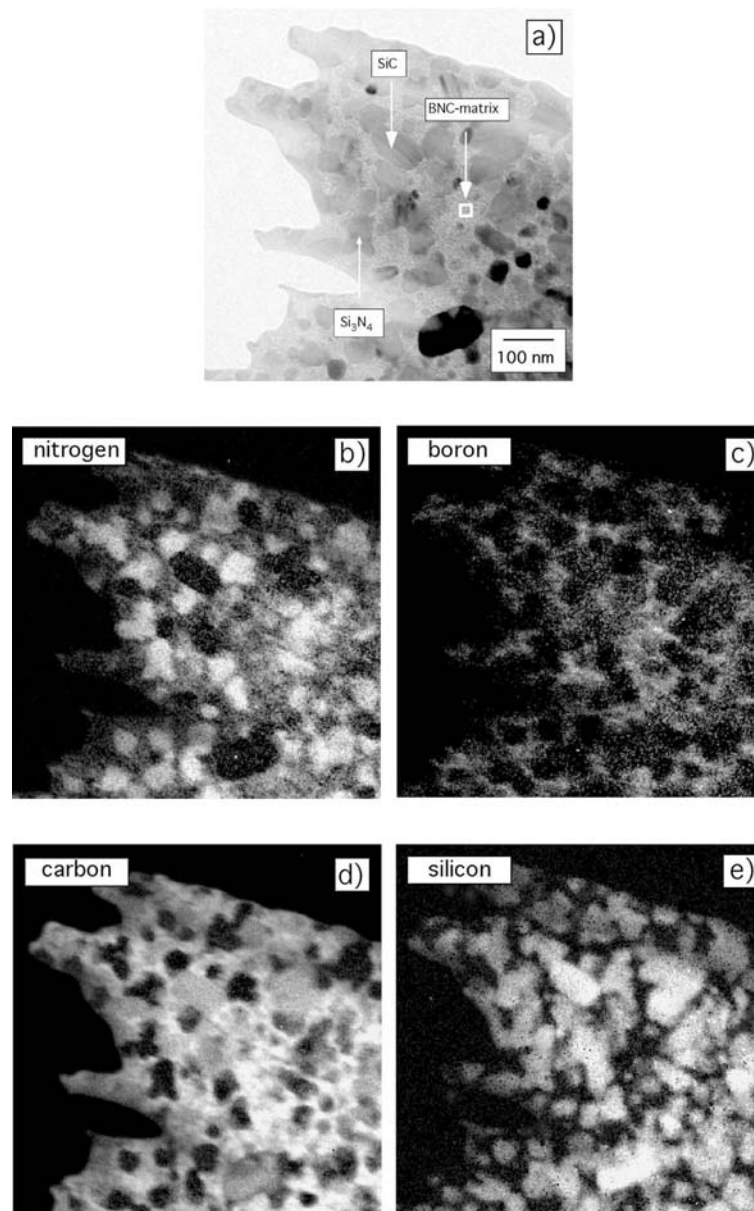


Fig. 1.8. TEM image and elemental maps of a Si–B–C–N ceramic after annealing at 1800°C for 10 h: (a) bright field image, (b) elemental map of nitrogen, (c) elemental map of boron, (d) elemental map of carbon, and (e) elemental map of silicon [52]. White areas correspond to the presence of the single elements.

As already mentioned the final composition of PDCs is determined by the kind of polymer and the thermolysis temperature. The compositions SiC_aN_b of Si–C–N PDCs are generally located within the limits of the three-phase equilibrium C–SiC– Si_3N_4 in the phase diagram of the ternary Si–C–N system and the compositions $\text{SiC}_a\text{N}_b\text{B}_c$ of Si–B–

C–N PDCs correspondingly are located within the four-phase region SiC–Si₃N₄–BN–C in the phase diagram of the quaternary Si–B–C–N system. The amorphous character of as-thermolysed Si–C–N and Si–B–C–N PDCs has been extensively proven by means of x-ray diffraction analysis (XRD) and transmission electron microscopy (TEM) [20, 53–58]. However, a particular structural feature common for all investigated materials is a phase separation demonstrated by the presence of amorphous Si–C–N domains. These domains are embedded into a matrix which consists of amorphous/turbostratic carbon and turbostratic B–N–C in the case of Si–C–N and Si–B–C–N PDCs, respectively. This effect was proven by electron- and neutron-scattering experiments and transmission electron microscopy [56, 59–61] and is in accordance with the phase separation valid also for conventional oxide-based glasses [62]. Consequently, the expression “phase separation” has also been introduced and applied to model of amorphous PDCs [63]. The characteristic features that trace back to this phase separation, i.e. amount of phases and particularly their compositions, influence essentially the above mentioned exceptional properties of PDC materials. In the case of Si–C–N ceramics, these separated domains with a composition located along the tie line SiC–Si₃N₄ are denoted as “am-SiCN” phase and composed of structural units made of SiC_iN_{4-i} tetrahedral [56, 64–66]. Such mixed tetrahedra correspond apparently to stoichiometric compounds SiC_{i/4}C_{(4-i)/3} [63]. A particular composition SiC_xN_b of a separated am-SiCN phase is a balance of the overall ceramic composition SiC_aN_b and separated amount of free carbon as illustrated in Fig. 1.9(a). Generally, the am-SiCN phase extends along the tie line SiC–Si₃N₄ as shown in the metastable phase diagram of the Si–C–N system (Fig. 1.9(b)). Analogous amorphous Si–C–N domains, am-SiCN, are also described regarding the microstructure of as-thermolysed SiBCN PDCs, and the rest considered consist of B–N–C domains. Such domains of composition located along the line C–BN represent special features of the microstructure of the SiBCN PDCs. Investigations of these ceramics after annealing above the thermolysis temperature revealed characteristic turbostratic structures of B–N–C domains formed of intercalating carbon and boron nitride layers (see Fig. 1.4) [44,61]. However, it is not decided yet whether the separated B–N–C domains should be interpreted as a homogenous BNC_x phase extended along

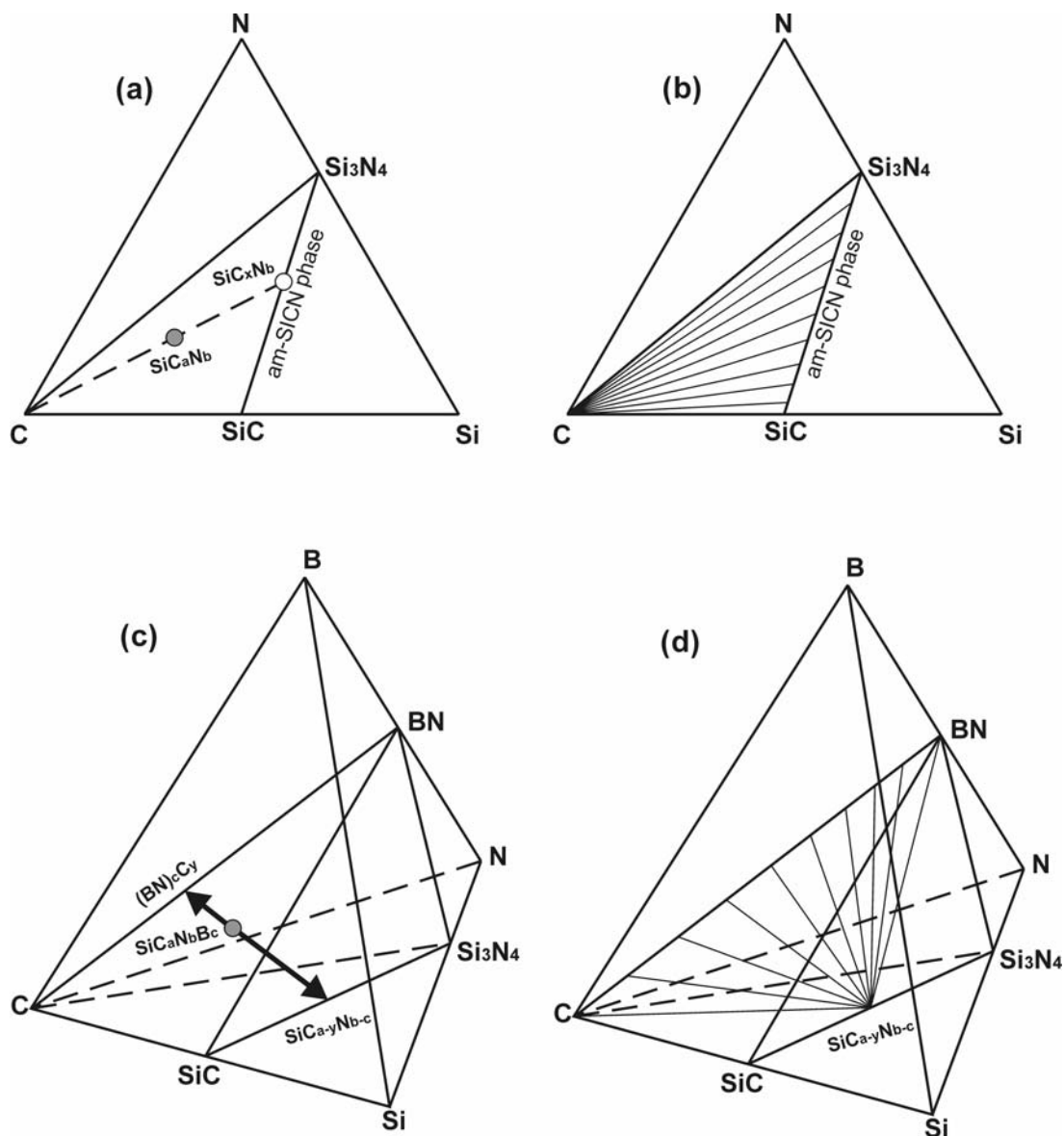


Fig. 1.9. Phase separation in Si-(B-)C-N PDCs: (a) separation of a given composition SiC_aN_b into carbon (C) and an am-SiCN phase, (b) metastable equilibrium of C and am-SiCN phases, (c) separation of a ceramic with overall composition $\text{SiC}_a\text{N}_b\text{B}_c$ into the am-SiCN phase and B-N-C domains, and (d) metastable equilibrium of B-N-C domains with a given composition $\text{SiC}_{a-y}\text{N}_{b-c}$ of the separated am-SiCN phase [63].

the tie line C-BN in the quaternary Si-B-C-N phase diagram, or as a structure composed of separate phases BN and C. Consequently, it can be deduced that Si-B-C-N ceramics of the composition $\text{SiC}_a\text{N}_b\text{B}_c$ within the four-phase region SiC-Si₃N₄-BN-C are separated into B-N-C domains of the composition $(\text{BN})_c\text{C}_y$ located on the tie line

BN-C, and Si-C-N domains of the composition $\text{SiC}_{a-y}\text{N}_{b-c}$ located on the tie line SiC-Si₃N₄ as shown in Fig. 1.9(c). Obviously there is also only one way of such a separation because the particular composition $(\text{BN})_c\text{C}_y$ of the separated B-N-C domains has to balance the composition $\text{SiC}_{a-y}\text{N}_{b-c}$ of the Si-C-N domains. However, it should be mentioned that for different ceramics with overall compositions located in the plane C-BN-SiC_{a-y}N_{b-c}, an am-SiCN phase with a defined composition can be associated with various compositions of the corresponding B-N-C domains (see Fig. 1.9(d)).

1.5. Outline of the thesis

In the present thesis, the crystallization and degradation course of amorphous Si-(B-)C-N PDCs with a constant atomic Si/C/N ratio and various boron contents were quantitatively studied for the first time in order to analyze the kinetics of these processes. Additionally, thermodynamic computations were carried out for the investigated ceramics to provide a more comprehensive understanding of the structural evolution within the amorphous materials investigated.

In chapter 2, the crystallization behavior of the amorphous ceramics including 0, 3.7, 6.0 and 8.3 at.% B investigated by X-ray diffraction (XRD) measurements is described. For these investigations, the materials were isothermally heat treated at various temperatures. It was aimed in this chapter to study qualitatively the effect of the boron content on the initial crystallization of SiC and Si₃N₄. Moreover, the Gibbs energies of the amorphous and completely crystalline state for the investigated ceramics were computed to reveal the impact of the boron content on the driving energy of the crystallization. Subsequently, the consistency between the obtained experimental and modeling results was discussed.

Chapter 3 is dedicated to the crystallization process of the amorphous ceramic including 8.3 at.% B. This process was quantitatively investigated and also modeled by a new thermodynamic approach. For this aim, the crystallized volume fractions of SiC and Si₃N₄, formed within the amorphous state, were determined by quantitative XRD analysis of the ceramics in the course of the isochronal annealing for various heating rates. Moreover, the temperature dependence of the nanocrystallite size, which was obtained from the analysis of the experimental results, was used as an input to the

modeling. Furthermore, a model derived for estimating the Gibbs energies of nanocrystalline states was applied for these studies.

Chapter 4 presents a comprehensive kinetic analysis of the Si_3N_4 crystallization in the ceramic with 8.3 at.% B. For this purpose, the ceramic samples were isothermally annealed at three different temperatures in the range between 1700 and 1850°C. Then, the XRD patterns of the as-annealed samples were quantitatively analyzed to determine the growing fraction of the Si_3N_4 crystallites as a function of time. The kinetic evaluation of the crystallization process was performed by a widely used model for the kinetic analysis of isothermal phase transformations. Consequently, the mechanisms controlling the progress of the crystallization course were identified. Additionally, the time dependence of the crystallite size was analyzed. Finally, the obtained results were discussed in order to get a better understanding of the crystallization process.

Chapter 5 addresses the kinetic influence of boron on the Si_3N_4 crystallization. For that purpose, isothermal heat treatments of the ceramics containing 3.7 and 6.0 at.% B were carried out. The same procedure as explained in the paragraph above (chapter 4) was used both for the determination of the crystallized volume fraction and the kinetic analysis. The obtained results and the ones attained in chapter 4 were compared in order to specify the effect of boron on the activation energies and mechanisms of the nucleation and growth process. Moreover, the dependence of the Si_3N_4 crystallite size on the boron content was examined in the case of annealing at constant temperature.

In chapter 6, the kinetic effect of boron on the chemical stability of the boron-free and the boron-containing (1.3 at. %) ceramic is described. The chemical instability within these ceramics corresponds to the carbothermal reaction $\text{Si}_3\text{N}_4 + 3\text{C} \rightarrow 3\text{SiC} + 2\text{N}_2^\dagger$. Consequently, the growing fraction of this reaction is proportional to the mass loss of the materials. Therefore, the isothermal mass loss of the ceramics as a function of time was measured for various temperatures using high temperature thermal gravimetric analysis (HT-TGA). Subsequently, the kinetics of the reaction was analyzed by a generalized model for the kinetic study of chemical reactions. The obtained kinetic parameters were discussed to clarify whether the presence of boron affects the mechanisms controlling the progress of the carbothermal reaction.

References

- [1] M. Takamizawa, T. Kobazashi, A. Hazashida, Y. Takeda, US Patent 4 604 367 (1986).
- [2] D. Seyferth, H. Plenio, *J. Am. Ceram. Soc.* 73 (1990) 2131.
- [3] M. Jansen, H.P. Baldus, Deutsche Offen DE 410 71 08 A1, 1992.
- [4] O. Funayama, T. Kato, Y. Tashiro, T. Isoda, *J. Am. Ceram. Soc.* 76 (1993) 717.
- [5] R. Riedel, A. Kienzle, G. Petzow, Deutsche Offen DE 432 07 83 A1, 1993.
- [6] K. Su, E.E. Remsen, G.A. Zank, L.G. Sneddon, *Chem. Mater.* 5 (1993) 547.
- [7] H.P. Baldus, M.Jansen, O. Wagner, *Key Eng. Mater.* 89-91 (1994) 75.
- [8] R. Riedel, A. Kienzle, W. Dressler, L. Ruwisch, J. Bill, F. Aldinger, *Nature* 382 (1996) 796.
- [9] T. Wideman, E. Cortez, E.E. Remsen, G.A. Zank, P.J. Carroll, L.G. Sneddon, *Chem. Mater.* 9 (1997) 2218.
- [10] L.L. Snead, S.J. Zinkle, *Nucl. Instrum. Methods Phys. Res. B* 191 (2002) 497.
- [11] R. Riedel, M. Seher, *J. Eur. Ceram. Soc.* Vol. 7 pp. 21-25 (1991).
- [12] H.J. Seifert, H.L. Lukas, F. Aldinger, *Ber. Bunsenges. Phys. Chem.* 102 (1998) 1309.
- [13] M. Weinmann, A.Zern, F. Aldinger, *Adv. Mater.* 13 (2001) 1704.
- [14] J. Bill, F. Aldinger, *Adv. Mater.* 7 (1995) 775.
- [15] H.P. Baldus, G. Passing, H. Scholz, D. Sporn, M. Jansen, J. Göring, *Key Eng. Mater.* 127-131 (1997) 177.
- [16] R. Riedel, L. Ruwisch, L. An, R. Raj, *J. Am. Ceram. Soc.* 81 (1998) 3341.
- [17] F. Aldinger, M. Weinmann, J. Bill, *Pure Appl. Chem.* 70 (1998) 439.
- [18] M. Weinmann, T.W. Kamphowe, J. Schuhmacher, K. Müller, F. Aldinger, *Chem. Mater.* 12 (2000) 2112.
- [19] M. Weinmann, J. Schuhmacher, H. Kummer, S. Prinz, J. Peng, H.J. Seifert, M. Christ, K. Müller, J. Bill, F. Aldinger, *Chem. Mater.* 12 (2000) 623.
- [20] A. Müller, P. Gerstel, M. Weinmann, J. Bill, F. Aldinger, *J. Eur. Ceram. Soc.* 20 (2000) 2655.
- [21] M. Christ, G. Thurn, M. Weinmann, J. Bill, F. Aldinger, *J. Am. Ceram. Soc.* 83 (2000) 3025.
- [22] M. Christ, A. Zimmermann, F. Aldinger, *J. Mater. Res.* 16 (2001) 1994.

- [23] S. Bernard, M. Weinmann, D. Cornu, F. Miele, F. Aldinger, *J. Eur. Ceram. Soc.* 25 (2005) 251.
- [24] J. Bill, T.W. Kamphowe, A. Müller, T. Wichmann, A. Zern, A. Jalowieki, J. Mayer, M. Weinmann, J. Schuhmacher, K. Müller, J. Peng, H.J. Seifert, F. Aldinger, *Appl. Organometal. Chem.* 15 (2001) 777.
- [25] H.P. Baldus, O. Wagner, M. Jansen, *Mater. Res. Soc. Symp. Proc.* 271 (1992) 821.
- [26] H.P. Baldus, M. Jansen, *Angew. Chem. Int. Ed. Engl.* 36 (1997) 328.
- [27] J. Bill, A. Kienzle, M. Sasaki, R. Riedel, F. Aldinger, *Advances in Sci. and Tech. Ceramics: Charting the Future 3B* (1995) 1291.
- [28] M. Weinmann, R. Haung, J. Bill, F. Aldinger, J. Schuhmacher, K. Müller, *J. Organometal. Chem.* 541 (1997) 345.
- [29] M. Weinmann, R. Haung, J. Bill, M. De Guire, F. Aldinger, *Appl. Organometal. Chem.* 12 (1998) 725.
- [30] H. Jüngermann, M. Jansen, *Mater. Res. Innovat.* 2 (1999) 200.
- [31] A. Müller, P. Gerstel, M. Weinmann, J. Bill, F. Aldinger, *J. Eur. Ceram. Soc.* 21 (2001) 2171.
- [32] Z. Wang, F. Aldinger, R. Riedel, *J. Am. Ceram. Soc.* 84-10 (2001) 2179.
- [33] A. Müller, P. Gerstel, M. Weinmann, J. Bill, F. Aldinger, *Chem. Mater.* 14 (2002) 3398.
- [34] A. Müller, J. Peng, H.J. Seifert, J. Bill, F. Aldinger, *Chem. Mater.* 14 (2002) 3406.
- [35] A. Müller, A. Zern, P. Gerstel, J. Bill, F. Aldinger, *J. Eur. Ceram. Soc.* 22 (2002) 1631.
- [36] Z. Wang, T.W. Kamphowe, S. Kats, J. Peng, H.J. Seifert, J. Bill, F. Aldinger, *J. Mater. Sci. Lett.* 19 (2000) 1701.
- [37] M. Weinmann, A. Zern, M. Hörz, F. Berger, K. Müller, F. Aldinger, *Mater. Sci. Forum* 386-388 (2002) 335.
- [38] P. Gerstel, A. Müller, J. Bill, F. Aldinger, *Chem. Mater.* 15 (2003) 4980.
- [39] Z. Wang, P. Gerstel, G. Kaiser, J. Bill, F. Aldinger, *J. Am. Ceram. Soc.* 88 (2005) 2709.
- [40] A. Müller, P. Gerstel, N. Bunjes, F. Berger, W. Sigle, K. Müller, M. Weinmann, *Int. J. Mater. Res.* 97-6 (2006) 721.

- [41] N. Saunders, P. Miodownik, "CALPHAD (calculation of phase diagrams): a comprehensive guide", In Materials series: vol. 1, (Ed.: Cahn R. W.), Pergamon: Oxford (1998).
- [42] B. Sundman, B. Jansson, J.O. Andersson, CALPHAD 9 (1985) 153.
- [43] H.J. Seifert, J. Peng, J.A. Golczewski, F. Aldinger, Appl. Organometal. Chem. 15 (2001) 794.
- [44] A. Jalowiecki, J. Bill, F. Aldinger, Composites Part A 27 (1996) 717.
- [45] H.J. Seifert, F. Aldinger, Structure and Bonding 101 (2002) 1.
- [46] K. Matsunaga, Y. Iwamoto, C.A.J. Fisher, H. Mutsuvara, J. Ceram. Soc. Japan 107 (1999) 1025.
- [47] N. Janakiraman, M. Weinmann, J. Schuhmacher, K. Müller, J. Bill, F. Aldinger, J. Am. Ceram. Soc. 85-7 (2002) 1807.
- [48] G.D. Soraru, D. Suttor, J. Sol-Gel Sci. Technol. 14 (1999) 69.
- [49] J. Parmentier, G.D. Soraru, F. Babonneau, J. Eur. Ceram. Soc. 21 (2001) 101.
- [50] H. Schmidt, G. Borchardt, A. Müller, J. Bill, J. Non-Crystalline Solids 341 (2004) 133.
- [51] H. Schmidt, G. Borchardt, Adv. Eng. Mater. 7 (2005) 221.
- [52] A. Zern, J. Mayer, N. Janakiraman, M. Weinmann, J. Bill, M. Rühle, J. Eur. Ceram. Soc. 22 (2002) 1621.
- [53] Y. Iwamoto, W. Völger, E. Kroke, R. Riedel, J. Am. Ceram. Soc. 84 (2001) 2170.
- [54] Y. Cai, A. Zimmermann, S. Prinz, A. Zern, F. Phillipp, F. Aldinger, Scripta Mater. 45 (2001) 1301.
- [55] M.A. Schiavon, G.D. Soraru, V.P. Yoshida, J. Non-Crystalline Solids 304 (2002) 76.
- [56] S. Trassl, D. Suttor, G. Motz, E. Rössler, G. Ziegler, J. Eur. Ceram. Soc. 20 (2000) 215.
- [57] J. Wan, M.J. Gasch, C.E. Lesher, A.K. Mukherjee, J. Am. Ceram. Soc. 86 (2003) 857.
- [58] Y. Cai, A. Zimmermann, A. Bauer, F. Aldinger, Acta Mater. 51 (2003) 2675.
- [59] S. Schempp, J. Dürr, P. Lamparter, J. Bill, F. Aldinger, J. Phys. Sci. 53a (1998) 127.
- [60] J. Haug, P. Lamparter, M. Weinmann, F. Aldinger, Chem. Mater. 16 (2004) 72.

-
- [61] J. Haug, P. Lamparter, M. Weinmann, F. Aldinger, *Chem. Mater.* 16 (2004) 83.
- [62] S.R. Elliot, "Physics of amorphous material", Longman, London and New York (1984) 118.
- [63] J.A. Golczewski, F. Aldinger, *Z. Metallkd.* 97 (2006) 114.
- [64] J. Seitz, J. Bill, N. Egger, F. Aldinger, *J. Eur. Ceram. Soc.* 16 (1996) 885.
- [65] C. Gérardin, F. Taulelle, D. Bahloul, *J. Mater. Chem.* 7 (1997) 117.
- [66] J. Schumacher, M. Weinmann, J. Bill, F. Aldinger, K. Müller, *Chem. Mater.* 10 (1998) 3913.

Effect of boron on the crystallization of amorphous Si-(B-)C-N polymer-derived ceramics

A.H. Tavakoli, J.A. Golczewski, J. Bill

Abstract

Amorphous Si-(B-)C-N polymer-derived ceramics (PDCs) with a boron content ranging from 0 to 8.3 at.% were synthesized by thermolysis of the boron-modified poly(methylvinylsilazane). Correlation of the boron content and the thermal stability of these materials in the course of annealing were investigated using high temperature thermal gravimetric analysis (HT-TGA). Furthermore, the initial crystallization of the as-thermolized amorphous ceramics was studied by X-ray diffraction (XRD) measurements. The increase of boron content promotes the crystallization of SiC, and inhibits the crystallization of Si₃N₄. Moreover, the ratio of α -Si₃N₄ / β -Si₃N₄ in crystalline ceramic decreases with increasing boron content. Thermodynamic modeling proves the influence of boron content on driving force for crystallization. The available thermodynamic model of amorphous Si-C-N domains, nanocrystalline silicon nitride, and nanocrystalline silicon carbide treated as the separated phases has been used to interpret the obtained results.

2.1. Introduction

Synthesis of Si-(B-)C-N PDCs has attracted considerable attention in past years due to their unique structural architecture [1-5] which cannot be obtained with other known synthesis techniques such as reactive magnetron sputtering [6,7], ion implantation [8], and high-energy ball-milling [9]. Depending on the thermal treatment, these ceramics are of glass-like, near-range-ordered and/or nanocrystalline character. This particular feature resulting by creation of inorganic materials from metal-organic precursors leads to the significant high temperature properties such as extraordinary thermal stability up to 1900 - 2000°C [10,11], noticeable oxidation resistance [3] and excellent mechanical performance [12,13].

The final composition and structure of Si-(B-)C-N PDCs are fixed by the choice of particular polymers and thermolysis temperatures. After thermolysis, the compositions SiC_aN_b or $\text{SiC}_a\text{N}_b\text{B}_c$ of the ceramic products are generally located within the limits of the three-phase region C-SiC-Si₃N₄ and the four-phase region SiC-Si₃N₄-BN-C of the ternary Si-C-N and quaternary Si-B-C-N system, respectively [14]. A particular structural feature common for all investigated as-thermolysed materials is heterogeneous owing to the separation of amorphous Si-C-N domains which in the case of Si-C-N PDCs is associated with regions of amorphous carbon, and in the case of Si-B-C-N PDCs with amorphous domains containing carbon, boron and nitrogen. Wide-angle neutron- and X-ray- scattering investigations as well as nuclear magnetic resonance (NMR) measurements [15-20] reveal an atomic short-range ordering within amorphous Si-C-N domains constructed as an assembly of structural units in form of $\text{SiC}_i\text{N}_{4-i}$ ($i = 0-4$) tetrahedra. Depending on the temperature, the size of separated regions (domains) in Si-C-N PDCs changes from 12 to 30 Å as measured by small-angle neutron- and X-ray- scattering techniques [15,16]. In the case of Si-B-C-N PDCs, the separated B-N-C domains are composed of intercalating carbon and BN layers (turbostratic B-N-C domains) [21]. Furthermore, the dimensions of separated nanodomains for boron-containing ceramics correspond with those obtained for boron free Si-C-N ceramics at essentially lower temperatures ($\Delta T \sim 200^\circ\text{C}$), what can be explained by the influence of boron on the coarsening kinetics of the separated regions [17]. Meanwhile, the phase separation of amorphous PDCs was described quantitatively using the equilibrium ternary and quaternary phase diagrams of Si-C-N and Si-B-C-

N, respectively [22,23]. Moreover, phase separation and formation of $\text{SiC}_i\text{N}_{4-i}$ tetrahedra was modeled applying molecular dynamics simulations [24-26].

The transformation of amorphous ceramics into crystalline structures built of silicon-containing nanodomains proceeding during thermal treatment depends on the overall ceramic composition, and is especially affected by the amount of boron. It was shown that with the increase of boron concentration, the sizes of Si_3N_4 crystallites change from micro to nano dimensions [27] and a hindering effect of boron addition on the crystallization and degradation of Si_3N_4 was reported [28,29]. To account for these effects, a thermodynamic modeling of crystallization for amorphous Si-C-N ceramics was recently attempted which demonstrates that the driving force of crystallization and the sequence of crystalline phase formation are connected with the ceramic composition [30-32].

There are also other factors affecting the crystallization behavior. Different chemical design of polymer precursors leads to the formation of crystalline SiC with different grain size distribution despite a similar overall composition of the ceramics and the same heat-treatment [33]. Moreover, the decrease of the particle size of the Si-B-C-N ceramic promotes the crystallization of the constituent phases due to the surface crystallization caused by vapor-phase reactions [34,35]. Besides, the changes of crystalline phases distribution have been observed in the vicinity of cracks in comparison with the bulk. This “skin-core effect” has been explained by deposition of a pure carbon layer during CH_4 gas outflow and the degradation of Si_3N_4 in consequence of the reaction with excess carbon deposited close to the surface [36].

Despite the extensive investigations on Si-(B-)C-N PDCs, the role of boron on the crystallization behavior is not well understood yet. To aim getting better insight in present work, the initial stage of SiC and Si_3N_4 crystallization in amorphous Si-(B-)C-N PDCs with similar Si/C/N ratio and variable boron content have been systematically studied and thermodynamic modeling has been attempted to interpret the obtained results.

2.2. Experimental procedures

2.2.1. Precursors synthesis, thermolysis, and post-annealing

The boron-free precursor, poly(methylvinylsilazane), was obtained by ammonolysis of dichloromethylvinylsilane according to the literature [37]. The three boron-containing precursors were synthesized via hydroboration of poly(methylvinylsilazane) with variable $[-\text{H}_3\text{CSi}(\text{Vi})\text{NH}-] / \text{H}_3\text{B.S}(\text{CH}_3)_2$ molar ratio of 8:1, 4:1, and 3:1 (Vi: $-\text{CH}=\text{CH}_2$) as described in detail elsewhere [28]. Thermolysis of the as-obtained precursors was carried out at 1100°C in quartz Schlenk tubes in a flowing argon atmosphere (heating rate $25-1100^\circ\text{C}$: $1^\circ\text{C}/\text{min}$ followed by a dwell time of 4h). The products of thermolysis in form of very coarse unshaped particles (1-3 mm) were subsequently annealed in a graphite furnace (heating rate $T \leq 1400^\circ\text{C}$: $10^\circ\text{C}/\text{min}$, $T > 1400^\circ\text{C}$: $2^\circ\text{C}/\text{min}$) using graphite crucibles under nitrogen atmosphere (1bar).

2.2.2. Measurement techniques

Chemical analysis of nitrogen, hydrogen, oxygen, and carbon was performed using a combination of different analysis equipments (Elemental Vario EL, ELTRA CS 800 C/S, and LECO TC-436 N/O) based on the combustion techniques. Furthermore, inductively coupled plasma – atomic emission spectroscopy (ICP-AES) using ISA Jobin Yvon JY70 Plus system was employed for the chemical analysis of silicon and boron.

X-ray diffraction patterns were measured with a Siemens D5000/Kristalloflex unit using $\text{Cu-K}\alpha$ radiation (40 kV, 30 mA) equipped with a quartz primary monochromator and a position-sensitive proportional counter as diffractometer. A step size of $\sim 0.01^\circ$ and a counting time of 20 sec./step were used for better precision.

High temperature thermal gravimetric analysis (HT-TGA) of the as-obtained ceramics was carried out employing a Bähr STA 501 equipment in 1 bar nitrogen atmosphere ($25-2250^\circ\text{C}$; heating rate $T \leq 1100^\circ\text{C}$: $10^\circ\text{C}/\text{min}$, $T > 1100^\circ\text{C}$: $5^\circ\text{C}/\text{min}$) using carbon crucibles.

2.3. Thermodynamic modeling

2.3.1. Amorphous phase “am-SiCN”

According to the quantitative description of phase separation [23], an amorphous Si–C–N PDC with a composition located within C-Si₃N₄-SiC three-phase equilibria is separated to amorphous graphite and amorphous Si–C–N domains as illustrated schematically in Fig. 2.1. An amorphous ceramic with composition SiC_aN_b separates

into a fraction of amorphous carbon balanced by a composition SiC_xN_b of the amorphous domains located along tie line $\text{SiC}-\text{Si}_3\text{N}_4$ according to the following formula:

$$\text{SiC}_a\text{N}_b = f_c(\text{C}) + (1 - f_c)(\text{SiC}_x\text{N}_b), \quad (2.1)$$

where $x = (4 - 3b)/4$, and $f_c = (4a + 3b - 4)/[4(1 + a + b)]$ is the fraction of the amorphous carbon. Correspondingly, the $\text{Si}-\text{B}-\text{C}-\text{N}$ amorphous ceramic of composition $\text{SiC}_a\text{N}_b\text{B}_c$ located within the four-phase equilibria of $\text{C}-\text{BN}-\text{Si}_3\text{N}_4-\text{SiC}$ is separated to the amorphous domains of composition $(\text{BN})_c\text{C}_y$ and $\text{SiC}_{a-y}\text{N}_{b-c}$ located along the $\text{C}-\text{BN}$ and $\text{SiC}-\text{Si}_3\text{N}_4$ tie lines, respectively (see Fig. 2.1) according to the formula:

$$\text{SiC}_a\text{N}_b\text{B}_c = f_{\text{B-N-C}}[(\text{BN})_c\text{C}_y] + (1 - f_{\text{B-N-C}})(\text{SiC}_{a-y}\text{N}_{b-c}), \quad (2.2)$$

where $y = (4a + 3b - 3c - 4)/4$, and $f_{\text{B-N-C}} = (4a + 3b + 5c - 4)/[4(1 + a + b + c)]$ is the fraction of the $(\text{BN})_c\text{C}_y$ domains.

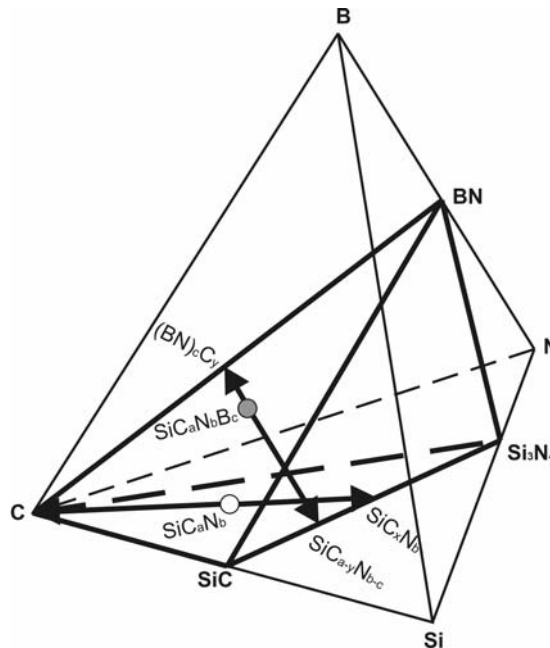


Fig. 2.1. Schematic illustration of phase separation corresponding to amorphous SiC_aN_b and $\text{SiC}_a\text{N}_b\text{B}_c$ PDCs.

The Si–C–N amorphous domains are considered to be a separate thermodynamic phase “am-SiCN” of composition on the line SiC - Si₃N₄. A thermodynamic model of this phase based on the experimental information about pure and mixed silicon-based tetrahedra in the structure of Si–C–N domains [15-20] was recently proposed [30]. In this model, the am-SiCN phase has been considered a solution phase built of tetrahedral structural units that lead to the stoichiometry SiC_{i/4}N_{(4-i)/3} (i = 0 - 4). Consequently, the composition of am-SiCN has been defined as follows:

$$\text{SiC}_x\text{N}_y = \sum_i f_i(\text{SiC}_{i/4}\text{N}_{(4-i)/3}), \quad (2.3)$$

where f_i is the fraction of the component SiC_{i/4}N_{(4-i)/3}. Thus, the Gibbs energy of this phase, $G^{\text{am-SiCN}}$, can be defined by the conventional formula:

$$G^{\text{am-SiCN}}(T) = \sum_i f_i(T) G_i(T) + RT \sum_i f_i(T) \ln[f_i(T)], \quad (2.4)$$

where $G_i(T)$ is the partial Gibbs energy of the particular constituent SiC_{i/4}N_{(4-i)/3} and the second term accounts for the entropy of random mixing. The specific values of $G_i(T)$ (Eq. (2.4)) are derived using the available thermodynamic assessments of SiC and Si₃N₄ [38,39] and the experimental information about enthalpy of amorphous SiC and Si₃N₄ formation [40,41].

2.3.2. Crystallization

The Gibbs energy of am-SiCN, $G^{\text{am-SiCN}}$, has been used to estimate a driving force for the formation of crystalline SiC and Si₃N₄ from the am-SiCN phase. Taking into account that neither Si₃N₄ nor SiC dissolve each other, the Gibbs energy of the completely crystallized state, G^{cr} , is given as follows:

$$G^{\text{cr}}(T) = f_{\text{Si-N}} G^{\text{cr-Si}_3\text{N}_4}(T) + (1 - f_{\text{Si-N}}) G^{\text{cr-SiC}}(T), \quad (2.5)$$

where $G^{\text{cr-Si}_3\text{N}_4}(T)$ is the Gibbs energy of the crystalline Si_3N_4 , $G^{\text{cr-SiC}}(T)$ is the Gibbs energy of the crystalline SiC, and $f_{\text{Si-N}}$ is the effective fraction of Si_3N_4 in the am-SiCN phase. Consequently, the thermodynamic driving force for crystallization, $\Delta G^{\text{cr}}(T)$, is the difference between the Gibbs energies of the amorphous and crystalline states:

$$\Delta G^{\text{cr}}(T) = G^{\text{cr}}(T) - G^{\text{am-SiCN}}(T). \quad (2.6)$$

This value can be used to consider thermodynamic aspects of the crystallization process.

2.4. Results

2.4.1. Characteristics of the as-obtained ceramics

Chemical compositions of the synthesized ceramics are given in Table 2.1. Correspondingly with the selection of polymer precursors, the Si/C/N atomic ratio is almost identical in the ceramics SiCN and SiCNB1-3, but the boron content increases

Table 2.1. Elemental analysis of the as-thermolysed materials^{a,b}.

Ceramic	SiCN	SiCNB1	SiCNB2	SiCNB3
Si	48.9 ± 0.8 (27.5)	45.6 ± 1.0 (25.2)	44.3 ± 1.1 (24.5)	41.7 ± 0.5 (22.9)
C	28.5 ± 0.6 (37.5)	29.4 ± 0.5 (38.1)	29.1 ± 0.7 (37.7)	28.8 ± 0.6 (37.1)
N	21.8 ± 0.5 (24.6)	20.7 ± 0.8 (23.0)	20.9 ± 1.2 (23.2)	20.8 ± 0.8 (23.0)
B	---	2.6 ± 0.1 (3.7)	4.2 ± 0.1 (6.0)	5.8 ± 0.1 (8.3)
O	0.8 ± 0.2 (0.8)	0.6 ± 0.2 (0.6)	0.8 ± 0.3 (0.8)	0.9 ± 0.1 (0.9)
H	0.6 ± 0.2 (9.5)	0.6 ± 0.1 (9.3)	0.5 ± 0.2 (7.8)	0.5 ± 0.2 (7.8)
Empirical formula^c	$\text{SiC}_{1.4}\text{N}_{0.9}\text{H}_{0.34}$	$\text{SiC}_{1.5}\text{N}_{0.9}\text{B}_{0.15}\text{H}_{0.37}$	$\text{SiC}_{1.5}\text{N}_{0.9}\text{B}_{0.24}\text{H}_{0.32}$	$\text{SiC}_{1.6}\text{N}_{1.0}\text{B}_{0.36}\text{H}_{0.34}$

^a wt.%, at.% in parenthesis

^b The error values were calculated using the standard deviation of several (at least 5) separate measurements.

^c Oxygen content is neglected.

gradually. The amount of oxygen is negligible, but the hydrogen content of the ceramic products is a bit higher than amounts of 4-7 at. % observed in the similar materials [42]. In this case, a possible reason of this discrepancy is the choice of the thermolysis at the temperature $T = 1100^{\circ}\text{C}$ which is essentially lower than the conventional thermolysis temperature $T = 1400^{\circ}\text{C}$ [28].

XRD patterns measured for the as thermolysed ceramics are shown in Fig. 2.2. The absence of distinct diffraction lines reveals a complete lack of long range atomic ordering corresponding to an amorphous character of the investigated materials.

2.4.2. Crystallization

XRD patterns measured after annealing of the amorphous ceramics at 1200°C for 2 h (Fig. 2.3(a)) do not show any peaks which reveals a possible formation of a crystalline phase. As shown in Fig. 2.3(b), after increase of the annealing temperature to 1300°C , a very broad peak corresponding to the β -SiC phase is detected for the boron-containing ceramics (SiCNB1-3), whereas the boron-free ceramic (SiCN) appears still amorphous. Moreover, with gradual increase of the boron content (ceramics SiCNB1-3) the integrated intensity of this peak also increases. This suggests that boron promotes the crystallization of SiC. Further rising of the annealing temperature to 1400°C leads apparently to an increase of the amount of SiC phase in the boron-containing ceramics, and crystallization of both β -SiC and α - Si_3N_4 phases in the case of boron-free ceramic (see Fig. 2.3(c)).

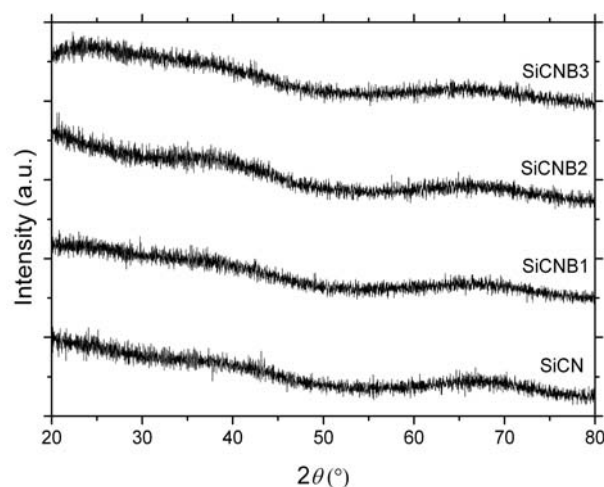


Fig. 2.2. X-ray diffraction patterns of the as-obtained boron-free (SiCN) and boron-containing ceramics (SiCNB1-3) after thermolysis treatment at 1100°C for 4 h.

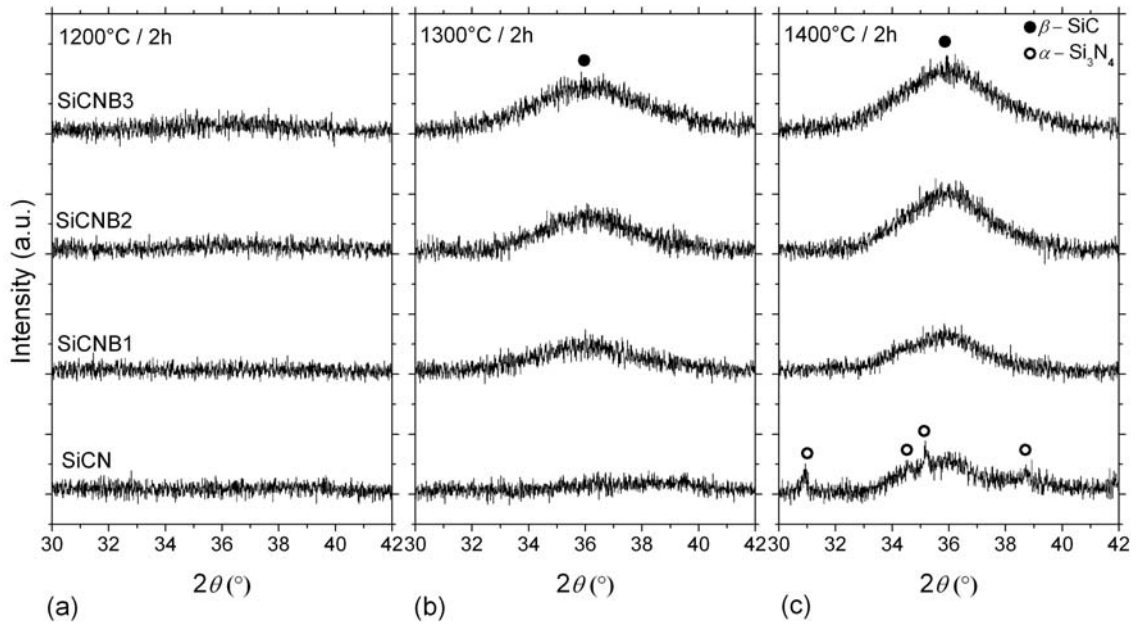


Fig. 2.3. X-ray diffraction patterns of the boron-free (SiCN) and boron-containing ceramics (SiCNB1-3) obtained after annealing at different temperatures. The marked β -SiC peak corresponds to the (111) plane. The marked α -Si₃N₄ peaks trace back to the (201), (102), (210) and ($\bar{2}\bar{1}1$) crystallographic planes.

In order to investigate the initial crystallization of Si₃N₄ in the boron-containing ceramics, higher temperatures ($T > 1400^\circ\text{C}$) are required. Therefore, the thermal stability of the materials should be taken into account. The corresponding results of the HT-TG analysis of the ceramic materials (SiCN and SiCNB1-3) under nitrogen atmosphere are shown in Fig. 2.4 which indicates that at temperatures above 1600°C , boron-free ceramic is no more stable and loses ~ 22 wt. % of mass due to the reaction of Si₃N₄ with free carbon:



whereas the addition of boron from 3.7 to 8.3 at. % increases the on-set temperature of this reaction from 1700 to 1850°C , respectively. The similar trend has been reported in the case of Si-B-C-N PDCs [28, 43]. Consequently, the temperature $T = 1650^\circ\text{C}$ was selected for studying the crystallization behavior of Si₃N₄ in the ceramics SiCNB1-3. The results are presented in Fig. 2.5. XRD patterns measured for SiCNB1-3 annealed

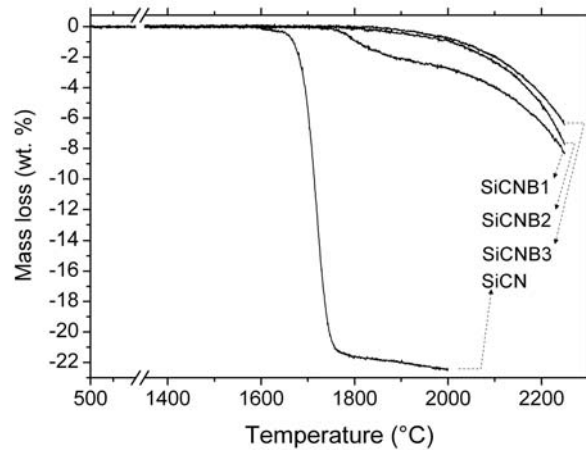


Fig. 2.4. High temperature thermal gravimetric analysis (TH-TGA) of the boron-free (SiCN) and boron-containing ceramics (SiCNB1-3). The error of 0.2-0.5 wt. % is estimated due to the scatter of values corresponding to the mass loss measured two times for each ceramic composition.

at 1650°C for 8 h indicates that the amorphous state is still present. So far, no Si_3N_4 crystallization can be detected (Fig. 2.5(a)). The increase of the time to 16 h results to the formation of both α - and β - Si_3N_4 in the ceramic containing 3.7 at.% of boron, while the diffractograms of the ceramics with higher amount of boron do not reveal crystallization of Si_3N_4 yet (see Fig. 2.5(b)). As shown in Fig. 2.5(c) and 5(d), longer annealing time of 24 and 32 h leads to the crystallization of Si_3N_4 in the ceramics with 6 and 8.3 at.% of boron, respectively. These results suggest that boron inhibits crystallization of Si_3N_4 in contrast to the alleged promotion of SiC crystallization mentioned above (see Fig. 2.3). In addition, very broad and weak peak at the range of the exhibited diffraction patterns in Fig. 2.5 can be attributed to the mixed phase of boron nitride and graphite (amorphous BNC_x turbostratic layers) [44-46]. Using the XRD data, also the influence of boron content on different contributions of α - Si_3N_4 and β - Si_3N_4 modifications of crystalline Si_3N_4 can be deduced (see Table 2.2). To get information about the ratio α - Si_3N_4 / β - Si_3N_4 , Rietveld refinement was performed using the software TOPAS 3.0 from Bruker AXS. and the standard crystallographic structures data corresponding to α - and β - Si_3N_4 [47, 48]. In the case of the ceramic SiCNB1, no significant influence of the annealing time on the ratio of the Si_3N_4 modifications was determined and the ratio α - Si_3N_4 / β - Si_3N_4 increases a bit from 56/44 ($t = 16$ h) to 60/40 ($t = 32$ h). The results for samples annealed for 32 h show that with increasing boron content, the ratio α - Si_3N_4 / β - Si_3N_4 decreases drastically from 60/40 for SiCNB1 to

32/68 in the case of SiCNB2. The ceramic SiCNB3 crystallizes initially only in form of β - Si_3N_4 .

The XRD data were also used to analyze average crystalline size, D , using the Scherrer formula [49]:

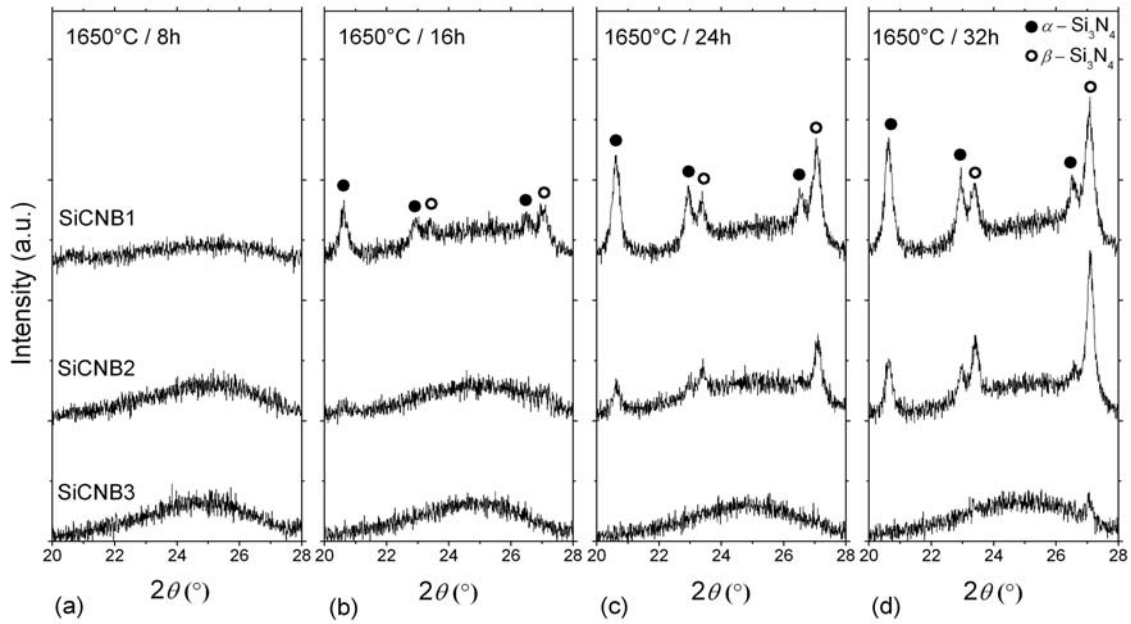


Fig. 2.5. X-ray diffraction patterns of the boron-free (SiCN) and boron-containing ceramics (SiCNB1-3) at constant annealing temperature (1650°C) and variable times. The marked α - Si_3N_4 peaks trace back to the Bragg angles corresponding to the (101), (110), and (200) crystallographic planes. The marked β - Si_3N_4 peaks are due to the Bragg angles corresponding to the (110) and (200) crystallographic planes.

Table 2.2. The estimated α - Si_3N_4 / β - Si_3N_4 phase ratios as a function of the annealing time and boron content calculated using the Rietveld refinement method.

Ceramics	SiCNB1			SiCNB2		SiCNB3
	t = 16 h	t = 24 h	t = 32 h	t = 24 h	t = 32 h	t = 32 h
Ratio (α-Si_3N_4 / β-Si_3N_4)^a	56/44	58/42	60/40	41/59	32/68	0/100

^a A typical error of \pm 5-10 % is approximated for the estimated relative phase amounts.

$$D = \frac{0.9\lambda}{\beta(2\theta)\cos(\theta)}, \quad (2.8)$$

where $\lambda=0.1540$ nm is the wave length of the Cu-K α_1 radiation, β is full-width at half maximum (FWHM) of the corresponding peak, and θ is Bragg angle in position of the peak. The FWHM of the investigated peaks shown in Fig. 2.3 and Fig. 2.5 were calculated by fit of the Lorentzian function to the diffraction data, and the instrumental peak broadening has been subtracted from the calculated data estimated using LaB₆ as a standard sample. The obtained results for the samples annealed at 1400°C (2h) are gathered in Table 2.3. The estimated average grain size of β -SiC is in the range of 2-3 nm, and is apparently not affected by the boron content. The average crystalline size of α -Si₃N₄ in the ceramic SiCN is ~100 nm and much larger than that of β -SiC. After annealing at 1650°C, the average grain size of the crystalline Si₃N₄ phase in the boron containing samples is essentially smaller, $D \approx 35$ -50 nm, in SiCNB1-3 (see Table 2.4).

2.4.3. Thermodynamic computations

The driving energies for crystallization, $\Delta G^{\text{cr}}(T)$, (Eq. (2.6)) have been computed by the Thermo-Calc software [50] for the ceramics SiCN and SiCNB1-3. The results are shown in Fig. 2.6. The negative values of $\Delta G^{\text{cr}}(T)$ estimated in the entire temperature range of 900-1800°C manifest as expected thermodynamic instability of the amorphous am-SiCN phase which increases with the temperature. This behavior is a consequence of structural changes of the am-SiCN phase revealed by changes of the computed

Table 2.3. Average grain size, D , of the crystalline phases after annealing at 1400°C for 2h^a.

Ceramics	SiCN	SiCNB1	SiCNB2	SiCNB3
$D, \beta\text{-SiC (nm)}^b$	3.0 ± 0.5	2.5 ± 0.5	2.4 ± 0.5	2.0 ± 0.5
$D, \alpha\text{-Si}_3\text{N}_4 \text{ (nm)}^c$	95 ± 15	-	-	-

^aThe main source of the error values corresponds to the estimation of the values FWHM.

^bData were calculated using the X-ray diffraction line at the Bragg angle corresponding to the (111) crystallographic plane.

^cData were calculated using the X-ray diffraction lines at the Bragg angles corresponding to the (201) and (210) crystallographic planes.

Table 2.4. Average grain size, D , of crystalline α -, β -Si₃N₄ phases at 1650°C^a.

Ceramics	SiCNB1			SiCNB2		SiCNB3
	t = 16 h	t = 24 h	t = 32 h	t = 24h	t = 32h	t = 32h
D, α -Si ₃ N ₄ (nm) ^b	38 ± 4	42 ± 5	45 ± 5	34 ± 10	47 ± 7	-
D, β -Si ₃ N ₄ (nm) ^c	35 ± 2	37 ± 2	36 ± 1	41 ± 3	50 ± 2	44 ± 2

^aThe main source of the error values corresponds to the estimation of the values FWHM.

^bData were calculated using the X-ray diffraction lines at the Bragg angles corresponding to the (101), (110), and (200) crystallographic planes.

^cData were calculated using the X-ray diffraction lines at the Bragg angles corresponding to the (110) and (200) crystallographic planes.

fractions corresponding to the particular constituents SiC_{*i*/4}N_{4-*i*/3} ($i = 0 - 4$) as displayed in Fig. 2.7. This picture shows the temperature dependence of the fraction f_i ($i = 0 - 4$) of the particular constituents estimated for am-SiCN phase in ceramics SiCN and SiCNB1-3. According to these plots, the main structural changes leading to the increase of the driving energy for crystallization emerge at temperatures ranging from 900 - 1400°C and are due to the transformation of the mixed tetrahedra, SiC_{*i*/4}N_{4-*i*/3} ($i = 1 - 3$), into the pure tetrahedra SiC₄ and SiN₄. At temperatures above 1400 °C, the am-SiCN is almost completely transformed into a fixed composition of pure tetrahedral and hence

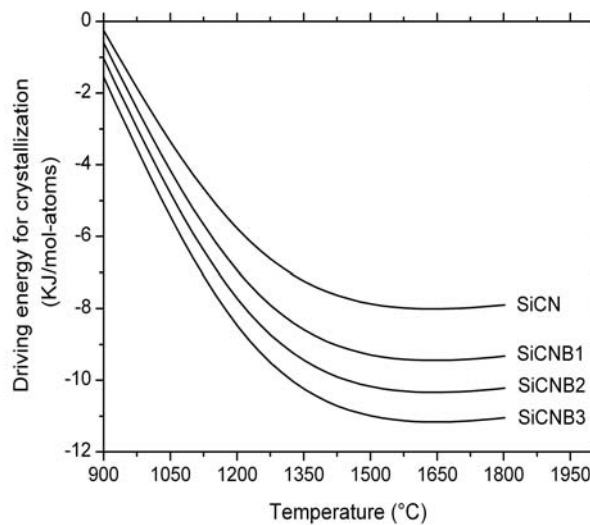


Fig. 2.6. Driving energy for the crystallization of the am-SiCN phase corresponding to the ceramics SiCN and SiCNB1-3 computed by Thermo-Calc program.

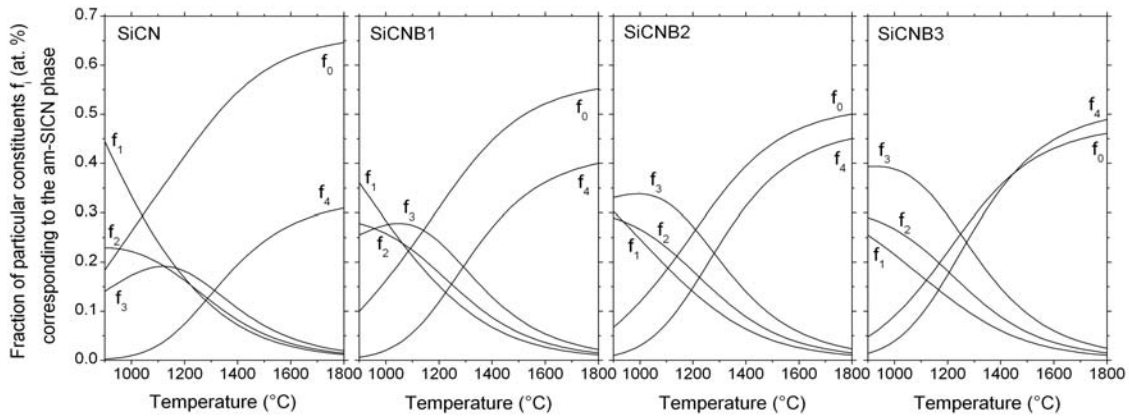


Fig. 2.7. Temperature change of the component fractions f_i within the am-SiCN phase for the ceramics SiCN and SiCNB1-3 ($f_0 = f_{\text{SiN}_{4/3}}$; $f_1 = f_{\text{SiC}_{1/4}\text{N}}$; $f_2 = f_{\text{SiC}_{1/2}\text{N}_{2/3}}$; $f_3 = f_{\text{SiC}_{3/4}\text{N}_{1/3}}$; $f_4 = f_{\text{SiC}}$).

the driving energy of am-SiCN crystallization does not change significantly in the range between 1400 - 1800°C (see Fig. 2.6 and Fig. 2.7). It should be pointed out that the ratio f_4/f_0 of pure tetrahedra increases with the increase of boron content. This reflects the development of the SiC fraction in the am-SiCN phase in consequence of the mass balance with an increasing amount of the BN phase in the B–N–C domains. Evident differences of driving energies estimated for ceramics with various boron contents can be assumed as an explanation for the boron impact on the crystallization process.

2.5. Discussion

Due to thermodynamics, an energy difference between the initial and final state is a necessary condition for any phase transformation. A development of a transformation product is usually attributed to kinetic aspects of this process. Eventually, it can also be considered as a consequence of thermodynamic equilibria. In the following discussion, this approach has been used to clarify the observed role of boron on crystallization of Si–B–C–N PDCs by thermodynamic modeling. To start with, the available assessment of thermodynamic description for Si–B–C–N system has been used [14,51]. Using this simple thermodynamic model, the phase equilibria and phase reactions attained in this system can be estimated in consequence of thermal treatment. The resulting phase fraction diagrams computed for the compositions of the investigated ceramics given in Table 2.1 are displayed in Fig. 2.8. In this calculation, the hydrogen content of ceramics

was ignored assuming at temperatures above 1050°C, hydrogen exists in the form of H₂ gas [14]. The relative phase fractions corresponding to the Gas (N₂) in Fig. 2.8 can be regarded as the relative values of mass loss due to the gas outflow from the system. This mass loss is the consequence of Si₃N₄ carbothermal reduction (Eq. (2.7)) predicted at 1484°C for all the investigated materials [51]. Only in the case of boron-free Si-C-N ceramic, this simple thermodynamic modeling fits with the mass loss of ~ 22 wt.% as observed at temperature above 1600°C (see Fig. 2.3). The only influence of the boron content demonstrated in these diagrams is increasing the fraction of the BN phase accompanied with an increase of the ratio SiC/Si₃N₄ which means decreasing the effective fraction of Si₃N₄, $f_{\text{Si-N}}$, in the am-SiCN. However, the intended explanation of the observed role of boron on the crystallization behavior can hardly be attained in this way, because in this approach the BN phase is assumed not to interact with SiC and Si₃N₄. Because of that, in all cases Si₃N₄ does not appear in calculated phase diagrams

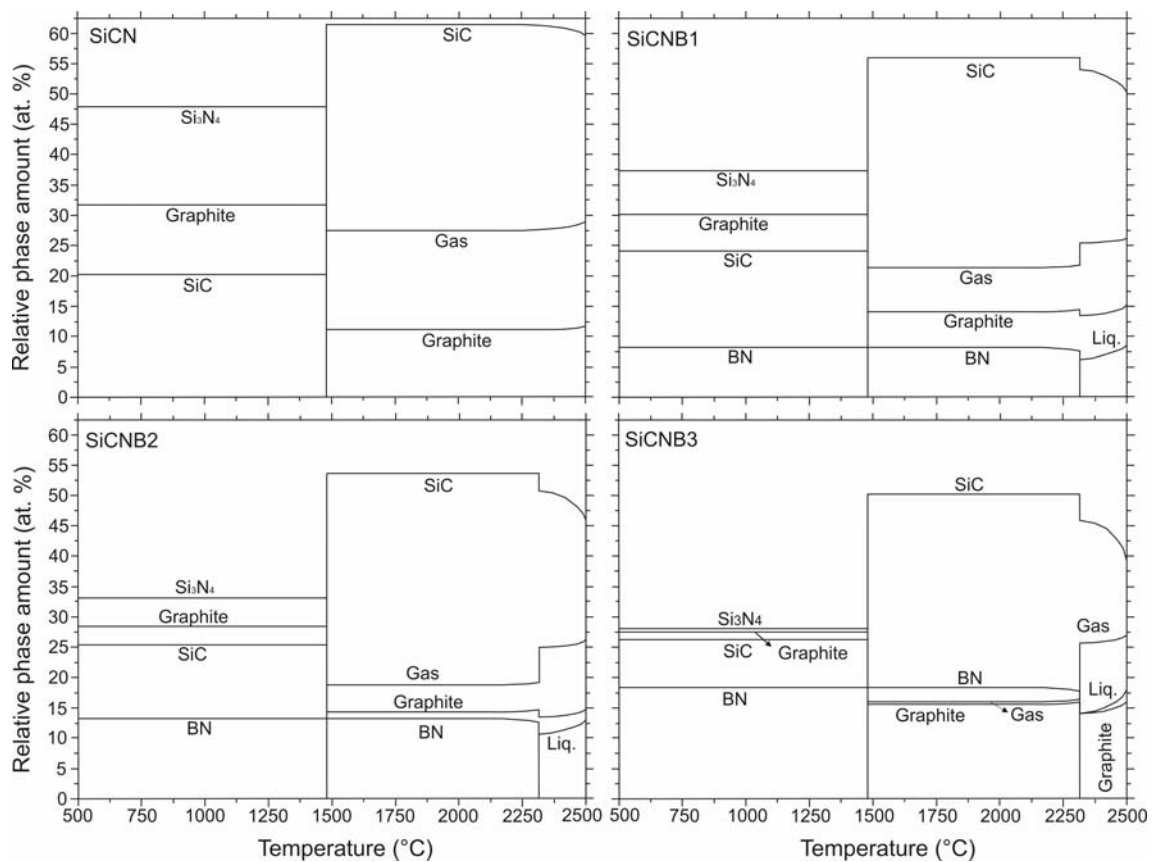


Fig. 2.8. Phase fraction diagrams of the ceramics SiCN and SiCNB1-3 computed by Thermo-Calc program.

above 1484°C in contrary to the experimental results revealing the stability of Si_3N_4 even at 2000°C [28,43]. Despite the degradation of Si_3N_4 as predicted in Fig. 2.8 for the ceramics SiCN and SiCNB1-3, the component fraction $f_{\text{SiN}_{4/3}}$ in Fig. 2.7 increases within the am-SiCN phase even at temperatures above 1484°C without any sign of the degradation. The reason for this discrepancy between two series of the computational results corresponds to the different chemical compositions considered for two separate thermodynamic modeling. In the case of thermodynamic modeling presented in this section, the overall compositions of the ceramics given in Table 2.1 were considered for the computations; however, the thermodynamic computations presented in section 2.4.3 correspond to the compositions located along tie line SiC-Si₃N₄ (see Fig. 2.1) due to the phase separation of the investigated materials (Eqs. (2.1) and (2.2)). Therefore, no free carbon is included in the applied model to react with Si₃N₄ according to Eq. (2.7) and subsequently, no mass loss has been predicted in the computational results as exhibited in Fig. 2.7.

Analysis including additional thermodynamic modeling of amorphous am-SiCN offers a further possibility to explain the observed role of boron. The computed driving forces for crystallization of the am-SiCN phase (see Fig. 2.6) prove that the gradual increase of the boron content should enhance the tendency of the crystallization. However, this enhancement concerns crystallization of SiC as well as of Si₃N₄. This result corresponds well with the experiments in the case of SiC (see Fig. 2.3), and disagrees completely with the fact that in the case of Si₃N₄, the tendency of crystallization really decreases with increasing boron content (see Fig. 2.5). Looking for reasons of the revealed shortage of the used modeling, it should be mentioned that the average crystalline size of SiC ($D \approx 2\text{-}3$ nm) as well as Si₃N₄ ($D \approx 30\text{-}50$ nm) calculated for the ceramics SiCNB1-3 using the obtained results of the XRD measurements (see Tables 2.2 and 2.3) demonstrate the nanocrystalline nature of SiC and Si₃N₄ at initial stage of crystallization. However, the thermodynamic descriptions of the SiC and Si₃N₄ used for the presented modeling of the crystallization of am-SiCN phase (see section 2.3) can not account for the nanocrystalline feature of these phases.

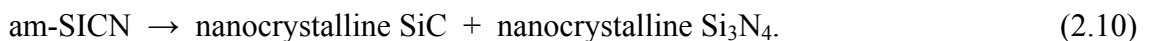
Recently, a thermodynamic model was presented in which an excess energy term connected with atoms located on the surface of crystallites was introduced to describe the nanocrystalline SiC and Si₃N₄ phases. The main assumption of this model was to

introduce average size of crystallites $\langle d \rangle$ as a characteristic of the nanocrystalline structure, and to use this parameter to derive the Gibbs energy of a nanocrystalline state. This approach, for details see [31,32], was applied in this work to consider nanocrystalline SiC and Si₃N₄ as separated phases. The Gibbs energies of these phases were obtained by adapting the general description of the Gibbs energy of a nanocrystalline phase $G^{\text{nano-cr}}$ [31,32]:

$$G^{\text{nano-cr}} = G^{\text{cr}} + \frac{G^{\text{am}} - G^{\text{cr}}}{\langle d \rangle^*}, \quad (2.9)$$

where G^{am} is the Gibbs energy of corresponding amorphous state, G^{cr} is the Gibbs energy of corresponding crystalline state without the contribution of grain boundaries, and the parameter $\langle d \rangle^* = \langle d \rangle / \langle d \rangle_{\text{min}}$ is the average crystallite dimension $\langle d \rangle$ normalized to a dimension $\langle d \rangle_{\text{min}}$ assumed as a lower limit for the size of the observed nanocrystalline SiC and/or Si₃N₄. Thus $\langle d \rangle_{\text{min}}$ represents extension of SiC₄ and SiN₄ tetrahedra in the structure of am-SiCN phase.

To attain a thermodynamic description of isothermal annealing in Ref. [32], the Gibbs energies of nanocrystalline SiC and Si₃N₄ phases were only considered functions of $\langle d \rangle^*$ and the Gibbs energy of the am-SiCN phase only a function of composition $f_{\text{Si-N}}$. Moreover, the interface controlled growth of nanocrystallites was assumed to get the expression of time dependant average dimension $\langle d \rangle(t)$. Assuming an arbitrary time scale and the arbitrary value of $\langle d \rangle_{\text{min}} = 1$, the computations of the corresponding metastable phase equilibria can be presented in the form of dimension-concentration phase diagrams as shown exemplarily in Fig 2.9. This diagram computed at $T = 1027^\circ\text{C}$ [32] demonstrates that depending on the composition of the Si-C-N domain, the am-SiCN phase can emerge in a metastable equilibrium either with nanocrystalline SiC or with nanocrystalline Si₃N₄ phase unless the dimension $\langle d \rangle^*$ does not exceed a particular value $\langle d \rangle_{\text{eut}}^*$. When $\langle d \rangle^*$ grows to values bigger than $\langle d \rangle_{\text{eut}}^*$ solely, nanocrystalline SiC and Si₃N₄ phases will appear in the microstructure in consequence of the eutectoid-like transformation of the am-SiCN:



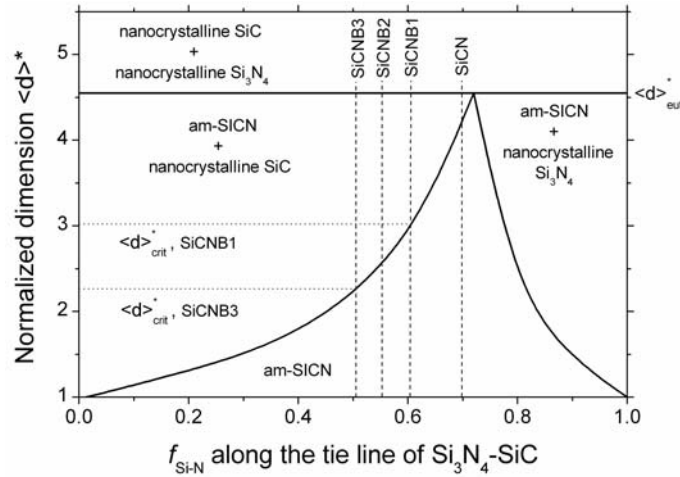


Fig. 2.9. Dimension-concentration phase diagram demonstrating metastable equilibria between am-SiCN, nano-crystalline SiC, and nano-crystalline Si_3N_4 phases at $T = 1027^\circ\text{C}$ [32]. Dash-lines indicate the fraction of Si_3N_4 within am-SiCN corresponding to the investigated ceramics SiCN and SiCNB1-3.

Considering the compositions of the am-SiCN phase corresponding to the investigated materials (dash vertical lines in Fig. 2.9), this phase diagram indicates that nanocrystalline SiC should crystallize as the first phase in all cases. Moreover, this diagram indicates that the critical dimension for the crystallization of the SiC, $\langle d \rangle_{\text{crit}}^*$, decreases with decreasing the $f_{\text{Si-N}}$ in consequence of increasing the boron content (see Fig. 2.9). This decrease of $\langle d \rangle_{\text{crit}}^*$ means earlier formation of the nanocrystalline SiC. Therefore, this diagram accounts also for the indicated promotion in the crystallization of SiC as observed by XRD studies in connection with increasing boron content (see Fig. 2.3). A further consequence is that the nanocrystalline Si_3N_4 crystallizes as a product of the eutectoid-like transformation of am-SiCN phase when the SiC nanocrystallites attain a particular value $\langle d \rangle_{\text{eut}}^*$. Consequently, this diagram can satisfactorily explain the sequence of nanocrystalline phases formation (SiC at first and Si_3N_4 subsequently) regardless of the boron content as well as the role of boron to advance crystallization of SiC. Indeed, the parts of the experimental results in the section 2.4.2 were interpreted using the thermodynamic model of the nanocrystalline phases. However, the role of boron to retard crystallization of Si_3N_4 according to the experimental results (Fig. 2.5) can not be explained by this model in which the

value $\langle d \rangle_{\text{cut}}^*$ predicted for the formation of Si_3N_4 is identical and independent of ceramic composition.

Separate discussion concerns to the increase in the ratio of $\beta\text{-Si}_3\text{N}_4 / \alpha\text{-Si}_3\text{N}_4$ with increasing the boron content in the case of annealing at constant temperature, which has been reported for the first time in this work. According to the literature [52], the temperature of the Si_3N_4 formation is the crucial factor which defines the type of the Si_3N_4 modification. Basically, $\alpha\text{-Si}_3\text{N}_4$ forms at temperatures below 1527°C and $\beta\text{-Si}_3\text{N}_4$ at higher temperatures. Moreover, the $\alpha \rightarrow \beta$ transformation has been reported only when there is a solvent in the vicinity of the two modifications observed in liquid phase sintering of Si_3N_4 [53] or using high temperatures (2000°C) under intensive mechanical pressure ($\sim 5\text{GPa}$) [54]. However, the $\beta \rightarrow \alpha$ transformation has not been reported so far. Therefore, the formation of $\alpha\text{-}$ and $\beta\text{-Si}_3\text{N}_4$ phases directly from an amorphous matrix is postulated in the case of materials investigated in this study. The main reason for the change in modification of the Si_3N_4 phase as a function of the boron content is not yet understood for us; nevertheless, variable chemical design of the ceramics obtained from polymer precursors with different amount of boron can be introduced as a plausible cause for this finding. Both $\alpha\text{-}$ and $\beta\text{-Si}_3\text{N}_4$ have hexagonal structure with differences in unit cell parameters where the c dimension of α is approximately twice that of β . The atomic layers in β modification are linked along the [001] direction in the sequence ABAB, whereas α modification has the sequence ABCDABCD, where CD layers are similar to AB layers just with 180° rotation on the c-axis [55]. Hence, it seems likely that the small variation in short-range atomic arrangement of an amorphous ceramic leads to the change in equilibrium condition of crystalline phase formation from one modification to another.

2.6. Summary and conclusions

In this work, the resistance of amorphous Si-(B-)C-N PDCs with various boron content against crystallization was studied. Thermodynamic approach was used to explain characteristics of the initial state of the crystallization process. The obtained results can be summarized as follows:

- The increase of the boron content promotes the formation of nano SiC as the first crystalline phase within the amorphous matrix whereas the crystallization of nanosized Si₃N₄ is significantly retarded.
- The Si–B–C–N ceramics with various boron concentrations contain in the crystalline state different fractions of α and β modifications of the Si₃N₄ phase. The ratio α -Si₃N₄ / β -Si₃N₄ is reduced with an increasing amount of boron.
- Thermodynamic modeling of the amorphous Si–C–N domains proves that the addition of boron increases the driving energy for the crystallization process.

Conventional thermodynamic modeling of crystalline phases in the Si–B–C–N with the BN phase regarded as non-interacting with other phases in this system can hardly account for the observed role of boron. More insight into the thermodynamics of crystallization has been gained with a new approach introducing separate thermodynamic modeling of nanocrystalline SiC and Si₃N₄ with variable dimensions. Consideration of metastable equilibria including an amorphous Si–C–N phase and evolving nanocrystalline phases, which can be estimated with this model, allows a plausible interpretation of the observed initial stages of crystallization except of the hindering effect of the boron on the crystallization of Si₃N₄.

The authors are aware of the fact that this later approach comprises processes of nucleation and growth, which are connected with kinetic aspects of crystallization. To get better insight into the kinetics of crystallization and to acquire information allowing an analysis of nucleation and growth in the ceramics investigated in this work, considerations on the time dependant evolution of their structures up to complete crystallization have been started. The obtained results and following analysis including both thermodynamic and kinetic approach are presented in chapters 3 to 5.

The dependence of the ratio α -Si₃N₄ / β -Si₃N₄ during isothermal crystallization of ceramics on the boron content has been provisionally attributed to possible changes in the chemical design of the used polymers.

Acknowledgements

The authors would like to thank Peter Gerstel for synthesis of the polymer precursors and Gerhard Kaiser for elemental analysis of the ceramic materials. Advice of Dr. Udo Welzel for evaluation of the X-ray diffraction patterns as well as substantial

cooperation of Dr. Andreas Leineweber for structural refinement of the investigated ceramics is highly appreciated. Financial support by European Union in the framework of Marie Curie Research Training Network and International Max Planck Research School for Advanced Materials is greatly acknowledged.

References

- [1] J. Bill, F. Aldinger, *Adv. Mater.* 7 (1995) 775.
- [2] H.P. Baldus, M. Jansen, *Angew. Chem. Int. Ed. Engl.* 36 (1997) 328.
- [3] F. Aldinger, M. Weinmann, J. Bill, *Pure & Appl. Chem.* 70 (1998) 439.
- [4] E. Kroke, Y.L. Li, C. Konetschny, E. Lecomte, C. Fasel, R. Riedel, *Mater. Sci. Eng. R* 26 (2000) 97.
- [5] M. Jansen, B. Jäschke, T. Jäschke, *Structure and Bonding* 101 (2002) 138.
- [6] H. Lutz, M. Bruns, F. Link, H. Baumann, *Thin Solid Films* 332 (1998) 230.
- [7] J. Vlček, Š. Potocký, J. Čížek, J. Houška, M. Kormunda, P. Zeman, V. Peřina, J. Zemek, Y. Setsuhara, S. Konuma, *J. Vac. Sci. Technol. A* 23 (2005) 1513.
- [8] M. Bruns, U. Geckle, V. Trouillet, M. Rudolphi, H. Baumann, *J. Vac. Sci. Technol. A* 23 (2005) 1114.
- [9] Z.H. Yang, D.C. Jia, Y. Zhou, C.Q. Yu, *Ceram. Int.* 33 (2007) 1573.
- [10] H.P. Baldus, M. Jansen, O. Wagner, *Key Eng. Mater.* 89-91 (1994) 75.
- [11] R. Riedel, A. Kienzle, W. Dressler, L. Ruwisch, J. Bill, F. Aldinger, *Nature* 382 (1996) 796.
- [12] M. Christ, G. Thurn, M. Weinmann, J. Bill, F. Aldinger, *J. Am. Ceram. Soc.* 83 (2000) 3025.
- [13] M. Christ, A. Zimmermann, F. Aldinger, *J. Mater. Res.* 16 (2001) 1994.
- [14] H. J. Seifert, J. Peng, J. Golczewski, F. Aldinger, *Appl. Organometal. Chem.* 15 (2001) 794.
- [15] S. Schempp, J. Dürr, P. Lamparter, J. Bill, F. Aldinger, *A J. Phys. Sci.* 53a (1998) 127.
- [16] J. Haug, P. Lamparter, M. Weinmann, F. Aldinger, *Chem. Mater.* 16 (2004) 72.
- [17] J. Haug, P. Lamparter, M. Weinmann, F. Aldinger, *Chem. Mater.* 16 (2004) 83.
- [18] N.R. Dando, A. J. Perrotta, C. Strohmman, R.M. Stewart, D. Seyferth, *Chem. Mater.* 5 (1993) 1624.

- [19] J. Dixmier, R. Bellissent, D. Bahloul, P. Goursat, *J. Eur. Ceram. Soc.* 13 (1994) 293.
- [20] J. Seitz, J. Bill, N. Egger, F. Aldinger, *J. Eur. Ceram. Soc.* 16 (1996) 885.
- [21] A. Jalowiecki, J. Bill, F. Aldinger, *Composites Part A* 27 (1996) 717.
- [22] J. Peng, PhD thesis, University of Stuttgart (2002).
- [23] J.A. Golczewski, F. Aldinger, *Int. J. Mater. Res.* 97 (2006) 114.
- [24] M. Amkreutz, T. Frauenheim, *Phys. Rev. B* 65 (2002) 134113.
- [25] N. Resta, C. Kohler, H.R. Trebin, *J. Am. Ceram. Soc.* 86 (2003) 1409.
- [26] M. Amkreutz, *Soft Mater.* 4[2-4] (2006) 187.
- [27] A. Jalowiecki, J. Bill, M. Friess, J. Mayer, F. Aldinger, R. Riedel, *Nanostructured Mater.* 6 (1995) 279.
- [28] A. Müller, P. Gerstel, M. Weinmann, J. Bill, F. Aldinger, *J. Eur. Ceram. Soc.* 20 (2000) 2655.
- [29] H. Schmidt, W. Gruber, G. Borchardt, P. Gerstel, A. Müller, N. Bunjes, *J. Eur. Ceram. Soc.* 25 (2005) 227.
- [30] J.A. Golczewski, F. Aldinger, *J. Non-Cryst. Solids* 347 (2004) 204.
- [31] J.A. Golczewski, *Int. J. Mater. Res.* 97 (2006) 729.
- [32] J.A. Golczewski, *J. Ceram. Soc. Japan* 114 (2006) 950.
- [33] N. Bunjes, A. Müller, W. Sigle, F. Aldinger, *J. Non-Cryst. Solids* 353 (2007) 1567.
- [34] N. Janakiraman, M. Weinmann, J. Schuhmacher, K. Müller, J. Bill, F. Aldinger, *J. Am. Ceram. Soc.* 85 (2002) 1807.
- [35] H.J. Kleebe, D. Suttor, H. Müller, G. Ziegler, *J. Am. Ceram. Soc.* 81 (1998) 2971.
- [36] A. Zern, J. Mayer, N. Janakiraman, M. Weinmann, J. Bill, M. Rühle, *J. Eur. Ceram. Soc.* 22 (2002) 1621.
- [37] M. Peuckert, T. Vaahs, M. Brück, *Adv. Mater.* 2 (1990) 398.
- [38] J. Gröbner, H.L. Lukas, F. Aldinger, *CALPHAD* 29 (1996) 247.
- [39] M. Hillert, S. Jonsson, B. Sundman, *Z. Metallkd.* 83 (1992) 648.
- [40] G. Fotii, *Appl. Surf. Sci.* 184 (2001) 20.
- [41] I. Tomaszkiwicz, *J. Therm. Anal. Calorim.* 65 (2001) 425.
- [42] H. Schmidt, *Soft Mater.* 4[2-4] (2006) 143.

- [43] A. Müller, P. Gerstel, M. Weinmann, J. Bill, F. Aldinger, *J. Eur. Ceram. Soc.* 21 (2001) 2171.
- [44] A. Müller, J. Peng, H.J. Seifert, J. Bill, F. Aldinger, *Chem. Mater.* 14 (2002) 3406.
- [45] P. Gerstel, A. Müller, J. Bill, F. Aldinger, *Chem. Mater.* 15 (2003) 4980.
- [46] A. Müller, P. Gerstel, N. Bunjes, F. Berger, W. Sigle, K. Müller, M. Weinmann, *Int. J. Mat. Res.* 97 (2006) 6.
- [47] H. Toraya, *J. Appl. Cryst.* 33 (2000) 95.
- [48] S. Wild, P. Grieveson, K.H. Jack, *Spec. Ceram.* 5 (1972) 385.
- [49] P. Scherrer, *Göttinger. Nachr. Math. Phys.*, 2 (1918) 98.
- [50] B. Sundman, B. Jansson, J.O. Anderson, *CALPHAD* 6 (1985) 153.
- [51] H. J. Seifert, H. L. Lukas, F. Aldinger, *Ber. Bunsenges. Phys. Chem.* 102 (1998) 1309.
- [52] N. Wada, S.A. Solin, J. Wong, S. Prochazka, *J. Non-Cryst. Solids* 43 (1981) 7.
- [53] S. Hampshire, K.H. Jack, in: D. E. Taylor, P. Popper (Eds.), *Proc. Br. Ceram. Soc.* 31 (1981) 37.
- [54] R.S. Bradley, D.C. Munro, M. Whitfield, *J. Inorg. Nucl. Chem.* 28 (1966) 1803.
- [55] D. Hardie, K.H. Jack, *Nature* 180 (1957) 332.

Quantitative XRD analysis and modeling of crystallization Process in amorphous Si–B–C–N polymer-derived ceramics

A.H. Tavakoli, J.A. Golczewski, J. Bill

Abstract

Amorphous Si–B–C–N polymer-derived ceramics (PDCs) with 8.3 at.% of boron were synthesized by thermolysis of the boron-modified poly(methylvinylsilazane). The isochronal crystallization process was quantitatively studied by X-ray diffraction (XRD) measurements using variable heating rates. Crystalline structures form within the amorphous Si–B–C–N PDCs at two stages including the formation of nanocrystalline SiC (NC-SiC) at the first stage followed with the formation of nanocrystalline Si₃N₄ (NC-Si₃N₄) and additional NC-SiC at the second stage. The change of the SiC crystallite size with temperature determined from the XRD analysis was used as a part of input data for the modeling. The metastable phase fraction diagrams were computed using an available model of metastable phase equilibria including amorphous and nanocrystalline phases for various modeling parameters and variable heating rates as well. The performed modeling is consistent with the experimental results to a large extent. The impact of modeling free parameters is discussed in order to explain the discrepancies observed between the experimental and computational results. The extended study of the NC-SiC formation at the first stage of crystallization justifies that this process is not purely controlled by the kinetics and proves a crucial role of the metastable phase equilibrium between the amorphous Si–C–N domains and NC-SiC.

3.1. Introduction

Extraordinary high temperature stability up to the temperature as high as $T \sim 2000^\circ\text{C}$ is the most important characteristic of Si–B–C–N PDCs [1,2]. Therefore, the main priority of research for these materials has been dedicated to the synthesis of the wide variety of polymer precursors in order to evaluate the influence of the constituent element ratios on the thermal stability of the as-obtained ceramics after thermolysis (see e.g. [3-8]). These attempts were aimed to reach ceramics with increased temperature stability.

The second priority of studies regarding Si–B–C–N PDCs concerns the understanding of the structural evolution during thermal treatment including polymer to ceramic transition, phase separation of amorphous domains, and crystallization of these domains, respectively. The polymer to ceramic transition results in the formation of an amorphous ceramic due to cross-linking and polycondensation reactions which occur during the process of thermolysis [5,9]. The composition $\text{SiC}_a\text{N}_b\text{B}_c$ of the ceramic product after thermolysis is generally located within the limits of the four-phase region SiC–Si₃N₄–BN–C of the quaternary Si–B–C–N system [10]. The as-obtained ceramics display heterogeneous structures owing to the separation of amorphous domains. According to the quantitative description of phase separation, a particular structural feature common for the as-thermolized materials is Si–C–N domains related with regions of amorphous domains containing carbon, boron, and nitrogen [11,12]. Wide-angle neutron- and X-ray- scattering investigations [13] as well as nuclear magnetic resonance (NMR) measurements [14,15] reveal an atomic short-range ordering within amorphous Si–C–N domains constructed as an assembly of structural units in forms of $\text{SiC}_i\text{N}_{4-i}$ ($i = 0-4$) tetrahedra. However, the separated B–N–C domains are composed of stacked carbon and BN layers (turbostratic B–N–C domains) [16]. Owing to the general location of Si–B–C–N compositions in Si–B–C–N quaternary phase diagram as described above, the crystallization of SiC, Si₃N₄, BN, and C is predicted during the course of high temperature annealing. Although, SiC and Si₃N₄ are the only visible crystalline phases, and B–N–C domains retain their amorphous feature even after long-term annealing at temperatures up to 1800°C [16-18]. As shown by XRD measurements, SiC is the primary crystalline phase which mostly forms in the modifications of α and β at temperatures $T \geq 1300^\circ\text{C}$ [7,8, 18-20]. Furthermore, it was

recently shown that the addition of boron in Si–B–C–N PDCs ($B < 10$ at.%) promotes the crystallization of NC-SiC [21]. On the contrary, the increase of boron hinders the crystallization of Si_3N_4 which forms as the second crystalline phase [6,19,21]. Moreover, boron influences the modification of the crystalline Si_3N_4 . In the case of ceramics containing 8-10 at.% of boron, crystallization of the Si_3N_4 yields the β modification at temperatures $T > 1600^\circ\text{C}$ [17-20]; however, within ceramics containing ≤ 6 at.% of boron, α - Si_3N_4 also forms in addition to β - Si_3N_4 [21]. Additionally, an attempt was made to study thermodynamics of the crystallization for Si–B–C–N PDCs using a thermodynamic model derived for amorphous Si–C–N domains [22]. The corresponding results indicate the increase of driving force for the crystallization process with increasing the boron content in the studied Si–B–C–N ceramics [21].

Despite many reports concerning the crystallization of amorphous Si–B–C–N PDCs, more fundamental studies are essential in order to explain the unique crystallization behavior of these materials. In the present work, the entire crystallization course of an amorphous Si–B–C–N PDC with the composition $\text{SiC}_{1.6}\text{N}_{1.0}\text{B}_{0.4}$ is quantitatively studied by isochronal heat treatment. Subsequently, the formation sequence and the emerging temperature of nanocrystalline phases are predicted by thermodynamic computations based on the available model of metastable phase equilibria [23,24]. In order to model the crystallization process, the experimental data analyzed from the isochronal heat treatments of the samples are applied as a part of input data. The consistency of experimental findings and metastable phase equilibria predicted by the modeling are discussed later.

3.2. Experimental Procedures

3.2.1. Precursor synthesis, thermolysis, and post-annealing

The boron-free precursor, poly(methylvinylsilazane), was obtained by ammonolysis of dichloromethylvinylsilane according to the literature [25]. The boron-containing precursor were synthesized via hydroboration of poly(methylvinylsilazane) with $[-\text{H}_3\text{CSi}(\text{Vi})\text{NH}-] / \text{H}_3\text{B.S}(\text{CH}_3)_2$ molar ratio of 3:1 (Vi: $-\text{CH}=\text{CH}_2$) as described in detail elsewhere [19]. Thermolysis of the as-obtained precursor was carried out at 1100°C in quartz Schlenk tubes in a flowing argon atmosphere (heating rate 25 - 1100°C : $1^\circ\text{C}/\text{min}$ followed by a dwell time of 4 h). The thermolysis products with a particle size

in the range between 1 and 3 mm were subsequently annealed in a graphite furnace using graphite crucibles under nitrogen atmosphere (1bar). Isochronal heat treatment was performed up to the maximum temperature $T = 2000^{\circ}\text{C}$ applying variable heating rates. To determine the increase of phase fraction corresponding to the crystalline phases, the samples were cooled down rapidly from different temperatures during the course of isochronal annealing (cooling rate $T \geq 1200^{\circ}\text{C}$: $-120^{\circ}\text{C}/\text{min}$, $T < 1200^{\circ}\text{C}$: $-25^{\circ}\text{C}/\text{min}$).

3.2.2. Chemical and thermal analysis

Chemical analysis of nitrogen, hydrogen, oxygen, and carbon was performed using a combination of different types of analysis equipment (Elemental Vario EL, ELTRA CS 800 C/S, and LECO TC-436 N/O) based on the combustion techniques. Furthermore, Inductively coupled plasma–Atomic emission spectroscopy (ICP-AES) using a ISA Jobin Yvon JY70 Plus system was employed for the chemical analysis of silicon and boron.

High temperature thermal gravimetric analysis (HT-TGA) of the as-obtained ceramics was carried out employing a Bähr STA 501 equipment in 1 bar nitrogen atmosphere (25-2250°C; heating rate $T \leq 1100^{\circ}\text{C}$: $10^{\circ}\text{C}/\text{min}$, $T > 1100^{\circ}\text{C}$: $5^{\circ}\text{C}/\text{min}$) using carbon crucible.

3.2.3. X-ray diffraction analysis

X-ray diffraction (XRD) measurements were carried out with a Philips unit using $\text{Cu-K}\alpha_1$ radiation (40 kV / 40 mA) equipped with an X'Pert accelerator (position-sensitive Si-strip detector) in order to analyze the as-obtained patterns quantitatively. Therefore, the following conditions were taken into consideration in terms of sample preparation and measurement parameters as well. As-annealed particles were milled to reach very fine particles with an average size of 1-2 μm . Then, 10 mg of the as-milled particles were dispersed in Toluene using ultrasonication. Subsequently, a thick layer of powders with diameter of 15 mm and thickness of $\sim 30 \mu\text{m}$ was formed on the surface of a single crystalline silicon wafer by sedimentation process. In order to improve the precision during XRD measurements, the step size of $\sim 0.01^{\circ}$ and the counting time of

600 sec./step were applied. Further investigations concerning the quantitative evaluation of the XRD data were performed using the *ProFit* software.

3.3. Modeling of metastable phase equilibria

3.3.1. Amorphous phase “am-SiCN”

According to the quantitative description of phase separation [12], an amorphous Si–B–C–N PDC with a composition located within the four-phase equilibria C–BN–Si₃N₄–SiC is separated to amorphous C–BN domains and amorphous Si–C–N domains as illustrated schematically in Fig. 3.1. An amorphous ceramic with a composition SiC_aN_bB_c is made of amorphous domains with compositions (BN)_cC_x and SiC_{a-x}N_{b-c} located along the C–BN and SiC–Si₃N₄ tie lines, respectively, according to the formula:

$$\text{SiC}_a\text{N}_b\text{B}_c = f_{\text{B-N-C}}[(\text{BN})_c\text{C}_x] + (1 - f_{\text{B-N-C}})(\text{SiC}_{a-x}\text{N}_{b-c}), \quad (3.1)$$

where $x = (4a + 3b - 3c - 4)/4$, and $f_{\text{B-N-C}} = (4a + 3b + 5c - 4)/[4(1 + a + b + c)]$ is the fraction of the (BN)_cC_x domain.

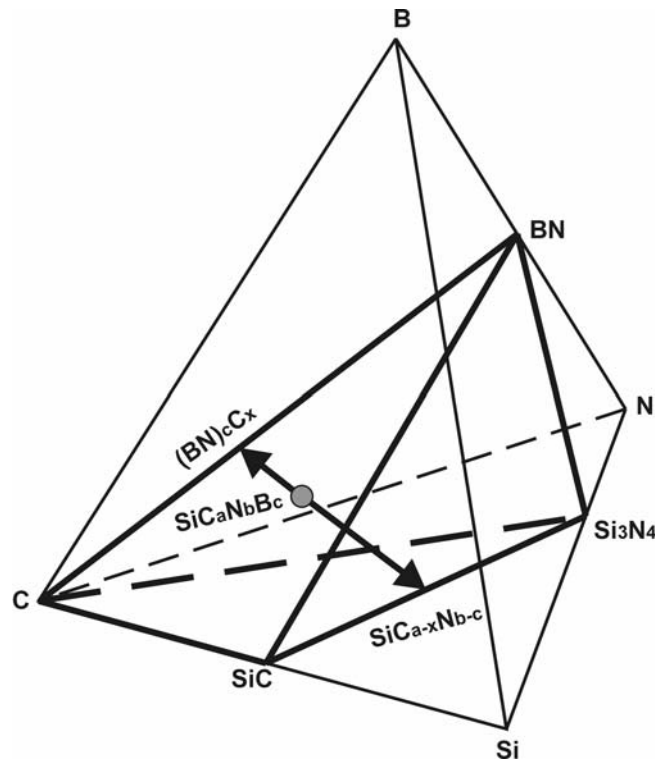


Fig. 3.1. Schematic illustration of phase separation corresponding to an amorphous SiC_aN_bB_c PDC.

The Si–C–N amorphous domains are considered to be a separate phase “am-SICN” of a composition on the line SiC - Si₃N₄. A recently proposed thermodynamic model of this phase [22] follows the experimental information about pure and mixed silicon-based tetrahedra in the structure of Si–C–N domains [26-31]. In this model, the am-SICN phase has been considered a solution phase built of tetrahedral structural units corresponding with the stoichiometry SiC_{i/4}N_{(4-i)/3} (i = 0–4). Consequently, the composition of am-SICN has been defined as follows:

$$\text{SiC}_{a-x}\text{N}_{b-c} = \sum_i f_i(\text{SiC}_{i/4}\text{N}_{(4-i)/3}), \quad (3.2)$$

where f_i is the fraction of the component SiC_{i/4}N_{(4-i)/3}. Thus, the Gibbs energy of this phase $G^{\text{am-SICN}}$ has been defined by the conventional formula:

$$G^{\text{am-SICN}}(T) = \sum_i f_i(T) G_i(T) + RT \sum_i f_i(T) \ln[f_i(T)], \quad (3.3)$$

where $G_i(T)$ is the partial Gibbs energy of the particular constituent SiC_{i/4}N_{(4-i)/3} and the second term accounts for the entropy of random mixing. The limiting values $G_0(T)$ and $G_4(T)$ (Eq. (3.3)) were derived using available thermodynamic assessments of SiC and Si₃N₄ [32,33] and experimental information about the formation enthalpy of amorphous SiC and Si₃N₄ [34,35]. The values $G_i(T)$ (i = 1–3) representing the Gibbs energies of the mixed silicon-based tetrahedra were derived as temperature independent values [22].

3.3.2. Nanocrystalline phases (NC-SiC, NC-Si₃N₄)

As recently shown by the authors [21], the thermodynamic model including Gibbs energies of the am-SICN and the completely crystallized state can not satisfactory describe the crystallization behavior of Si–B–C–N PDCs. Therefore, a possible impact of the dimensions on the Gibbs energies of the crystalline phases was taken into account. Nanocrystalline materials with crystallite dimensions less than 100 nm are

characterized by a large fraction of atoms located at interfaces. This feature, which explains essential differences between properties of nanocrystalline materials and those of conventional polycrystals [36,37], can also justify an attempt to describe the nanocrystalline states NC-SiC and NC-Si₃N₄ as separate phases. The corresponding Gibbs energies were derived introducing an excess term $\Delta G^{\text{ex}} = f_1 \Delta G_1$, where f_1 is the fraction of interface atoms and ΔG_1 accounts for the contribution of interface energy [23]. With the growth of nanocrystallites, the value f_1 decreases and consequently the excess energy ΔG^{ex} also decreases. The growth of nanocrystallites is a complex process depending both on temperature T and time t . Nevertheless, an average nanocrystallites dimension $\langle d \rangle$ can be regarded as a single parameter describing a momentary existing nanostructure and used to determine the temperature and time dependant surface atomic fraction $f_1 \propto 1/\langle d \rangle$. Naturally, the Gibbs energy of a nanocrystalline phase G^{NC} should attain values between an upper limit defined by the Gibbs energy of an amorphous state G^{am} and a lower limit defined by the Gibbs energy of a crystalline state G^{cr} . Thus, considering $\Delta G = G^{\text{am}} - G^{\text{cr}}$ as a maximum value of the excess energy corresponding with the smallest average nanocrystallites dimension $\langle d \rangle_{\text{min}}$, the Gibbs energy of nanocrystalline phase becomes:

$$G^{\text{NC}} = G^{\text{cr}} + \Delta G / \langle d \rangle^*, \quad (3.4)$$

where $\langle d \rangle^* = \langle d \rangle / \langle d \rangle_{\text{min}}$ is a normalized dimension of nanocrystallites.

Using the energy values of 27.4 and 9.8 kJ/mol-atoms as recently estimated for the energy differences between the amorphous and crystalline states of SiC and Si₃N₄, respectively, the following formulas were derived for the Gibbs energies of NC-SiC and NC-Si₃N₄ [23,24]:

$$G^{\text{NC-SiC}} = G^{\text{cr-SiC}} + 27.4 / \langle d \rangle_{\text{SiC}}^*, \quad (3.5(a))$$

$$G^{\text{NC-Si}_3\text{N}_4} = G^{\text{cr-Si}_3\text{N}_4} + 9.8 / \langle d \rangle_{\text{Si}_3\text{N}_4}^*. \quad (3.5(b))$$

3.4. Results and Discussion

3.4.1. Thermal stability of the as-thermolyzed ceramics

The phase equilibria in consequence of thermal treatment were estimated using the available assessment for the thermodynamic description of the Si–B–C–N system [10,38]. The resulting phase fraction diagram computed for the composition of the investigated ceramic (Table 3.1) is given in Fig. 3.2. In this calculation, the hydrogen content of the ceramic was ignored assuming hydrogen exists in the form of H₂ gas at temperatures above 1050°C [10]. As shown in this figure, the composition of the ceramic is defined by the four-phase equilibrium including SiC, Si₃N₄, C and BN. Furthermore, the thermal stability of the system is limited by the reaction of total Si₃N₄ with C at the temperature $T=1484^{\circ}\text{C}$ [38]. This reaction results in the formation of SiC and a mass loss of the solid phase due to Gas (N₂) evolution. The equilibrium state attained due to this reaction remains unchanged up to the maximum temperature of calculation $T = 2250^{\circ}\text{C}$. However, the thermal stability of the Si–B–C–N ceramic as measured by HT-TGA (Fig. 3.3) does not correspond with the behavior anticipated in the phase fraction diagram (see Fig. 3.2). This material reveals an extraordinary high temperature stability known since the middle of 90s [1,2] which is mostly attributed to BNC_x turbostratic layers retarding the reaction of Si₃N₄ with C [38,39]. As shown in Fig. 3.3, the upper limit of the thermal stability is estimated at $T \sim 1850^{\circ}\text{C}$ and further annealing of the ceramic at higher temperatures leads to the gradual mass loss of the system. The amount of mass loss at the maximum temperature of measurement $T = 2250^{\circ}\text{C}$ was detected ~ 6.5 wt.% which is about 50% of the mass loss predicted for total degradation of Si₃N₄ (~ 13.3 wt.%). This demonstrates the existence of Si₃N₄ even at $T = 2250^{\circ}\text{C}$.

Table 3.1. Elemental analysis of the as-thermolyzed Si–B–C–N ceramic^a.

Si	C	N	B	O	H	Empirical formula ^b
41.7 (22.9)	28.8 (37.1)	20.8 (23.0)	5.8 (8.3)	0.9 (0.9)	0.5 (7.8)	SiC _{1.6} N _{1.0} B _{0.4} H _{0.3}

^a wt.%, at.% in parenthesis

^b Oxygen content is neglected.

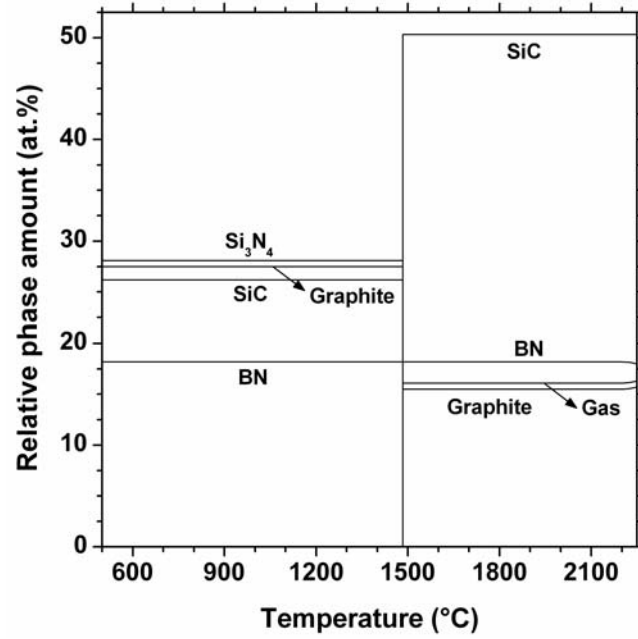


Fig. 3.2. Phase fraction diagram of the investigated Si-B-C-N material calculated by the CALPHAD method.

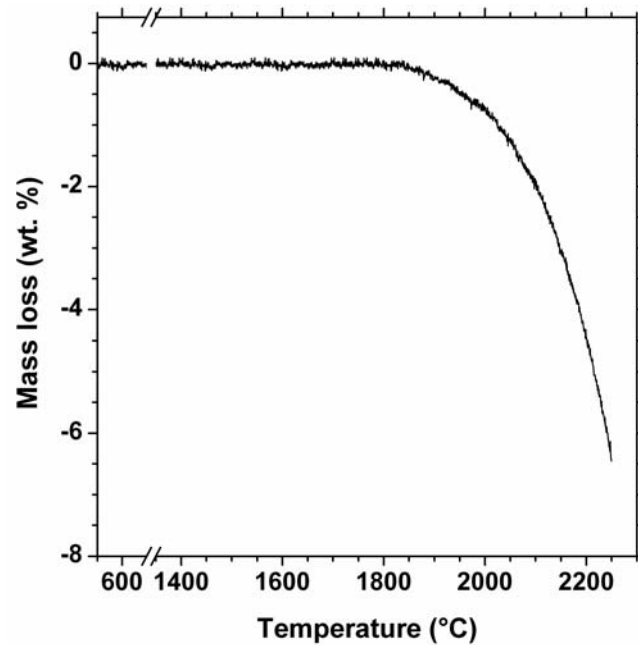


Fig. 3.3. High temperature thermal gravimetric analysis (HT-TGA) of the Si-B-C-N ceramic.

3.4.2. Isochronal investigation of structural evolution

XRD analysis of the as-thermolyzed ceramic shown in Fig. 3.4 does not reveal any peaks corresponding to crystalline phase. This indicates a complete lack of long range atomic ordering due to an amorphous character of the investigated ceramic.

The high temperature stability of the investigated ceramic (Fig. 3.3) enables to study the structural evolution within the amorphous phase by heat treatment of the ceramics without a noticeable interference from the formation of crystalline SiC as the product of Si_3N_4 degradation. To get detailed insight of the crystallization process, isochronal annealing of the amorphous materials was carried out using different heating rates $\phi = 1, 5$ and $25^\circ\text{C}/\text{min}$. Exemplary XRD patterns of the as-annealed ceramics at the specified temperatures for 2θ ranging from 55 to 66° and variable values ϕ are exhibited in Fig. 3.5. As shown in Fig. 3.5(a), the crystallization of SiC starts at temperatures between 1300 and 1500°C when $\phi = 1^\circ\text{C}/\text{min}$ is used. The increase of temperature up to $T = 1800^\circ\text{C}$ does not reveal the formation of any new crystalline phase. Further annealing up to the temperature $T = 1850^\circ\text{C}$ leads to the emergence of several peaks corresponding to $\beta\text{-Si}_3\text{N}_4$. This behavior reveals the significant resistance of the amorphous Si–B–C–N PDCs against the crystallization of Si_3N_4 rather than that of SiC. As expected, the increase of ϕ to 5 and $25^\circ\text{C}/\text{min}$ results in retardation of the crystallization process shown in Fig. 3.5(b) and 3.5(c), respectively. Considering the peaks corresponding to $\beta\text{-Si}_3\text{N}_4$ in Fig. 3.5, $\sim 50\text{-}70^\circ\text{C}$ delay for the start of Si_3N_4 crystallization is estimated with the increase of ϕ by 25 times.

In addition to the formation sequence of the crystalline phases shown in Fig. 3.5, the increase of the peak area and the decrease of the peak broadening corresponding to $\alpha/\beta\text{-SiC}$ are two other visible effects due to the increase of temperature in the course of isochronal annealing. Correspondingly, the increase of the peak areas for $\beta\text{-Si}_3\text{N}_4$ occurs

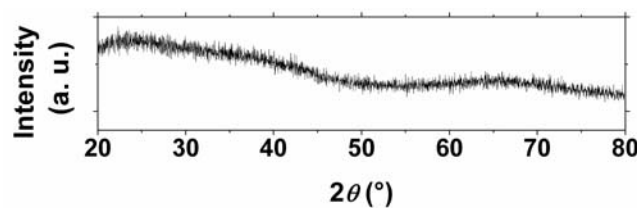


Fig. 3.4. XRD pattern of the as-thermolyzed Si–B–C–N ceramic.

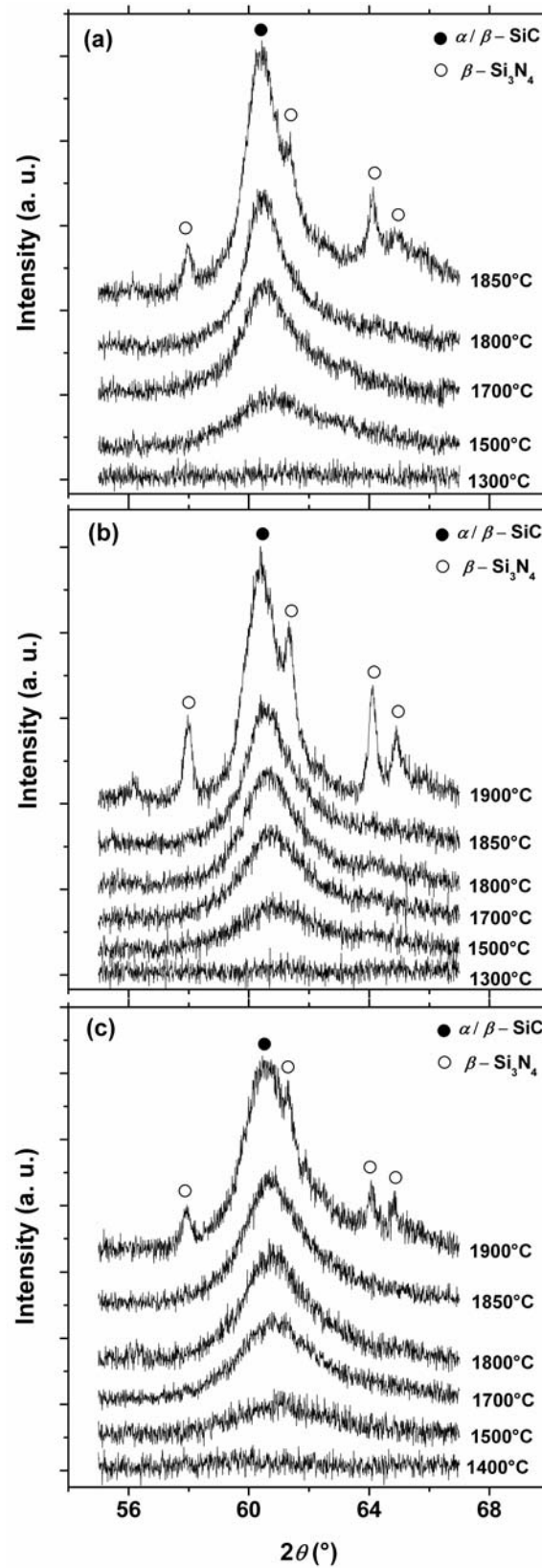


Fig. 3.5. Exemplary XRD patterns of the Si-B-C-N PDCs heated up to the specified temperatures using isochronal heat treatment: (a) 1°C/min; (b) 5°C/min; (c) 25°C/min.

at temperatures above 1800°C depending on the heating rate. In order to analyze the crystallization process quantitatively, the crystallized volume of each phase was assumed proportional to the integrated intensity $I_j(T, t)$ ($j = \text{SiC}, \text{Si}_3\text{N}_4$) of a single XRD peak at temperature T and time t . Therefore, the volume fraction of a crystalline phase $X_j(T, t) = I_j / I_j^{\text{max}}$ was estimated where I_j^{max} is the corresponding value of integrated intensity after the complete crystallization of a phase ‘j’. The value of I_j^{max} remains unchanged in the case of further annealing after fulfillment of the crystallization course as long as no reaction including phase ‘j’ occurs within the system. According to the literature [5,6,18], the crystallization of SiC in Si–B–C–N PDCs occurs in two modifications α and β , and the polytype of α -SiC is not yet identified. Moreover, the broad diffraction peaks of α - and β -SiC located at different angles 2θ are fully overlapped in the XRD patterns of the investigated ceramics due to the formation of very small nanocrystallites SiC. Therefore, the only single XRD peak common for either the (220) diffraction plane of β -SiC or the (110) diffraction plane of the α -SiC polytypes (marked in Fig. 3.5) was designated as the representative of the crystalline SiC for the quantitative analysis. The single peaks with strong intensities were regarded for the analysis of the crystalline Si_3N_4 volume fraction. These peaks, which are not shown in Fig. 3.5, correspond to the (100), (110) and (200) diffraction planes located at $2\theta=13.44, 23.39$ and 27.06° , respectively. In order to calculate the integrated intensity of the investigated peaks, the Pseudo-Voigt function was fitted to the measured XRD data. In the case of β - Si_3N_4 , the volume fraction of the crystalline phase $X_{\text{Si}_3\text{N}_4}$ was calculated for the three selected peaks and the average value was reported. Fig. 3.6 exhibits the volume fraction of crystallized phases formed during the courses of isochronal annealing. Using this figure, the structural evolution of the amorphous Si–B–C–N PDCs can be summarized as follows: (a) the first stage of the SiC crystallization is initiated above 1300°C depending on the heating rate. This crystallization period seems to terminate within the temperature range between 1700 and 1850°C (Fig. 3.6(a)); (b) the second stage of SiC crystallization occurs at the temperatures ranging from 1800 to 1850°C. Above these temperatures, the curves reveal an saturation effect including the completion of the SiC crystallization process (see Fig. 3.6(a)); (c) the crystalline Si_3N_4 forms after accomplishment of the first stage of SiC

crystallization and parallel to the second stage of the crystalline SiC formation (Fig. 3.6(b)). A similar crystallization behavior was also reported by Schmidt [40] for isothermal annealing of a bulk Si-B-C-N PDC derived from different polymer precursors. At first glance, the second crystallization stage of SiC seems to be due to the reaction of Si_3N_4 and C which sounds likely according to the HT-TGA (Fig. 3.3). However, the mass loss of ~ 0.5 wt.% was detected at 1900°C using HT-TGA which corresponds to the formation of ~ 1 wt.% of SiC. In other words, degradation of Si_3N_4

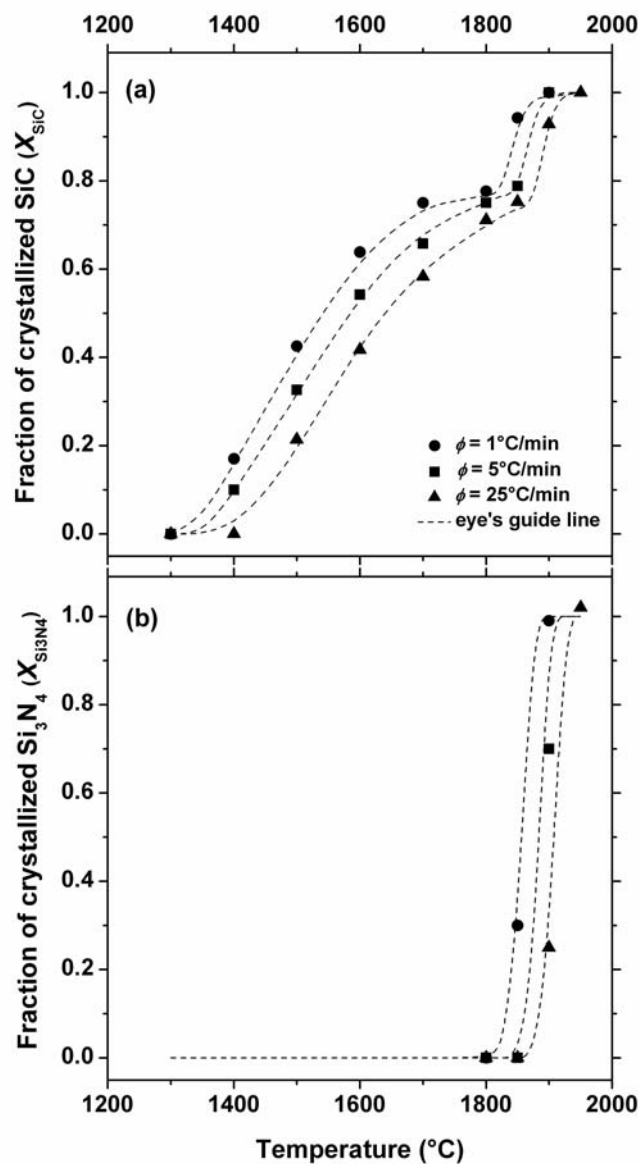


Fig. 3.6. Volume fraction of the crystallized phases SiC (a) and Si_3N_4 (b) versus temperature determined using isochronal annealing of the Si-B-C-N ceramics for various heating rates. A typical error value is estimated to be ± 0.05 .

can only increase the volume fraction of crystalline SiC by ~ 3 % whereas the increase of SiC volume fraction by ~ 20 % is estimated for the second stage of the crystallization according to the quantitative XRD analysis as shown in Fig. 3.6(a). Hence, the additional crystallization period can be attributed to the structural evolution of the amorphous Si–B–C–N PDCs in the course of isochronal heat treatment without decomposition and the loss of nitrogen.

Further analysis deals with grain size evaluation of the crystalline phases (SiC, Si₃N₄). For this aim, the XRD data were used to calculate the average crystallite size $\langle d \rangle$ applying the Scherrer formula [41]:

$$\langle d \rangle = \frac{0.9\lambda}{B(2\theta)\cos(\theta)}, \quad (3.6)$$

where $\lambda=0.1540$ nm is the wave length of the Cu-K α_1 radiation, B is full-width at half maximum (FWHM) of the corresponding peak, and θ is Bragg angle in position of the peak. The same single peak (see Fig. 3.5) investigated for the analysis of SiC volume fraction was used for the calculation of the SiC crystallite dimensions. Additionally, the single peaks located at $2\theta=13.44, 23.39$ and 27.06° were applied to determine the Si₃N₄ crystallite dimensions. These peaks, which are not shown in Fig. 3.5, were already used for the analysis of Si₃N₄ volume fraction (see Fig. 3.6). The FWHM of each diffraction line was calculated with the fit of the XRD data by the Pseudo-Voigt function. The instrumental peak broadening was subtracted from the calculated data estimated using LaB₆ as a standard sample. The obtained results are gathered in Fig. 3.7 where the average crystallite size of SiC and Si₃N₄ are plotted versus temperature. The SiC grains possess nanosized dimensions in the range of 1-2 nm at the beginning of the crystallization period. During the two stages of crystallization, the crystallite size almost increases linearly up to the values ranging from ~ 5 to ~ 7 nm, depending on the heating rate. When the temperature is further increased, the grain size deviates from linear changes and rises sharply due to the presumable coarsening of NC-SiC. Si₃N₄ crystallites also form in nanosized dimensions (40-42 nm), but they are much bigger than the ones of SiC nanograins. Moreover, the crystallite size of Si₃N₄ does not significantly change during the period of crystallization.

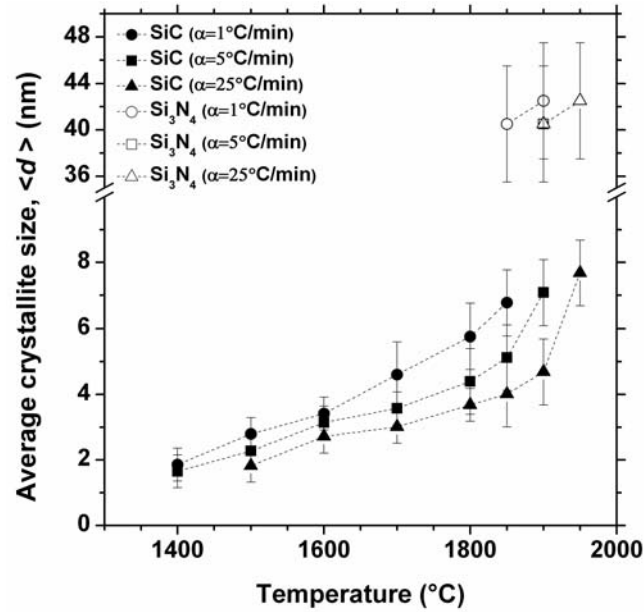


Fig. 3.7. Average grain size of NC-SiC and NC-Si₃N₄ versus temperature calculated during the isochronal crystallization of the amorphous Si-B-C-N PDCs for various heating rates.

3.4.3. Metastable phase fraction diagrams

The Gibbs energies $G^{\text{am-SiCN}}$, $G^{\text{NC-SiC}}$ and $G^{\text{NC-Si}_3\text{N}_4}$ (Eqs. (3.3) and (3.5)) were considered in order to estimate the metastable phase equilibria including am-SiCN, NC-SiC and NC-Si₃N₄. Moreover, the composition of am-SiCN phase was calculated to be SiC_{0.52}N_{0.64} based on the elemental analysis of the investigated ceramic (Table 3.2) and the phase separation formula (Eq. (3.1)). According to the definition of $\langle d \rangle^* = \langle d \rangle / \langle d \rangle_{\text{min}}$ in Eq. (3.4), the values $\langle d \rangle$ should be determined for both nanocrystalline phases (NC-SiC and NC-Si₃N₄). In principle, $\langle d \rangle$ is a temperature and time dependant parameter. On the one hand, the growth of $\langle d \rangle$ is a kinetically controlled process and on the other hand, this process affects the estimated thermodynamic equilibria. In other words, the model of metastable equilibria indicates a coupling between the thermodynamics of crystallization and the kinetics of nanocrystallites growth. Therefore, proper definition of the functions $\langle d \rangle_{\text{SiC}}(T, t)$ and $\langle d \rangle_{\text{Si}_3\text{N}_4}(T, t)$ are crucial for estimating the Gibbs energies of nanocrystalline phases $G^{\text{NC-SiC}}$ and $G^{\text{NC-Si}_3\text{N}_4}$. In the computations performed in this work, the experimental data

concerning the growth of nanograined SiC during the isochronal heat treatments were taken into account (see Fig. 3.7). As shown in this figure, the growth of nanocrystallites as a function of temperature is almost linear at temperatures $T < 1850^\circ\text{C}$. Consideration of the experimental data at temperatures above 1850°C was avoided due to the growth of SiC nanocrystallites which presumably occurs due to a coarsening phenomenon. Therefore, a linear fit of $\langle d \rangle_{\text{SiC}} = uT + v$ was carried out for the variable values ϕ . The fitting parameters are given in Table 3.2. The reasonable correlation coefficient of the experimental data points $r \approx 0.98$ presented in this table demonstrates the linear change of SiC nanocrystallites in the temperature range of study. Owing to the decomposition reaction of $\text{Si}_3\text{N}_4 \rightarrow 3\text{Si} + 2\text{N}_2$ predicted at $T \geq 1848^\circ\text{C}$ [38], the upper temperature of the modeling is also limited to the equilibrium temperature of Si_3N_4 decomposition $T = 1848^\circ\text{C}$. Therefore, the average nanocrystallite dimensions calculated for NC-SiC at $T \geq 1850^\circ\text{C}$ (see Fig. 3.7) can not be used as input data of the modeling. Thus, $\langle d \rangle_{\text{Si}_3\text{N}_4}^*$ has been assumed to be correlated with $\langle d \rangle_{\text{SiC}}^*$ and a constant ratio R of nanocrystallites growth with temperature was introduced as an additional parameter for computations:

$$R = \langle d \rangle_{\text{Si}_3\text{N}_4}^* (T) / \langle d \rangle_{\text{SiC}}^* (T). \quad (3.7)$$

Consequently, $\langle d \rangle_{\text{min, SiC}}$ and R are two free parameters used to describe the Gibbs energies of NC-SiC and NC-Si₃N₄ (Eq. (3.5)).

Table 3.2. Parameters estimated from linear fit of experimental data ($\langle d \rangle_{\text{SiC}} = uT + v$) for different values of the heating rate ϕ .

ϕ ($^\circ\text{C}/\text{min}$)	$u \times 10^3$	v	Correlation coefficient	Temp. Range ^a ($^\circ\text{C}$)
1	9.6 ± 0.6	-11.7 ± 0.9	0.984	1322-1800
5	7.4 ± 0.5	-8.7 ± 0.8	0.980	1311-1850
25	5.9 ± 0.5	-6.9 ± 0.8	0.973	1339-1850

^a The minimum temperature corresponds to the minimum dimension assumed for the crystalline SiC ($\langle d \rangle_{\text{min, SiC}} = 1 \text{ nm}$). The maximum temperature is the highest temperature detected before the crystallization of Si₃N₄.

For a first computation series, $\langle d \rangle_{\min, \text{SiC}} = 1 \text{ nm}$ and $R = 1$ were assumed. The metastable phase fraction diagrams computed by Thermo-Calc software [42] for various heating rates are presented in Fig. 3.8(a). These diagrams reveal a critical temperature T_{crit} below that, the am-SiCN is the only stable phase. As expected, T_{crit} depends on the value ϕ and increases from ~ 1356 to $\sim 1397^\circ\text{C}$ with the increase of ϕ from 1 to $25^\circ\text{C}/\text{min}$. At temperatures $T \geq T_{\text{crit}}$, the formation of NC-SiC is predicted. Consequently, the amount of am-SiCN decreases gradually as the fraction of NC-SiC increases with temperature. Indeed, there is a metastable equilibrium between the am-SiCN and NC-SiC in the range of temperature between T_{crit} and the specific value of temperature T_{eut} . As temperature reaches to the value T_{eut} , the remaining am-SiCN is totally transformed due to the eutectoid-like reaction:



where NC-Si₃N₄ forms together with an additional amount of NC-SiC (see Fig 3.8(a)). The value T_{eut} also depends on heating rate and increases from $\sim 1399^\circ\text{C}$ for $\phi = 1^\circ\text{C}/\text{min}$ to $\sim 1462^\circ\text{C}$ for $\phi = 25^\circ\text{C}/\text{min}$. At temperatures above T_{eut} , no transformation is predicted to occur and the metastable phase equilibrium between NC-SiC and NC-Si₃N₄ remains stable up to 1848°C .

The role of the free parameters (R and $\langle d \rangle_{\min, \text{SiC}}$) on the metastable phase equilibria is discussed in the following in order to reach better consistency between the crystallization modeling and the quantitative crystallization study carried out by evaluation of XRD patterns as shown in Fig. 3.6. Therefore, $\langle d \rangle_{\min, \text{SiC}} = 1 \text{ nm}$ remained unchanged and the temperature dependence of nanocrystallites dimensions for NC-Si₃N₄ was considered two times smaller than that of NC-SiC ($R = 0.5$) for a second computation series. The results of this second computation series are shown in Fig. 3.8(b). As indicated, the values of T_{crit} do not change comparing with the first computation series (Fig. 3.8(a)). Since $\langle d \rangle_{\text{SiC}}^*(T)$ is not affected by the value R , the metastable equilibrium between the am-SiCN and NC-SiC is also not influenced and consequently, the value T_{crit} remains unchanged. However, T_{eut} moves to higher temperatures in comparison with first approximation of the computation (Fig. 3.8(a)).

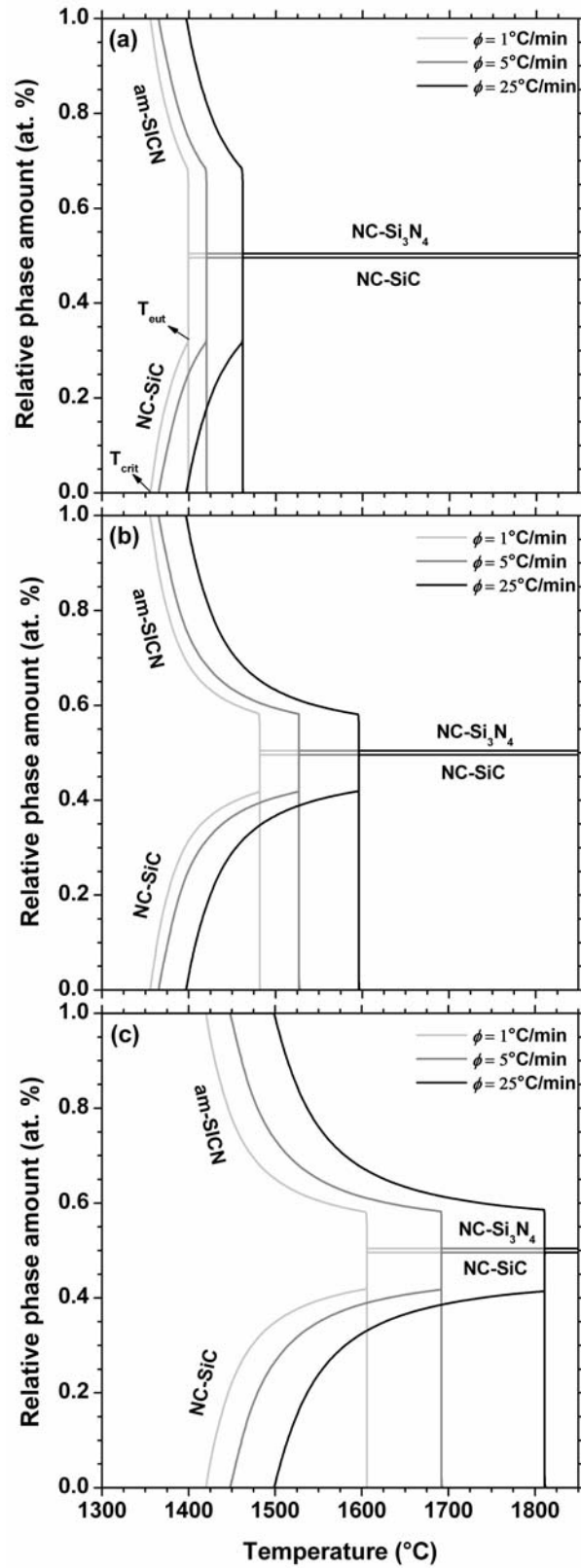


Fig. 3.8. Metastable phase fraction diagrams including am-SiCN, NC-SiC and NC-Si₃N₄ computed by Thermo-Calc software for different heating rates and variable modeling parameters: (a) $\langle d \rangle_{\text{min, SiC}} = 1 \text{ nm}$, $R = 1$; (b) $\langle d \rangle_{\text{min, SiC}} = 1 \text{ nm}$, $R = 0.5$; (c) $\langle d \rangle_{\text{min, SiC}} = 1.5 \text{ nm}$, $R = 0.5$.

Correspondingly, the eutectoid-like reaction (Eq. (3.8)) occurs at ~ 1482 , 1527 and 1596°C for the heating rate $\phi = 1, 5, 25^\circ\text{C}/\text{min}$, respectively. According to Eq. (3.7), the dependence of $\langle d \rangle_{\text{Si}_3\text{N}_4}^*$ on temperature is reduced with decreasing the value R from 1 to 0.5. Consequently, $G^{\text{NC-Si}_3\text{N}_4}$ (Eq. 3.5(b)) is located at a higher state of energy which reflects a higher temperature stability for metastable equilibrium between the am-SiCN and NC-SiC (the increase of T_{eut}).

As a third series of computations, the sensitivity of metastable phase equilibria to the value $\langle d \rangle_{\text{min,SiC}}$ was examined. The value $\langle d \rangle_{\text{min,SiC}}$ can not exceed the smallest crystallite dimension of SiC ($\langle d \rangle_{\text{SiC}} = 1.65 \pm 0.5 \text{ nm}$) calculated from XRD measurement. Thus, the value $\langle d \rangle_{\text{min,SiC}} = 1.5 \text{ nm}$ and the value $R = 0.5$ were chosen in order to compute the metastable phase fraction diagram. As exhibited in Fig. 3.8(c), the change of both T_{crit} and T_{eut} represent the impact of the parameter $\langle d \rangle_{\text{min,SiC}}$ on the metastable phase equilibria. The increase of the value $\langle d \rangle_{\text{min,SiC}}$ results in the increase of T_{crit} to 1419 , 1448 and 1499°C for $\phi = 1, 5, 25^\circ\text{C}/\text{min}$, respectively. Moreover, T_{eut} increases as compared to the values reported for the second approximation of the computation (see Fig. 3.8(b)). Depending on the heating rate, these values change from 1605 to 1811°C with increasing ϕ from 1 to $25^\circ\text{C}/\text{min}$. To explain the reasons of increasing T_{crit} and T_{eut} in the last series of computations, the definition of $\langle d \rangle_{\text{SiC}}^*(T) = \langle d \rangle_{\text{SiC}}(T) / \langle d \rangle_{\text{min,SiC}}$ should be taken into account. The dependence of $\langle d \rangle_{\text{SiC}}^*$ on the temperature is reduced with increasing $\langle d \rangle_{\text{min,SiC}}$. Therefore, $G^{\text{NC-SiC}}$ is located at a higher state of energy according to Eq. 3.5(a). Consequently, the stability of the am-SiCN phase increases to a higher temperature which corresponds to an increase of T_{crit} (see Fig. 3.8(c)). Furthermore, the dependence of $\langle d \rangle_{\text{Si}_3\text{N}_4}^*$ on temperature also decreases due to the correlation of $\langle d \rangle_{\text{Si}_3\text{N}_4}^*$ and $\langle d \rangle_{\text{SiC}}^*$ as defined in Eq. (3.7). Hence, $G^{\text{NC-Si}_3\text{N}_4}$ (Eq. 3.5(b)) is also placed at a higher state of energy which leads to a shift of T_{eut} to the elevated temperatures comparing with the values of T_{eut} obtained in the second series of computations. Summarizing the conclusions derived from Fig. 3.8, the temperatures corresponding to the metastable phase transformations (T_{crit} , T_{eut}) significantly depend on the free parameters of the modeling ($\langle d \rangle_{\text{min,SiC}}$, R). However,

the crystallization process in two stages and the formation sequence of nanocrystalline phases (NC-SiC, NC-Si₃N₄) are the characteristics of the metastable phase fraction diagrams computed for the variable values $\langle d \rangle_{\min, \text{SiC}}$ and R .

3.4.4. Discussion on the consistency of experimental analysis and modeling

The summary of the quantitative XRD study (Fig. 3.6) and the computation of the metastable phase equilibria (Fig. 3.8) were considered in order to analyze the correspondence between the results obtained by the modeling of the isochronal crystallization and the experimental study. The main correspondence concerns the two stages of crystallization characterized by the formation of NC-SiC at the first and the subsequent formation of NC-SiC and NC-Si₃N₄ during the second stage of the crystallization. Moreover, the onset temperature of NC-SiC formation was detected between 1300 and 1500°C (see Fig. 3.6) in agreement with the values T_{crit} estimated in the metastable phase equilibria computed for the variable modeling parameters (see Fig. 3.8). Furthermore, the volume fraction of NC-SiC crystallized at the first stage ($X_{\text{SiC}} \approx 0.8$) is almost identical for both the experimental findings and the metastable phase fraction diagrams computed for the value $R = 0.5$ (Figs. 3.8(b) and 3.8(c)).

The main discrepancy between the experimental analysis and computational modeling associates with the temperature T_{eut} corresponding to the second stage of the crystallization as denoted eutectoid-like transformation (Eq. (3.8)). Depending on the heating rate, T_{eut} was determined to be located in the range between 1800 and 1900°C based on the experimental study shown in Fig. 3.6. However, T_{eut} changes for the computational results in a wide range of temperature from ~1400 to ~1810°C as discussed in section 3.4.3. Consequently, T_{eut} predicted by modeling significantly depends both on the heating rate and the modeling free parameters (R and $\langle d \rangle_{\min, \text{SiC}}$). On the contrary, the temperatures T_{eut} detected for the second stage of the crystallization using experimental investigations (Fig. 3.6) do not reveal the noticeable dependence on the heating rate. The presumable reason for this distinction is related to the values $\langle d \rangle_{\text{Si}_3\text{N}_4}^* = f(T)$ estimated for the modeling of $G^{\text{NC-Si}_3\text{N}_4}$ due to a limitation of the modeling temperature ($T = 1848^\circ\text{C}$).

Further discussion regarding the differences of the experimental results and the modeling output concerns the increase of the NC-SiC phase amount at the first stage of crystallization. As shown in Fig. 3.6, the crystallization process gradually proceeds in a large range of temperature. However, the fraction of NC-SiC sharply increases at the initial temperatures of the crystallization for the computed phase fraction diagrams. Subsequently, the rest of the transformation proceeds rapidly (Fig. 3.8(a)) or slowly as indicated in Fig. 3.8(b) and 3.8(c), depending on the modeling conditions. As explained in section 3.4.3, the increase of the NC-SiC phase fraction estimated by modeling for the first stage of crystallization occurs due to the temperature change of the metastable equilibrium between am-SiCN and NC-SiC. However, the progress of NC-SiC crystallization determined by the experimental investigations (Fig. 3.6) also comprises the kinetic aspects of the crystallization including nucleation and growth. In this connection, the role of the kinetics is considered for discussion in order to figure out to what extent the crystallization kinetics can individually explain the formation process of NC-SiC as exhibited in Fig. 3.6. To investigate the formation kinetics of NC-SiC at the first stage of crystallization, the Ozawa equation [43] was used:

$$\frac{d \ln(-\ln(1 - X_{T,NC-SiC}))}{d \ln \phi} = -n, \quad (3.9)$$

where $X_{T,NC-SiC}$ is the normalized volume fraction of NC-SiC formed at temperature T and heating rate ϕ . n is regarded as the growth exponent value. Fig. 3.9 shows the linear dependence of $\ln(-\ln(1 - X_{T,NC-SiC}))$ on $\ln \phi$ at different temperatures. The value n can be obtained from the slope of the fitted lines. Consequently, the mean value $n \approx 0.3$ was detected almost independent of the temperature. According to the literature [44-46], the value of $1 < n < 4$ is reasonable in order to estimate the predominant mechanisms of the nucleation and growth processes. Therefore, no clear explanation for the crystallization kinetics of NC-SiC can be deduced from the value $n \approx 0.3$ obtained using this kinetic model. The existence of a very complex mechanism that can not be analyzed by the conventional kinetic models like Eq. (3.9) is a simple possible reason for this finding. Despite the uncertainty about the capability of the model (Eq. (3.9)) used to explain the

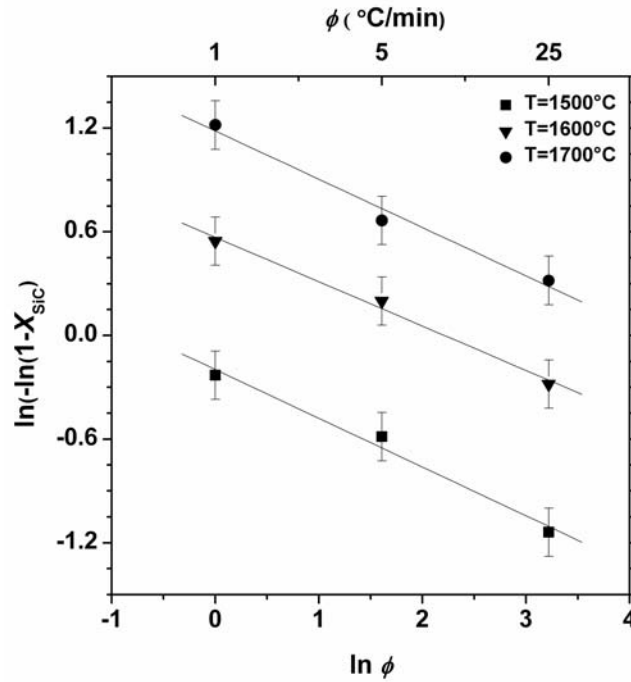


Fig. 3.9. Plot of $\ln(-\ln(1-X_{T,NC-SiC}))$ versus $\ln \phi$ for different temperatures. The solid lines indicate the linear fit of data according to the Eq. (3.9).

crystallization kinetics of the NC-SiC formation, the very small value n means a minor dependence of the NC-SiC phase fraction on the heating rate at constant temperature. This means the major role of temperature rather than time for the progress of the crystallization process. In other words, the obtained value $n \approx 0.3$ can also be considered additional evidence which verifies that the increase of the NC-SiC phase fraction is mostly due to the temperate change of the metastable phase equilibrium between the am-SiCN and NC-SiC.

3.5. Summary and Conclusions

In the present study, the isochronal crystallization of an amorphous Si-B-C-N PDC was studied using quantitative XRD analysis. Moreover, a model of metastable phase equilibria including am-SiCN, NC-SiC and NC-Si₃N₄ was used in order to estimate the formation process of the nanocrystalline phases. The temperature dependence of the nanocrystallite dimensions in the performed modeling was

determined using the results of the XRD analysis. The achieved results are summarized as follows:

- SiC nanocrystallites form as the first crystalline phase at temperatures above 1300°C, depending on the heating rate. This stage of crystallization proceeds slowly with the increase of temperature.
- Depending on the heating rate, the second stage of crystallization occurs at temperatures in the range between 1800 and 1900°C. This period of crystallization, which proceeds very fast with increasing the temperature, includes the formation of the Si₃N₄ nanocrystallites in addition to the evolution of further SiC nanocrystallites.
- Metastable phase fraction diagrams as the outcome of the modeling demonstrate a two-stage crystallization process: the formation of NC-SiC at first and the subsequent eutectoid-like transformation of the remained amorphous phase to nanocrystalline phases Si₃N₄ and SiC.

To a large extent, the crystallization process according to the experimental analysis is in agreement with the formation of NC-SiC and NC-Si₃N₄ within the am-SiCN predicted using the model of metastable phase equilibria. The temperature dependence of the normalized dimensions assumed for the growth of Si₃N₄ nanocrystallites ($\langle d \rangle_{\text{Si}_3\text{N}_4}^* = f(T)$) was concluded as a main reason of the discrepancies observed between the experimental and computational findings. It was also demonstrated that the increase in the phase fraction of NC-SiC at the first stage of crystallization is predominantly the consequence of change in the metastable phase equilibrium between the am-SiCN and NC-SiC with increasing temperature and can not be explained by the conventional kinetic model used in this work.

Acknowledgements

The authors would like to thank Peter Gerstel, Maritta Dudek, Gerhard Kaiser and Reinhard Mager for the polymer synthesis, XRD measurements, chemical analysis and technical support, respectively. Comments of Dr. Udo Welzel for evaluation of the X-ray diffraction patterns are highly acknowledged. Financial support by European Union in the framework of Marie Curie Research Training Network and International Max Planck Research School for Advanced Materials is greatly appreciated.

References

- [1] H.P. Baldus, M. Jansen, O. Wagner, *Key Eng. Mater.* 89-91(1994) 75.
- [2] R. Riedel, A. Kienzle, W. Dressler, L. Ruwisch, J. Bill, F. Aldinger, *Nature*, 382 (1996) 796.
- [3] M. Weinmann, T.W. Kamphowe, J. Schuhmacher, K. Müller, F. Aldinger, *Chem. Mater.* 12 (2000) 2112.
- [4] Z. Wang, F. Aldinger, R. Riedel, *J. Am. Ceram. Soc.* 84 (2001) 2179.
- [5] J. Bill, T. W. Kamphowe, A. Müller, T. Wichmann, A. Zern, A. Jalowiecki, J. Mayer, M. Weinmann, J. Schuhmacher, K. Müller, J. Peng, H.J. Seifert, F. Aldinger, *Appl. Organometal. Chem.* 15 (2001) 777.
- [6] A. Müller, P. Gerstel, M. Weinmann, J. Bill, F. Aldinger, *J. Eur. Ceram. Soc.* 21 (2001) 2171.
- [7] M.A. Schiavon, G.D. Soraru, I.V.P. Yoshida, *J. Non-Crystalline Solids* 348 (2004) 156.
- [8] S. Bernard, M. Weinmann, P. Gerstel, P. Miele, F. Aldinger, *J. Mater. Chem.* 15 (2005) 289.
- [9] F. Aldinger, M. Weinmann, J. Bill, *Pure and Appl. Chem.* 70 (1998) 439.
- [10] H.J. Seifert, J. Peng, J. Golczewski, F. Aldinger, *Appl. Organometal. Chem.* 15 (2001) 794.
- [11] J. Peng, PhD thesis, University of Stuttgart (2002).
- [12] J.A. Golczewski, F. Aldinger, *Int. J. Mater. Res.* 97 (2006) 114.
- [13] J. Haug, P. Lamparter, M. Weinmann, F. Aldinger, *Chem. Mater.*, 16 (2004) 83.
- [14] J. Schuhmacher, F. Berger, M. Weinmann, J. Bill, F. Aldinger, K. Müller, *Appl. Organometal. Chem.* 15 (2001) 809.
- [15] F. Berger, A. Müller, F. Aldinger, K. Müller, *Z. Anorg. Allg. Chem.* 63 (2005) 355.
- [16] A. Jalowiecki, J. Bill, F. Aldinger, *Composites Part A* 27 (1996) 717.
- [17] A. Zern, J. Mayer, N. Janakiraman, M. Weinmann, J. Bill, M. Rühle, *J. Eur. Ceram. Soc.* 22 (2002) 1621.
- [18] N. Janakiraman, M. Weinmann, J. Schuhmacher, K. Müller, J. Bill, F. Aldinger, *J. Am. Ceram. Soc.* 85 (2002) 1807.

- [19] A. Müller, P. Gerstel, M. Weinmann, J. Bill, F. Aldinger, *J. Eur. Ceram. Soc.* 20 (2000) 2655.
- [20] A. Müller, A. Zern, P. Gerstel, J. Bill, F. Aldinger, *J. Eur. Ceram. Soc.* 22 (2002) 1631.
- [21] A.H. Tavakoli, P. Gerstel, J.A. Golczewski, J. Bill, *J. Non-Cryst. Solids* 355 (2009) 2381.
- [22] J.A. Golczewski, F. Aldinger, *J. Non-Cryst. Solids* 347 (2004) 204.
- [23] J.A. Golczewski, *Int. J. Mater. Res.* 97 (2006) 729.
- [24] J.A. Golczewski, *J. Ceram. Soc. Japan* 114 (2006) 950.
- [25] M. Peuckert, T. Vaahs, M. Brück, *Adv. Mater.* 2 (1990) 398.
- [26] S. Schempp, J. Dürr, P. Lamparter, J. Bill, F. Aldinger, *A J. Phys. Sci.* 53 (1998) 127.
- [27] J. Dürr, P. Lamparter, J. Bill, S. Steeb, F. Aldinger, *J. Non-Cryst. Solids* 232-234, (1998) 155.
- [28] J. Haug, P. Lamparter, M. Weinmann, F. Aldinger, *Chem. Mater.* 16 (2004) 72.
- [29] N.R. Dando, A. J. Perrotta, C. Strohmam, R.M. Stewart, D. Seyferth, *Chem. Mater.* 5 (1993) 1624.
- [30] J. Dixmier, R. Bellissent, D. Bahloul, P. Goursat, *J. Eur. Ceram. Soc.* 13 (1994) 293.
- [31] J. Seitz, J. Bill, N. Egger, F. Aldinger, *J. Eur. Ceram. Soc.* 16 (1996) 885.
- [32] J. Gröbner, H.L. Lukas, F. Aldinger, *CALPHAD* 29 (1996) 247.
- [33] M. Hillert, S. Jonsson, B. Sundman, *Z. Metallkd.* 83 (1992) 648.
- [34] G. Foti, *Appl. Surf. Sci.* 184 (2001) 20.
- [35] I. Tomaszkiwicz, *J. Therm. Anal. Calorim.* 65 (2001) 425.
- [36] H. Gleiter, *Prog. Mater. Sci.*, 33 (1989) 223.
- [37] R.W. Siegle, "in *Physics of New Materials*", Springer Series in Material Sciences, Vol. 27 (Edited by F.E. Fujita), Springer Verlag, Berlin (1994).
- [38] H.J. Seifert, H.L. Lukas, F. Aldinger, *Ber. Bunsenges. Phys. Chem.* 102 (1998) 1309.
- [39] M. Weinmann, J. Schuhmacher, H. Kummer, S. Prinz, J. Peng, H.J. Seifert, M. christ, K. Müller, J. Bill, F. Aldinger, *Chem. Mater.* 12 (2000) 623.
- [40] H. Schmidt, *Soft Mater.* 4 [2-4] (2006) 143-64.

-
- [41] P. Scherrer, Göttinger. Nachr. Math. Phys., 2 (1918) 96.
 - [42] B. Sundman, B. Jansson, J.O. Anderson, CALPHAD 9 (1985) 153.
 - [43] T. Ozawa, Polymer 12 (1971)150.
 - [44] K. Matusita, S. Sakka, Y. Matsui, J. Mat. Sci. 10 (1975) 961.
 - [45] K. Matusita, S. Sakka, Phy. Chem. Glasses 20 (1979) 81.
 - [46] K. Matusita, S. Sakka, J. Non-Cryst. Solids 38-39 (1980) 741.

Crystallization kinetics of Si_3N_4 in Si–B–C–N polymer-derived ceramics

A.H. Tavakoli, J.A. Golczewski, J. Bill

Abstract

In order to study the crystallization kinetics of $\beta\text{-Si}_3\text{N}_4$ in Si–B–C–N polymer-derived ceramics, the amorphous ceramics with composition $\text{SiC}_{1.6}\text{N}_{1.0}\text{B}_{0.4}$ were synthesized and then isothermally annealed at 1700, 1775 and 1850°C for different time periods ranging up to 75 h. The integrated intensities of $\beta\text{-Si}_3\text{N}_4$ X-ray diffraction (XRD) patterns were used to examine the course of crystallization. The average size of the Si_3N_4 nanocrystallites was analyzed by means of the XRD measurements and energy-filtering transmission electron microscopy (EFTEM). It was realized that the nanocrystallite dimensions change insignificantly within the time period of crystallization; however, they depend significantly on the temperature. Subsequently, the formal description of the phase transformation kinetics has been applied to analyze the $\beta\text{-Si}_3\text{N}_4$ crystallization kinetics. The experimental data have been analyzed equally with and without considering the incubation time for the initiation of the crystallization process. Assuming the Arrhenius law for the temperature dependence of the crystallization rate constants, similarly large activation energies in the range of 11.5 eV were estimated in both cases. Consequently, continuous nucleation and diffusion controlled growth have been concluded as the main mechanisms of the crystallization process. The activation energy of nucleation was estimated almost three times larger than the activation energy of the growth process. This result points at the crucial role of the nucleation rate in the crystallization kinetics of $\beta\text{-Si}_3\text{N}_4$.

4.1. Introduction

The extraordinary high temperature stability [1,2] as well as the remarkable high creep resistance of Si–B–C–N Polymer-derived ceramics (PDCs) [3] are two main features which signify the potential application of these materials as advanced engineering ceramics.

In general, as-thermolized Si–B–C–N PDCs reveal an amorphous structure at temperatures $T < 1300^{\circ}\text{C}$ while further annealing of the materials at elevated temperatures leads to the formation of crystalline phases. The crystallization of the amorphous state can influence physical and mechanical properties of these ceramics. In this connection, it was shown by Kumar et al. [4] that the Si–B–C–N ceramic samples including nanocrystalline SiC and Si₃N₄ exhibit a higher creep resistance than the corresponding amorphous sample. Moreover, identification and control of the crystallization process can be regarded as an effective way for the microstructural design of these ceramics. Using this approach, a wide variety of nanocomposites can be fabricated including different crystalline phases and a variable volume fraction of the constituent phases as well.

The Si–B–C–N PDCs containing 8-10 at. % of boron, which exhibit an excellent thermal stability, have been mostly considered for the study of the crystallization behavior [5-12]. These ceramics are generally located within the limits of the four-phase region SiC-Si₃N₄-BN-C of the quaternary Si–B–C–N system [13]. According to the quantitative description of phase separation, a particular structural feature common for the as-thermolized Si–B–C–N PDCs is Si–C–N domains related with regions of amorphous B–N–C domains containing boron, nitrogen and carbon [14]. The B–N–C domains composed of stacked layers retain their amorphous feature even after long-term annealing at high temperatures [6,8,9]. XRD investigations reveal a two-stage crystallization process where SiC is the first crystalline phase within the amorphous structure. Subsequent annealing of the ceramic samples at higher temperatures results in the formation of crystalline Si₃N₄ [8, 15-17]. The TEM analysis reveals the nano-sized nature of both crystalline phases [6,7,9,12]. Moreover, the nanocrystalline SiC emerges with much smaller dimensions than the nanocrystalline Si₃N₄ as shown by TEM [7,12]. Further investigations using quantitative XRD analysis indicate the crystallization of SiC in two stages [18,19]. Accordingly, the second stage of SiC crystallization

coincides with the formation of the crystalline Si_3N_4 . Recently, the thermodynamic aspect of the crystallization process was taken into account in order to explain the crystallization behavior in this system. It was shown that a simple model including thermodynamic description of the amorphous Si–C–N domains [20] together with the completely crystallized state can not satisfactorily describe the crystallization behavior of Si–B–C–N PDCs [17]. However, an extended model based on assumption of the metastable phase equilibria including amorphous and nanocrystalline phases [21,22] can account for the observed two-stage crystallization process [19]. Consequently, it was shown that the increase of the nanocrystalline SiC phase fraction at the first stage of the crystallization can not be considered as a process controlled purely by kinetics. In fact, the progress of the crystallization in this stage is the consequence of a continuous change in the metastable phase equilibria between amorphous Si–C–N domains and nanocrystalline SiC. On the contrary, the increase of the crystalline Si_3N_4 phase fraction is estimated to be purely controlled by kinetics [19].

In the present study, the formation kinetics of Si_3N_4 in the ceramic with a chemical composition of $\text{SiC}_{1.6}\text{N}_{1.0}\text{B}_{0.4}$ is reported. The growing amount of the nanocrystalline Si_3N_4 is determined with quantitative XRD studies and analyzed using the classical kinetic theory for the description of isothermal phase transformations. Furthermore, the dependence of the crystallite size on time and temperature is studied by XRD and EFTEM. Subsequently, the obtained results are discussed together with the existing information on the crystallization of Si–B–C–N PDCs in order to determine the mechanisms controlling the process of nucleation and growth. Finally, a better understanding of the separate role of nucleation and growth in the crystallization kinetics is provided.

4.2. Experimental Procedures

4.2.1. General remarks

The ceramics with a chemical composition of $\text{SiC}_{1.6}\text{N}_{1.0}\text{B}_{0.4}$ were obtained by direct thermolysis of hydroborated poly(methylvinylsilazane) as the polymer precursor (see Ref. [15, 23] for detailed information on the synthesis method) at 1100°C in quartz Schlenk tubes in a flowing argon atmosphere (heating rate $25\text{--}1100^\circ\text{C}$: $1^\circ\text{C}/\text{min}$ followed by a dwell time of 4 h). The as-obtained large ceramic particles in a size

between 1-3 mm were isothermally heat treated at various temperatures $T = 1700, 1775$ and 1850°C for different time periods ranging between 0.1 h and 75 h (heating rate: $25^{\circ}\text{C}/\text{min}$; cooling rate $T \geq 1200^{\circ}\text{C}$: $-120^{\circ}\text{C}/\text{min}$, $T < 1200^{\circ}\text{C}$: $-25^{\circ}\text{C}/\text{min}$). Annealing of the samples was carried out in a graphite furnace using graphite crucibles under nitrogen atmosphere (1bar).

Chemical analysis of nitrogen was performed using the equipment ELTRA ONH-2000 based on the combustion technique.

4.2.2. X-ray diffraction analysis

X-ray diffraction (XRD) measurements were carried out with a Philips unit using $\text{Cu-K}\alpha_1$ radiation (40 kV / 40 mA) equipped with X'Pert accelerator (position-sensitive Si-strip detector) in order to do quantitative analysis of the as-obtained diffraction patterns. Therefore, the following conditions were considered in terms of the sample preparation and the measurement parameters as well. As-annealed particles were milled to reach very fine powders with the average size of 1-2 μm . Then, 10 mg of the as-milled powders were dispersed in Toluene using ultrasonication. Subsequently, a thin layer of powders with diameter of 15 mm and thickness of $\sim 30 \mu\text{m}$ was formed on surface of a single crystalline silicon wafer by sedimentation. In order to observe a better precision during XRD measurement, the step size of $\sim 0.01^{\circ}$ and the counting time of 600 sec./step was applied. Further investigations concerning the quantitative evaluation of the XRD data were performed using the *ProFit* software.

4.2.3. TEM investigations

TEM specimens were prepared by Tripod polishing followed by Ar-ion milling. The samples were cut into slabs of 1-2 mm^2 . Then, cross-section specimens were glued to a pyrex specimen holder. A *Multipreparation System* was applied for Tripod polishing using diamond-lapping films. Polishing was performed until a wedge angle of $1-2^{\circ}$ was introduced. Owing to a very brittle nature of the ceramics, further polishing of samples was avoided. After detaching of the specimen holder, specimens were mounted on a Mo-Ring. The final thinning of specimens was carried out by Ar-ion beam bombardment in a Gatan PIPS at an angle of 8° and the ion energy of 3 keV for 1-2 h.

A Zeiss EM 912Ω with LaB₆ cathode operating at 120 kV equipped with an imaging omega filter was used for the conventional TEM and EFTEM investigations. The elemental mapping of carbon was obtained using the three window method (two images for the background of the EEL spectrum and a third image above the carbon K-edge, 284 eV, containing the elemental specific signal). The energy slit width was adjusted to 30 eV for the element carbon. This allowed using exposure times between 2 and 10 s.

4.3. Results and Discussion

4.3.1. Course of crystallization

4.3.1.1. Growing amount of crystalline Si₃N₄

In order to investigate the crystallization of Si₃N₄ in the SiC_{1.6}N_{1.0}B_{0.4} ceramic, the thermal stability of the material should be taken into account. The corresponding result of the high temperature thermal gravimetric analysis (HT-TGA) investigated recently [17] proves the stability at temperatures $T \leq 1850^\circ\text{C}$. Consequently, the temperatures $T = 1700, 1775$ and 1850°C were selected for the isothermal crystallization study of Si₃N₄ in SiC_{1.6}N_{1.0}B_{0.4}. It was already shown that the β modification of Si₃N₄ is formed in the case of SiC_{1.6}N_{1.0}B_{0.4} [17]. Fig. 4.1 exemplarily exhibits the intensity of the characteristic β -Si₃N₄ XRD peak located at $2\theta = 27.06^\circ$ growing with time at selected temperatures. Considering the XRD pattern measured for the ceramic sample annealed at 1700°C for 15h (Fig. 4.1(a)), no Si₃N₄ crystallization can be detected. As expected, the increase of time leads to the initiation and progress of the crystallization process. As shown in Fig. 4.1(b) and 4.1(c), the emergence of the Si₃N₄ crystallites is not detected after 2 and 0.17 h annealing at 1775 and 1850°C , respectively. Moreover, the time period for development of the crystalline volume fraction decreases significantly with increasing temperature.

For a quantitative analysis of crystallization, the crystallized volume of Si₃N₄ phase was assumed proportional to the integrated intensity $I_{\text{Si}_3\text{N}_4}(t)$ of a single XRD peak at temperature T . Therefore, the normalized volume fraction of a crystalline phase $X_{\text{Si}_3\text{N}_4}(t) = I_{\text{Si}_3\text{N}_4}(t) / I_{\text{Si}_3\text{N}_4}^{\text{max}}$ was estimated where $I_{\text{Si}_3\text{N}_4}^{\text{max}}$ is the corresponding value for the complete crystallization of the Si₃N₄ phase and should not change after further

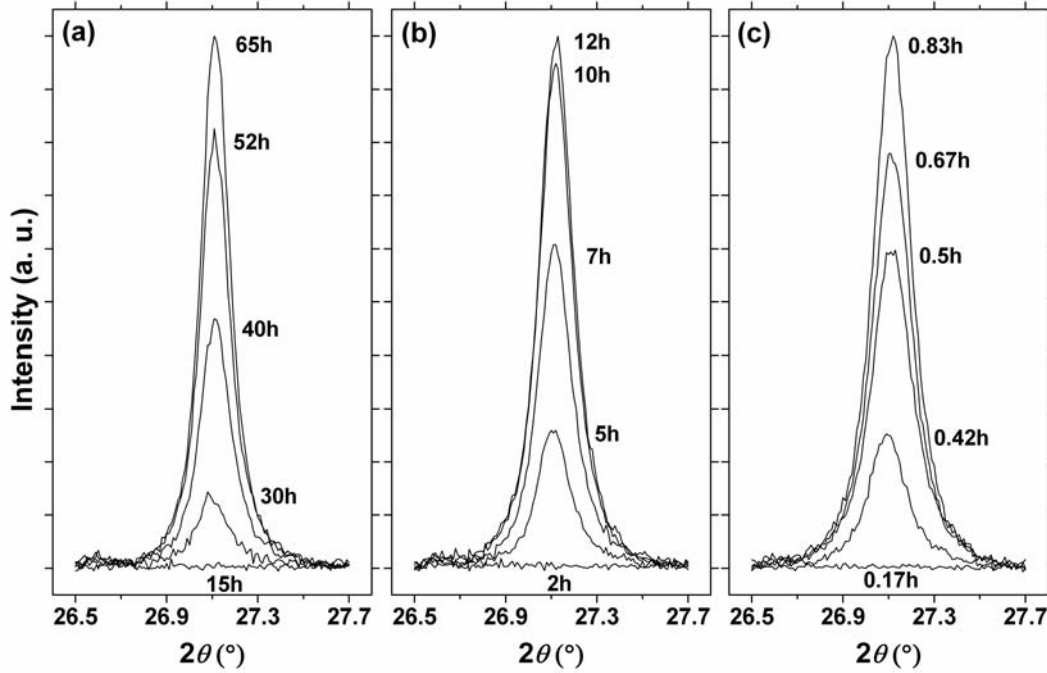


Fig. 4.1. Exemplary XRD peaks corresponding to the most intensified diffraction line of β - Si_3N_4 dependent on the annealing time of amorphous $\text{SiC}_{1.6}\text{N}_{1.0}\text{B}_{0.4}$ PDCs at different temperatures: (a) 1700°C; (b) 1775°C; (c) 1850°C.

annealing of the sample at temperature T . Three single peaks corresponding to β - Si_3N_4 were selected for more accurate quantitative analysis of the growing Si_3N_4 phase fraction. These peaks are located at $2\theta = 13.44, 23.39$ and 27.06° , respectively, and one of them is shown in Fig. 4.1. To calculate the integrated intensity of the investigated peaks ($I_{\text{Si}_3\text{N}_4}$), the Pseudo-Voigt function was fitted to the measured XRD data. Subsequently, the values $X_{\text{Si}_3\text{N}_4}$ were calculated for each single peak and the average of the obtained values $X_{\text{Si}_3\text{N}_4}$ was considered as the volume fraction of crystalline β - Si_3N_4 at time t . The achieved results are presented in Fig. 4.2 where the estimated volume fraction of the crystalline Si_3N_4 (black filled circles) are displayed as a function of time at various temperatures. The crystallization course is estimated to take 65 h at 1700°C because further heat treatment of the ceramics does not show any increase in the volume fraction of crystalline β - Si_3N_4 . With the increase of the isothermal annealing temperature to 1775 and 1850°C, the time required for complete Si_3N_4 crystallization

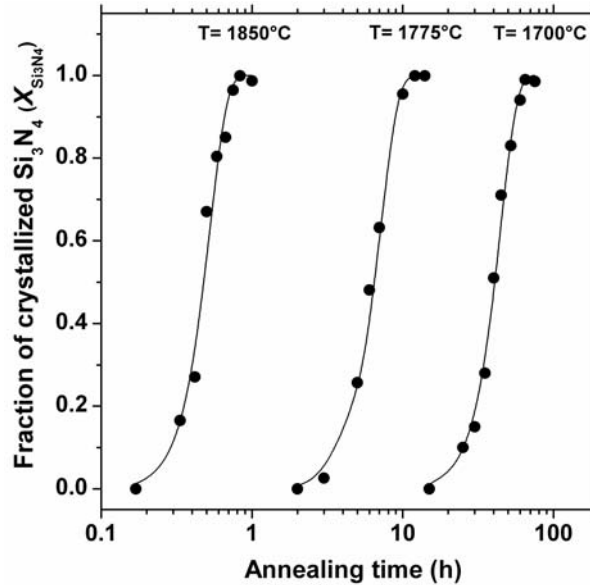


Fig. 4.2. Volume fraction of crystallized Si_3N_4 (●) versus time observed after isothermal annealing of $\text{SiC}_{1.6}\text{N}_{1.0}\text{B}_{0.4}$ PDCs at variable temperatures. A typical error value is estimated to be ± 0.05 . Solid lines are associated with fit of data by Eq. (4.2).

reduces to ~ 12 and 0.83 h, respectively (see Fig. 4.2). To achieve the information regarding the thermal stability of the ceramic samples in the course of isothermal heat treatment, chemical analysis was performed in the case of the fully crystallized samples. The obtained results are given in Table 4.1. As observed, the average values of nitrogen (wt. %) measured for the heat treated samples are comparable with the corresponding value measured for the as-thermolyzed sample (20.8 wt. %). This finding verifies the chemical stability of the ceramic samples during the crystallization process of Si_3N_4 .

4.3.1.2. Growth of crystallite dimensions

The average size of Si_3N_4 crystallites was studied in the time period of crystallization for various temperatures in order to obtain the time and temperature dependence of the Si_3N_4 crystallite dimensions. For this purpose, the XRD data were

Table 4.1. Elemental analysis of nitrogen in $\text{SiC}_{1.6}\text{N}_{1.0}\text{B}_{0.4}$ with various thermal histories.

Annealing condition	As-thermolyzed	1700°C - 65h	1775°C - 12h	1850°C - 0.83h
Nitrogen content (wt. %)	20.8 ± 0.8	21.2 ± 0.5	20.5 ± 0.5	21.6 ± 0.5

used to analyze the average crystallite size, $\langle d \rangle$, using the Scherrer formula [24]:

$$\langle d \rangle = \frac{0.9\lambda}{B(2\theta)\cos(\theta)}, \quad (4.1)$$

where $\lambda=0.1540$ nm is the wave length of the applied Cu-K α_1 radiation, B is full-width at half maximum (FWHM) of the corresponding peak, and θ is Bragg angle at the position of the peak. The same single peaks investigated for the analysis of the phase volume fraction were used for the calculation of the crystallite dimensions. The FWHM of each diffraction line was calculated with fit of XRD data by the Pseudo-Voigt function. The instrumental peak broadening was subtracted from the calculated data estimated using LaB $_6$ as a standard sample. The obtained results are presented in Fig. 4.3 where the average crystallite size of β -Si $_3$ N $_4$ is plotted versus the time at various temperatures. Average crystallite dimensions $\langle d \rangle \approx 69 - 78$ nm were calculated for the course of crystallization at 1700°C. Values of $\langle d \rangle$ were determined to be 54-58 and 38-45 nm with increasing the isothermal annealing temperature to 1775 and 1850°C, respectively. These results reveal that the values of $\langle d \rangle$ do not increase remarkably within the crystallization period at constant temperature whereas a significant decrease of $\langle d \rangle$ with increasing temperature is detected.

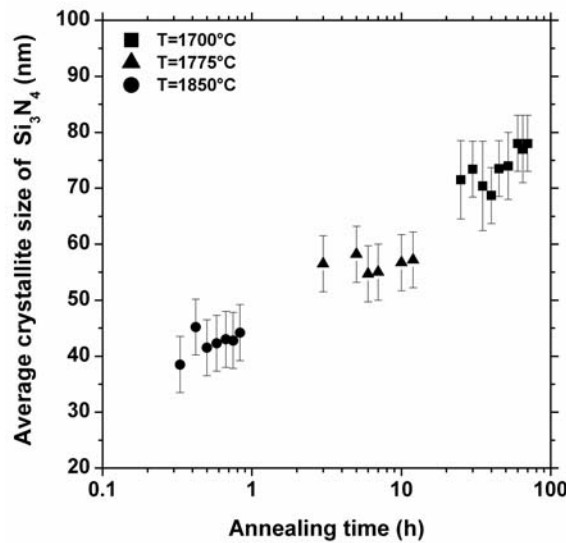


Fig. 4.3. Average crystallite dimensions of β -Si $_3$ N $_4$ during the isothermal process of crystallization within SiC $_{1.6}$ N $_{1.0}$ B $_{0.4}$ PDCs for various temperatures.

The dependence of the Si_3N_4 grain size on the temperature was also investigated by conventional TEM and EFTEM. Fig. 4.4(a) exhibits a TEM bright field image of the fully crystallized $\text{SiC}_{1.6}\text{N}_{1.0}\text{B}_{0.4}$ sample obtained after annealing at 1700°C for 65h. To distinguish the Si_3N_4 crystallites from coexisting SiC crystallites, the elemental distribution of carbon was investigated by EFTEM measurements. The elemental distribution image of carbon corresponding to the bright field image (Fig. 4.4(a)) is shown in Fig. 4.4(b). Since the amorphous B–N–C matrix and crystalline SiC include certain concentrations of carbon, the bright and grey regions in Fig. 4.4(b) manifest the existence of carbon containing phases; however, the crystalline Si_3N_4 appears in black color using the carbon map. The microstructure of the $\text{SiC}_{1.6}\text{N}_{1.0}\text{B}_{0.4}$ sample annealed at 1850°C for 0.83h was also studied in order to compare the crystallite dimensions of Si_3N_4 in the fully crystalline state achieved at variable temperatures. A TEM bright field image of the ceramic sample annealed at 1850°C and the corresponding elemental distribution image of carbon are shown in Fig. 4.4(c) and 4.4(d), respectively. These images were taken using the same magnification applied for the TEM imaging of the sample annealed at 1700°C . The smaller dimensions and larger number of the Si_3N_4 crystallites are recognized in the EFTEM image of the sample annealed at 1850°C (Fig. 4.4(d)) as compared to the one of the sample annealed at 1700°C (Fig. 4.4(b)). To get detailed information, the average dimensions of 250 grains were counted for each sample using the EFTEM images taken from variable regions of the microstructure. The grain size distribution of Si_3N_4 for two investigated samples is shown in Fig. 4.4(e). Furthermore, the obtained histograms were fitted by the normal function (dash lines in Fig. 4.4(e)). Consequently, the average crystallite size of Si_3N_4 is estimated to be 70-75 and 40-45 nm for the samples annealed at 1700 and 1850°C , respectively. These values are consistent with those obtained from the XRD measurements (Fig. 4.3) and justify the remarkable temperature dependence of the average crystallite dimensions. Moreover, the consistency of the crystallite size range obtained from XRD and EFTEM analyses confirms using the Scherrer formula (Eq. (4.1)) in which the role of micro-strain on the XRD peak broadening is disregarded.

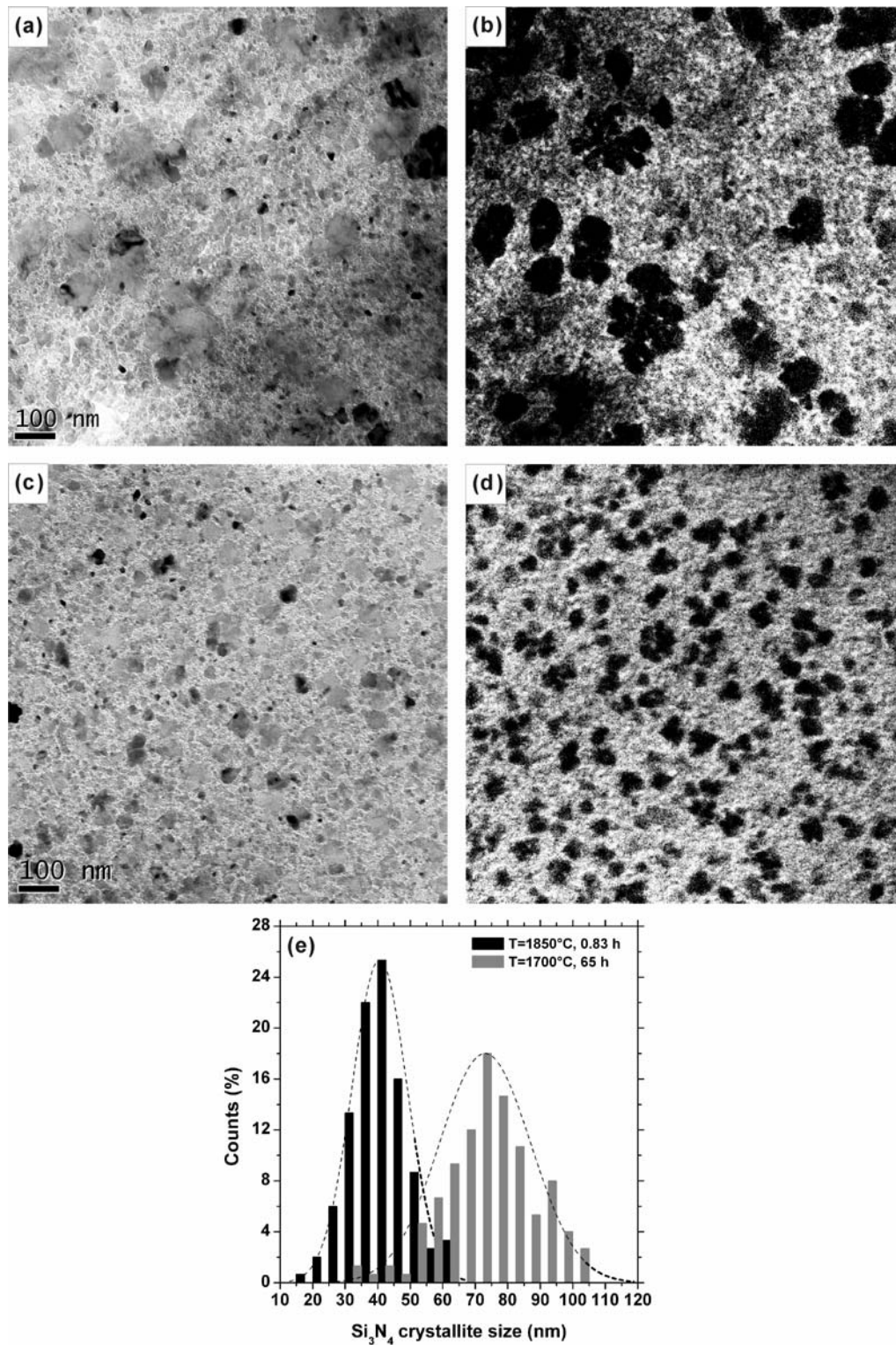


Fig. 4.4. Conventional TEM and EFTEM images of $\text{SiC}_{1.6}\text{N}_{1.0}\text{B}_{0.4}$ ceramics: (a) bright field image after annealing at 1700°C for 65h, (b) elemental map of carbon for the image (a), (c) bright field image after annealing at 1850°C for 0.83h, (d) elemental map of carbon for the image (c), (e) Si_3N_4 crystallites size distribution as determined from the EFTEM images of the fully crystallized samples obtained at 1700 and 1850°C . Black regions in the images (b) and (d) represent crystallites of $\beta\text{-Si}_3\text{N}_4$.

4.3.2. Kinetic analysis of crystallization

The kinetics of the β -Si₃N₄ crystallization in SiC_{1.6}N_{1.0}B_{0.4} was investigated using the classical kinetic theory developed by Johnson, Mehl, Avrami and Kolmogorov (JMAK-theory) [25-29]. Accordingly, the volume fraction of crystalline Si₃N₄ ($X_{\text{Si}_3\text{N}_4}$) as a function of time t is expressed as

$$X_{\text{Si}_3\text{N}_4}(t) = 1 - \exp(-(kt)^n), \quad (4.2)$$

where k is a temperature dependent effective rate constant of the crystallization process comprising both nucleation of the crystallites and the crystal growth and n is the JMAK exponent which effectively depends on the type of crystallite nucleation (site saturation or continuous), dimensionality of growth and growth controlling mechanism. Fitting Eq. (4.2) with the obtained data (black filled circles in Fig. 4.2) gives the sigmoid curves indicated in Fig. 4.2. The kinetic parameters (rate constant and JMAK exponent) derived from the analysis are given in Table 4.2. The values of JMAK exponent $n = 4.1 \pm 0.2$, 3.9 ± 0.2 , and 3.8 ± 0.3 were obtained in the case of isothermal heat treatment at $T = 1700$, 1775 and 1850°C , respectively. The natural logarithms of the obtained rate constants for the Si₃N₄ crystallization, $\ln k$, are plotted versus the reciprocal temperature, $1/T$, in Fig. 4.5. The data can be analyzed by an Arrhenius equation:

$$k = k_0 \exp\left(-\frac{Q^c}{RT}\right), \quad (4.3)$$

Table 4.2. Rate constants k , JMAK exponents n , and effective activation energy Q^c of β -Si₃N₄ crystallization. The obtained values correspond to the first series of calculations using Eqs. (4.2) and (4.3).

$T(^{\circ}\text{C})$	$k(\text{s}^{-1})$	n	$Q^c(\text{eV})$
1700 ± 15	$(6.2 \pm 0.9) \times 10^{-6}$	4.1 ± 0.2	
1775 ± 15	$(3.8 \pm 0.6) \times 10^{-5}$	3.9 ± 0.2	11.4 ± 0.5
1850 ± 15	$(5.3 \pm 0.3) \times 10^{-4}$	3.8 ± 0.3	

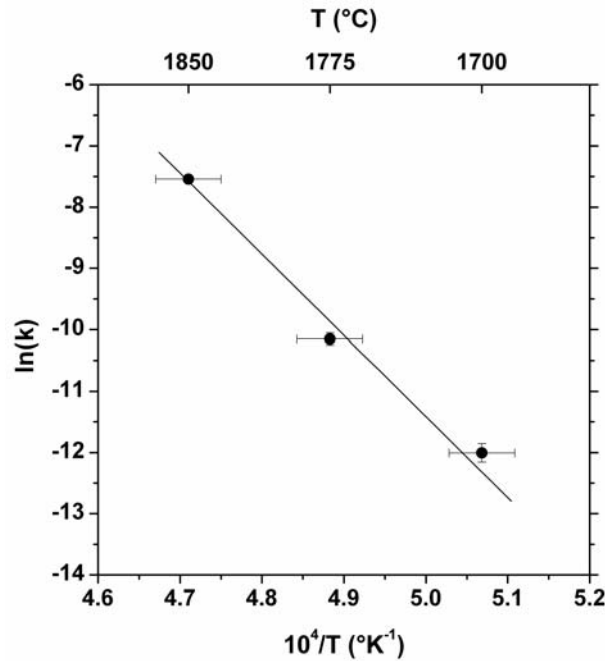


Fig. 4.5. Plot of $\ln k$ as a function of the reciprocal temperature for the crystallization of β - Si_3N_4 in $\text{SiC}_{1.6}\text{N}_{1.0}\text{B}_{0.4}$ samples (in association with the kinetic analysis without consideration of incubation time). The solid line represents the fit of data by Eq. (4.3).

where k_0 is a pre-exponential factor, Q^c is an effective activation energy of crystallization, and R is the gas constant. Accordingly, the value $Q^c = 11.4 \pm 0.5$ eV was derived with fitting of the data by Eq. (4.3) as illustrated in Fig. 4.5.

In the kinetic analysis described above, the time lag between the beginning of isothermal annealing and the emergence of the Si_3N_4 crystalline phase was considered an inherent part of the crystallization course. However, this time period can also be regarded as a temperature dependent incubation time $\tau(T)$ required for the initiation of the Si_3N_4 crystallization. In this case, the experimental data should be analyzed using the modified form of Eq. (4.2):

$$X_{\text{Si}_3\text{N}_4}(t) = 1 - \exp\left(- (k(t - \tau))^n\right), \quad (4.4)$$

where $t - \tau$ represents an effective time of the crystallization process. Based on this equation, the values τ were determined to be 15, 2 and 0.17 h for isothermal annealing at 1700, 1775 and 1850°C, respectively (Table 4.3). Fig. 4.6 exhibits the second series

of curves obtained from fitting of the experimental data using Eq. (4.4). The summary of kinetic data obtained using the later approach is presented in Table 4.3. Comparing these results with those reported before for the first series of calculations (see Table 4.2), the different values corresponding to the JMAK exponent ($n = 2.4 \pm 0.1$, 2.4 ± 0.1 and 2.5 ± 0.2) and the slightly increased values for the crystallization rate constant, k , (less than two times) should be pointed out. Moreover, the activation energy $Q^c = 11.5 \pm 0.6$ eV was obtained analyzing the temperature dependence of these rate constants by

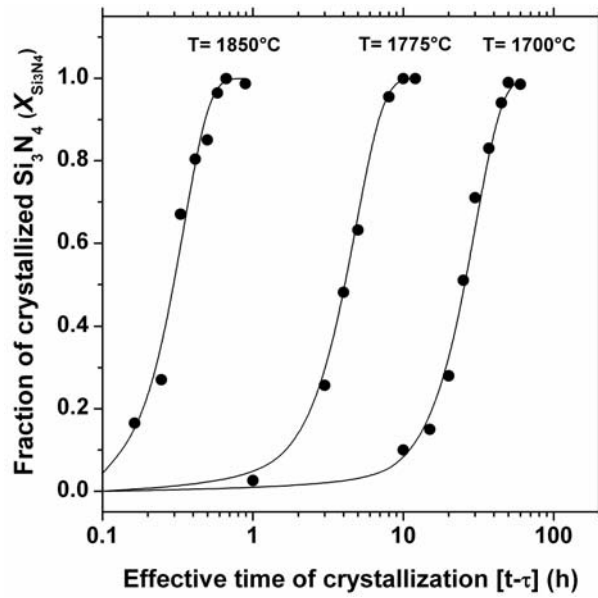


Fig. 4.6. Volume fraction of the crystallized Si₃N₄ (●) versus effective crystallization time ($t - \tau$) determined using isothermal annealing of SiC_{1.6}N_{1.0}B_{0.4} PDCs for variable temperatures. A typical error value is estimated ± 0.05 . Solid lines are associated with the fit of the data by Eq. (4.4).

Table 4.3. Rate constants k , JMAK exponents n , and effective activation energy Q^c of Si₃N₄ crystallization. The obtained values correspond to the second series of calculations using Eqs. (4.4) and (4.3).

$T(^{\circ}\text{C})$	τ (h)	k (s ⁻¹)	n	Q^c (eV)
1700 \pm 15	15	$(9.5 \pm 1.5) \times 10^{-6}$	2.4 \pm 0.1	
1775 \pm 15	2	$(5.8 \pm 0.7) \times 10^{-5}$	2.4 \pm 0.1	11.5 \pm 0.6
1850 \pm 15	0.17	$(8.0 \pm 0.8) \times 10^{-4}$	2.5 \pm 0.2	

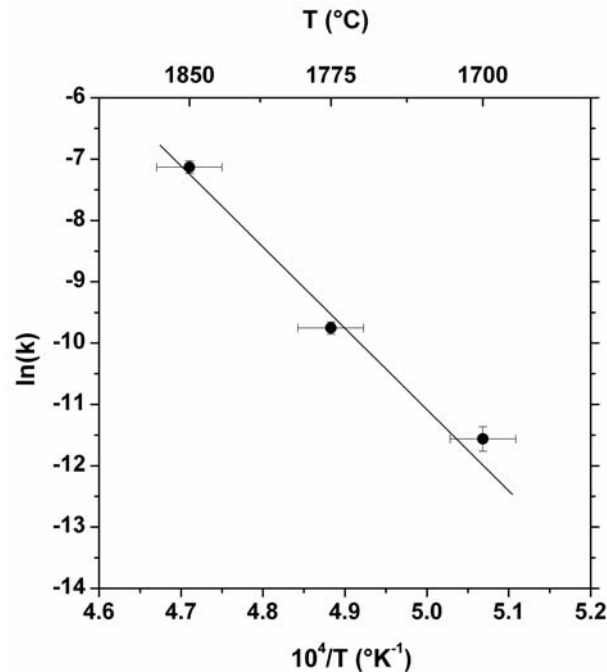


Fig. 4.7. Plot of $\ln k$ as a function of reciprocal temperature for the crystallization of β - Si_3N_4 in $\text{SiC}_{1.6}\text{N}_{1.0}\text{B}_{0.4}$ samples (in association with the kinetic analysis with consideration of incubation time). The solid line represents the fit of the data by Eq. (4.3).

an Arrhenius relation Eq. (4.3) as shown in Fig. 4.7. It draws attention that despite the differences of the transformation rate constants estimated for the both kinetic analysis (see Table 4.2 and Table 4.3), the obtained values Q° are almost identical.

4.4. Discussion

The kinetics of β - Si_3N_4 crystallization in $\text{SiC}_{1.6}\text{N}_{1.0}\text{B}_{0.4}$ was described in section 4.3.2 with and without considering the incubation times estimated for the course of isothermal annealing of the ceramic samples. Correspondingly, two different average values for the JMAK exponent ($n \approx 3.9$ and $n \approx 2.4$) were obtained which suggests two possible interpretations for the controlling mechanisms of the nucleation and growth processes. Using the formal theory of transformation kinetics [30], the value $n = 4$ implies a constant nucleation rate during the course of crystallization with a three dimensional interface-controlled growth. However, the value $n = 2.5$ suggests continuous nucleation of the crystallites as the predominant mechanism of the nucleus

formation followed with a growth process controlled by the volume diffusion of the constituent elements in the amorphous state. Therefore, consideration of the incubation period in the analysis of the crystallization kinetics leads to a different interpretation of the mechanisms controlling the progress of crystallization. In this connection, it is essential to clarify which approach yields a more reasonable explanation of the β -Si₃N₄ crystallization in the investigated Si–B–C–N PDC. As indicated in Ref. [19], the crystallization of β -Si₃N₄ is not hindered only due to the existence of a huge activation energy required for the progress of the crystallization process as reported in the present work ($Q^\circ \approx 11.5$ eV) and indeed, the high temperature stability of the amorphous state against the crystallization of Si₃N₄ is also a thermodynamic consequence of the change in the SiC nanocrystallites dimensions which slightly grow within the amorphous state as the first crystalline phase (see the literature [21,22] for detailed information). Therefore, the time lag before the emergence of the crystalline Si₃N₄ should not account as an inherent part of the crystallization course. According to what discussed above, the consideration of the incubation time, τ , for the data analysis yields more precise understanding regarding the crystallization kinetics of Si₃N₄.

Change of the average crystallite dimensions during a process of crystallization is generally connected with the mechanisms controlling the kinetics of this transformation. As shown in section 4.3.1.2, the average crystallite diameters of Si₃N₄ do not change significantly in the course of crystallization (Fig. 4.3) despite the continuous increase of crystallized phase fraction at constant temperature. The continuous Si₃N₄ nucleus formation followed by a very fast growth of as-nucleated crystallites is the most plausible scenario which justifies the observed behavior. In other words, continuous nucleation can be rationalized as the dominant mechanism of nucleus formation based on the crystallite size analysis. This conclusion also verifies the nucleation mechanism as deduced above based on the JMAK exponent values n obtained from the kinetic analysis of the crystallization process. The slight increase of the grain size indicated in Fig. 4.3 can be due to the decreased nucleation rate particularly at the end of the crystallization period. The second considerable point revealed in section 4.3.1.2 is the temperature dependence of the average crystallite dimensions. Assuming a spherical shape for the geometry of Si₃N₄ crystallites, the number of the crystallites at the end of

the crystallization course N^C can be estimated as $V^C / \left(\frac{\pi}{6}\langle d \rangle^3\right)$ where V^C is the total volume of the corresponding crystalline phase and $\left(\frac{\pi}{6}\langle d \rangle^3\right)$ represents the final volume of the corresponding single crystallite with an average diameter of $\langle d \rangle$, assuming that the crystallites are not overlapped. In principle, the total number of crystallites N^C can be approximated proportional to the number of supercritical nucleus per unit volume N^* which form within the crystallization course. Therefore, any change in the total number of N^* should influence the final average crystallite dimensions. According to the classical theory of nucleation in condensed materials [30, 31], the average number of critical nucleus per unit volume N^* with dimensions equal to the critical nucleus size ($r = r^c$) is determined by

$$N^* = N \exp\left(-\frac{\Delta G^*}{RT}\right), \quad (4.5)$$

where N is the number of atoms per unit volume of the crystalline phase, R is the gas constant, and ΔG^* is the work for nucleus formation. In the case of crystalline phase formation in an amorphous matrix, ΔG^* depends on surface free energy of the crystal / amorphous interface and the driving energy for nucleation. Under simplified assumptions, ΔG^* can be approximated as $A/\Delta T^2$ [32], where A is a constant and ΔT is the overheating in the case of our study. Therefore, the increased temperature of annealing reflects the increased value of ΔT and consequently, the decreased value of ΔG^* . According to Eq. (4.5), the decrease of ΔG^* together with the increase of the annealing temperature yield a larger number of supercritical nucleus per unit volume N^* . This corresponds to an increased number of the crystallites N^C and according to the relation of N^C and $\langle d \rangle$ as described above, smaller average dimensions of the crystallites are estimated with increasing the annealing temperature as also demonstrated by XRD and TEM investigations (Fig. 4.3 and 4.4).

The obtained results give an additional opportunity to determine the individual activation energies corresponding to the nucleation and growth processes using the

recent developments on the analysis of solid state transformations [33]. Accordingly, the effective activation energy of crystallization Q^c can be defined as

$$Q^c = \frac{(n - d/m)Q^N + (d/m)Q^G}{n}, \quad (4.6)$$

where d is the dimensionality of growth (1, 2, 3), m is the growth mode parameter ($m = 1$: interface-controlled growth; $m = 2$: diffusion-controlled growth), Q^N and Q^G are the activation energies for processes of nucleation and growth, respectively. For the particular case of continuous nucleation and three dimensional diffusion controlled growth ($n = 2.5$, $d = 3$ and $m = 2$) as specified in the present study, Eq. (4.6) can be written as

$$Q^c = \frac{2}{5}Q^N + \frac{3}{5}Q^D, \quad (4.7)$$

where Q^D is the activation energy of diffusion. In recent years, the considerable studies on the self diffusion of Si, C and N in similar amorphous Si–B–C–N ceramics were carried out with the stable isotopes using ion mass spectroscopy and consequently, the activation energies of diffusion Q^D were calculated to be in the range between 5.5-7.2 eV for all investigated elements [34-37]. Assuming the average value $Q^D \approx 6.3$ eV and considering the value $Q^c \approx 11.5$ eV as obtained in the present work, the activation energy of nucleation is calculated to be $Q^N \approx 19.3$ eV by Eq. (4.7). The value $Q^N \gg Q^D$ obviously verifies the leading role of the nucleation process in the crystallization kinetics of Si₃N₄ in the Si–B–C–N ceramic. Moreover, this large value of Q^N can be used to clarify why the dimensions of the Si₃N₄ crystallites remains nearly unchanged in the crystallization period as shown in Fig. 4.3. When one embryo of Si₃N₄ overcomes the large barrier of nucleation and one crystallite forms, the growth process proceeds very fast due to the fact that the estimated activation energy of growth is almost three times smaller than that of nucleation. Therefore, the Si₃N₄ crystallite consumes rapidly all the silicon and nitrogen atoms available in its amorphous

neighboring area and eventually gets surrounded by the amorphous B–N–C turbostratic layers and the SiC crystallites as well. Consequently, the formation of new nucleus is the necessary condition for further progress of the crystallization process. According to this scenario, the process of nucleation governs the kinetic of Si₃N₄ crystallization in SiC_{1.6}N_{1.0}B_{0.4}. Indeed, when a critical nucleus forms, it grows very fast and consequently, the average crystallite dimensions remain almost constant during the course of crystallization.

4.5. Summary and conclusions

In this work, the crystallization course of β -Si₃N₄ in a SiC_{1.6}N_{1.0}B_{0.4} polymer-derived ceramic was studied using isothermal heat treatment of the samples and subsequent determination of the crystalline phase fraction by quantitative XRD analysis. Furthermore, the time and temperature dependence of the crystallite dimensions were investigated using XRD and EFTEM measurements. Subsequently, the formation kinetics of β -Si₃N₄ was investigated and the classical equation for the isothermal analysis of phase transformations (JMAK Eq.) was used for the kinetic evaluations. The outcome of this work can be summarized as follows:

- The crystallization course lasts for ~ 65, 12 and 0.83 h at temperatures of 1700, 1775 and 1850°C, respectively.
- The average dimensions of Si₃N₄ nanocrystallites do not significantly change during the isothermal crystallization periods; however, the increase of the annealing temperature results in the noticeable decrease of the average nanocrystallite size.
- The JMAK exponent values $n \approx 3.9$ and $n \approx 2.4$ are achieved as a result of kinetic analysis without and with considering the incubation period for the initiation of the crystallization, respectively. Moreover, the value $Q^\circ \approx 11.5$ eV was calculated as the effective activation energy of the crystallization independently on consideration of the incubation time.

Using the formal theory of transformation kinetics, continuous nucleation is concluded as the dominant mechanism of Si₃N₄ crystallite nucleation. The recent findings of our group demonstrate the significant role of thermodynamics beside kinetics on the retardation of the Si₃N₄ crystallization and justifies considering the

incubation time, τ , for the kinetic calculations in the present study. Consequently, the diffusion controlled growth is deduced from the kinetic analysis. Further analysis based on the obtained kinetic mechanisms results in estimating the values Q^N and Q^D corresponding to the activation energies for the process of nucleation and growth, respectively. The value $Q^N \gg Q^D$ signifies the crucial role of the nucleation kinetics in the progress of the Si₃N₄ crystallization process. In addition, using the classical theory of nucleation, the strong dependence of the Si₃N₄ average crystallite size on the temperature was explained. Moreover, the insignificant change in the crystallite dimensions during the process of crystallization implies the continuous nucleation of Si₃N₄ nanocrystallites in accordance with the kinetic information deduced from the analysis of experimental data.

Acknowledgements

The authors wish to thank P. Gerstel for the polymer synthesis, M. Dudek for XRD measurements, U. Salzberger for TEM sample preparation, K. Hahn for providing TEM images and R. Mager for technical support. Comments of Dr. Udo Welzel for evaluation of the X-ray diffraction patterns and helpful advice of Dr. Harald Schmidt are highly acknowledged. Financial support by European Union in the framework of Marie Curie Research Training Network and International Max Planck Research School for Advanced Materials is greatly appreciated.

References

- [1] H.P. Baldus, M. Jansen, O. Wagner, *Key Eng. Mater.* 89-91 (1994) 75.
- [2] R. Riedel, A. Kienzle, W. Dressler, L. Ruwisch, J. Bill, F. Aldinger, *Nature* 382 (1996) 796.
- [3] G. Thurn, F. Aldinger, in: J. Bill, F. Wakai, F. Aldingers (Eds.), *Precursor-derived ceramics*, Wiley-VCH, Weinheim (1999) 237.
- [4] N.V. Ravi Kumar, S. Prinz, Y. Cai, A. Zimmermann, F. Aldinger, F. Berger, K. Müller, *Acta Materialia* 53 (2005) 4567.
- [5] J. Bill, F. Aldinger, *Adv. Mater.* 7 (1995) 775.
- [6] A. Jalowiecki, J. Bill, F. Aldinger, *Composites Part A* 27 (1996) 717.

- [7] Y. Cai, A. Zimmermann, S. Prinz, A. Zern, F. Phillipp, F. Aldinger, *Scripta Materialia* 45 (2001) 1301.
- [8] N. Janakiraman, M. Weinmann, J. Schuhmacher, K. Müller, J. Bill, F. Aldinger, *J. Am. Ceram. Soc.* 85 (2002) 1807.
- [9] A. Zern, J. Mayer, N. Janakiraman, M. Weinmann, J. Bill, M. Rühle, *J. Eur. Ceram. Soc.* 22 (2002) 1621.
- [10] M.A. Schiavon, G.D. Soraru, I.V.P. Yoshida, *J. Non-Crystalline Solids*, 348 (2004) 156.
- [11] S. Bernard, M. Weinmann, P. Gerstel, P. Miele, F. Aldinger, *J. Mater. Chem.*, 15 (2005) 289.
- [12] N. Janakiraman, A. Zern, M. Weinmann, F. Aldinger, P. Singh, *J. Eur. Ceram. Soc.* 25 (2005) 509.
- [13] H.J. Seifert, J. Peng, J. Golczewski, F. Aldinger, *Appl. Organometal. Chem.* 15 (2001) 794.
- [14] J.A. Golczewski, F. Aldinger, *Int. J. Mater. Res.* 97 (2006) 114.
- [15] A. Müller, P. Gerstel, M. Weinmann, J. Bill, F. Aldinger, *J. Eur. Ceram. Soc.* 20 (2000) 2655.
- [16] A. Müller, P. Gerstel, M. Weinmann, J. Bill, F. Aldinger, *J. Eur. Ceram. Soc.* 21 (2001) 2171.
- [17] A.H. Tavakoli, P. Gerstel, J.A. Golczewski, J. Bill, *J. Non-Cryst. Solids* 355 (2009) 2381.
- [18] H. Schmidt, *Soft Mater.* 2-4 (2006) 143.
- [19] A.H. Tavakoli, P. Gerstel, J.A. Golczewski, J. Bill, *J. Am. Ceram. Soc.* 93 (2010) 1470.
- [20] J.A. Golczewski, F. Aldinger, *J. Non-Cryst. Solids* 347 (2004) 204.
- [21] J.A. Golczewski, *Int. J. Mater. Res.* 97 (2006) 729.
- [22] J.A. Golczewski, *J. Ceram. Soc. Japan* 114 (2006) 950.
- [23] M. Peuckert, T. Vaahs, M. Brück, *Adv. Mater.* 2 (1990) 398.
- [24] P. Scherrer, *Göttinger. Nachr. Math. Phys.*, 2 (1918) 98.
- [25] M. Avrami, *J. Chem. Phys.* 7 (1939) 1103.
- [26] M. Avrami, *J. Chem. Phys.* 8 (1940) 212.
- [27] M. Avrami, *J. Chem. Phys.* 9 (1941) 177.

- [28] W.A. Johnson, R.F. Mehl, *Trans. AIME* 135 (1939) 416.
- [29] A.N. Kolmogorov, *Izv. Akad. Nauk SSSR Ser. Mat.* 3 (1937) 355.
- [30] J.W. Christian, *The Theory of Transformations in Metals and Alloys*, Pergamon, Oxford, 2002.
- [31] M.E. Fine, *Introduction to Phase Transformations in Condensed Systems*, Macmillan series in Mater. Sci., New York, 1964.
- [32] D.A. Porter, K.E. Easterling, *Phase transformations in Metals and Alloys*, Chapman and Hall, 1992.
- [33] A.T.W. Kempen, F. Sommer, E.J. Mittemeijer, *J. Mater. Sci.* 37 (2002) 1321.
- [34] H. Schmidt, G. Borchardt, S. Weber, S. Scherrer, H. Baurmann, A. Müller, J. Bill, *J. Appl. Phys.* 88 (2000) 1827.
- [35] H. Schmidt, G. Borchardt, H. Baurmann, S. Weber, S. Scherrer, , A. Müller, J. Bill, *Def. and Diff. For.* 194-199 (2001) 941.
- [36] H. Schmidt, *Diff. Fundamentals* 2 (2005) 59.1.
- [37] H. Schmidt, G. Borchardt, O. Kaïtasov, B. Lesage, *J. Non-Cryst. Solids* 353 (2007) 4801.

Kinetic effect of boron on the crystallization of Si_3N_4 in Si–B–C–N polymer-derived ceramics

A.H. Tavakoli, J.A. Golczewski, J. Bill

Abstract

To investigate the kinetic impact of boron on the Si_3N_4 crystallization in Si–B–C–N polymer-derived ceramics, the amorphous ceramics with compositions $\text{SiC}_{1.5}\text{N}_{0.9}\text{B}_{0.15}$ and $\text{SiC}_{1.5}\text{N}_{0.9}\text{B}_{0.24}$ including 3.7 and 6.0 at.% B, respectively, were synthesized and then isothermally annealed at temperatures ranging from 1550 to 1775°C. The course of crystallization for the α and β modifications of Si_3N_4 was quantitatively analyzed by determining the integrated intensities of the corresponding X-ray diffraction (XRD) patterns. The average dimensions of the Si_3N_4 nanocrystallites were analyzed by means of the XRD measurements. Additionally, recent results of similar investigations on the ceramic with 8.3 at.% B were also taken into account. A noticeable increase of the Si_3N_4 nanocrystallite size with increasing the boron content at constant temperature has been concluded. The kinetic analysis has demonstrated that the controlling mechanisms of the Si_3N_4 crystallization, continuous nucleation and diffusion controlled growth, are independent of the boron content. Nevertheless, the estimated activation energy of the crystallization significantly increases from 7.8 to 11.5 eV with the amount of boron ranging from 3.7 to 8.3 at.%. It is also concluded that the activation energy of the nucleation process is much larger than that of the growth process and thus the role of boron on the crystallization kinetics is mainly due to the effect of boron on the nucleation process. Discussion on the obtained results yields plausible explanations for the detected effects of boron.

5.1. Introduction

The high temperature stability of Si–B–C–N polymer-derived ceramics (PDCs) against the chemical degradation and the crystallization of the amorphous state [1-4] has drawn a considerable attention for the structural investigations of these materials since the middle of the 90s (e.g. see [5-9]).

The composition of amorphous Si–B–C–N PDCs after thermolysis is generally located within the limits of the four-phase region SiC-Si₃N₄-BN-C of the quaternary Si–B–C–N system [10]. Phase separations within the microstructure of these amorphous ceramics have been resolved based on the structural investigations by NMR measurements [5,11] and wide-angle neutron- and X-ray scattering studies [12]. Accordingly, particular structural features common for the as-thermolized materials are Si–C–N domains related with regions of amorphous domains composed of stacked layers containing carbon, boron, and nitrogen (turbostratic B–N–C domains). Further annealing of the as-thermolized Si–B–C–N PDCs at temperatures $T \geq 1300^\circ\text{C}$ leads to the formation of SiC nanocrystallites within the amorphous microstructure as the primary crystalline phase [7,13,14]. Si₃N₄ nanocrystallites emerge at significantly higher temperatures, depending on the boron content. In this connection, it was shown that the increase of boron up to ~ 8-9 at.% retards the crystallization of Si₃N₄ [14,15] whereas the crystallization of SiC is promoted [16].

A number of attempts were recently made to model the crystallization behavior of Si–B–C–N PDCs and to explain the impact of boron on the crystallization behavior. The thermodynamic model including the Gibbs energies of amorphous Si–C–N domains and the completely crystallized state cannot satisfactorily describe the crystallization behavior; however, it proves that the addition of boron increases the driving energy for the crystallization process [16,17]. Using the model of metastable phase equilibria comprising the Gibbs energies of amorphous Si–C–N domains and nanocrystalline phases [18, 19], the crystallization process was described showing a satisfactory accordance with the experimental investigations performed on Si–B–C–N PDCs [20]. Moreover, this model can also describe the promoting role of boron on the SiC crystallization. Nevertheless, modeling of the metastable phase equilibria can not explain the hindering role of boron on the Si₃N₄ crystallization. Indeed, getting more insight regarding the effect of boron on the energetics of the Si₃N₄ crystallization in Si–

B-C-N PDCs seems hard to achieve at present due to the limited detail information on crystallization of these materials.

In the present work, the crystallization kinetics of Si_3N_4 has been investigated for two ceramics with similar Si/C/N atomic ratio and variable boron content (3.7, 6.0 at.%) with the aim to get better understanding of the retarding role of boron on the Si_3N_4 crystallization. For this purpose, the volume fraction of the crystallized Si_3N_4 during isothermal annealing has been quantitatively evaluated using XRD measurements and subsequently analyzed using the classical kinetic theory for the description of isothermal phase transformations. The obtained results together with the recently reported data concerning the crystallization kinetics of Si_3N_4 for the ceramic including 8.3 at.% B [21] allow to clarify the boron impact on the activation energy of the crystallization and to determine the nucleation and growth dominant mechanisms controlling the crystallization course.

5.2. Experimental procedures

5.2.1. General remarks

The ceramics with chemical compositions of $\text{SiC}_{1.5}\text{N}_{0.9}\text{B}_{0.15}$ and $\text{SiC}_{1.5}\text{N}_{0.9}\text{B}_{0.24}$ including 3.7 and 6.0 at.% B, respectively, were obtained by direct thermolysis of the two boron-containing precursors synthesized via hydroboration of poly(methylvinylsilazane) with variable $[-\text{H}_3\text{CSi}(\text{Vi})\text{NH}-] / \text{H}_3\text{B.S}(\text{CH}_3)_2$ molar ratio of 8:1, 4:1, (Vi: $-\text{CH}=\text{CH}_2$) as described in detail elsewhere [14]. The thermolysis process was carried out at 1100°C in quartz Schlenk tubes in a flowing argon atmosphere (heating rate $25\text{-}1100^\circ\text{C}$: $1^\circ\text{C}/\text{min}$ followed by a dwell time of 4h). The as-obtained large ceramic particles in a size between 1-3 mm were isothermally heat treated at various temperatures ranging between 1550 and 1775°C for different time periods ranging from 7 h to 525 h (heating rate: $25^\circ\text{C}/\text{min}$; cooling rate $T \geq 1200^\circ\text{C}$: $-120^\circ\text{C}/\text{min}$, $T < 1200^\circ\text{C}$: $-25^\circ\text{C}/\text{min}$). Annealing of the samples was carried out in a graphite furnace using graphite crucibles under nitrogen atmosphere (1bar).

Chemical analysis of nitrogen was performed using the equipment ELTRA ONH-2000 based on the combustion technique.

5.2.2. X-ray diffraction analysis

X-ray diffraction (XRD) measurements were carried out with a Philips unit using Cu-K α_1 radiation (40 kV / 40 mA) equipped with X'Pert accelerator (position-sensitive Si-strip detector) in order to do quantitative analysis of the as-obtained diffraction patterns. Therefore, the following conditions were considered in terms of the sample preparation and the measurement parameters as well. As-annealed particles were milled to reach very fine powders with the average size of 1-2 μm . Then, 10 mg of the as-milled powders were dispersed in Toluene using ultrasonication. Subsequently, a thin layer of powders with diameter of 15 mm and thickness of $\sim 30\mu\text{m}$ was formed on surface of a single crystalline silicon wafer by sedimentation. In order to observe a better precision during XRD measurement, the step size of $\sim 0.01^\circ$ and the counting time of 600 sec./step was applied. Further investigations concerning the quantitative evaluation of the XRD data were performed using the *ProFit* software.

5.3. Results

5.3.1. Course of crystallization

5.3.1.1. Growing amount of crystalline Si₃N₄

To investigate the crystallization of Si₃N₄ in the Si-B-C-N PDCs, the high temperature stability of the ceramics should be taken into account. The corresponding results of the high temperature thermal gravimetric analysis (HT-TGA) reported in the literature [17] prove the chemical stability of SiC_{1.5}N_{0.9}B_{0.15} and SiC_{1.5}N_{0.9}B_{0.24} at temperatures $T \leq 1700$ and $T \leq 1800^\circ\text{C}$, respectively. Therefore, two sets of temperatures were selected for the isothermal heat treatment of the samples: (i) $T = 1550, 1625$ and 1700°C for the ceramic with 3.0 at.% B, (ii) $T = 1625, 1700$ and 1775°C for the ceramic with 6.0 at.% B. Figs. 1(a), 1(b) and 1(c) exhibit the XRD patterns of the ceramic samples containing 3.7, 6.0 and 8.3 at. % B, respectively, which have been isothermally annealed at $T = 1700^\circ\text{C}$ prior to the initiation of the Si₃N₄ crystallites formation. It should be noted that the crystallization behavior and the crystallization kinetics of Si₃N₄ in SiC_{1.6}N_{1.0}B_{0.36} including 8.3 at.% B was recently investigated in detail [21]. As shown in Fig. 5.1, the broad peaks in XRD patterns correspond to SiC nanocrystallites which form within the amorphous microstructure of the ceramics during the annealing period. Moreover, the time lag for the start of the Si₃N₄ crystallization course increases from ~ 2 h to ~ 15 h with increasing the boron

content from 3.7 to 8.3 at.%. As expected, the increase of annealing time leads to the initiation and progress of the Si_3N_4 crystallization. For instance, Fig. 5.2 exemplarily exhibits the intensity of the characteristic α - and β - Si_3N_4 XRD peaks located at $2\theta = 20.58$ and 27.06° , respectively, growing with time at $T = 1700^\circ\text{C}$ in the ceramic including 6.3 at.% B.

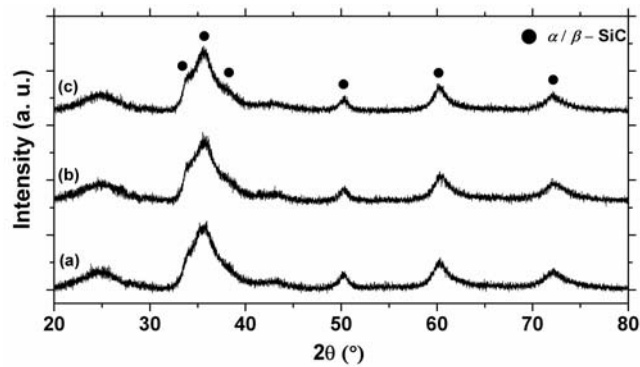


Fig. 5.1. XRD patterns of the Si-B-C-N ceramics including (a) 3.7 at.% B, (b) 6.0 at.% B and (c) 8.3 at.% B prior to the crystallization of Si_3N_4 after isothermal heat treatment at $T = 1700^\circ\text{C}$ for 2, 6 and 15 h, respectively.

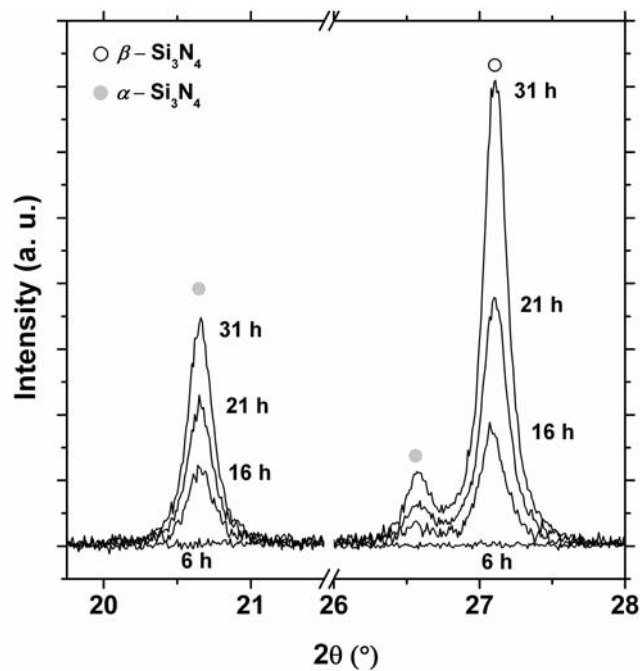


Fig. 5.2. Exemplary XRD peaks corresponding to the diffraction lines of α - and β - Si_3N_4 dependent on the annealing time of amorphous $\text{SiC}_{1.5}\text{N}_{0.9}\text{B}_{0.24}$ at constant temperature of $T = 1700^\circ\text{C}$.

The integrated intensity of the diffracted x-ray beam from a (hkl) lattice plane corresponds with the number of the (hkl) plane within a crystalline state. Moreover, the number of the (hkl) plane correlates with the corresponding crystallized volume fraction within an amorphous state. Thus for a quantitative analysis of crystallization in this study, the crystallized volume for two modifications of Si_3N_4 (α, β) was assumed proportional to the integrated intensity $I_i(t)$ ($i = \alpha, \beta$) of a single XRD peak at temperature T . Accordingly, the normalized volume fraction of a crystalline phase $X_i(t) = I_i / I_i^{\max}$ ($i = \alpha, \beta$) has been evaluated where I_i^{\max} ($i = \alpha, \beta$) is the corresponding value for the complete crystallization of the Si_3N_4 . In this connection, two peaks corresponding to α, β modifications of Si_3N_4 respectively located at $2\theta = 20.58$ and 27.06° (shown in Fig. 5.2) were selected for the quantitative analysis of the growing fraction of the phase Si_3N_4 . To calculate the integrated intensity of the investigated peaks $I_i(t)$ ($i = \alpha, \beta$), the Pseudo-Voigt function was fitted to the measured XRD data and subsequently the values X_i ($i = \alpha, \beta$) were calculated as the volume fraction of crystalline α - and β - Si_3N_4 at time t . The obtained results at $T = 1700^\circ\text{C}$ are presented in Fig. 5.3 where the estimated volume fraction of the crystalline α - and β - Si_3N_4 are plotted as a function of time. For the ceramic including 3.7 at.% B, the complete α - and β - Si_3N_4 crystallization are estimated to last 9 and 11 h, respectively. The corresponding XRD pattern is indicated in Fig 5.4(a). With increasing the boron content to 6.0 at.%, the time required for the complete α - and β - Si_3N_4 crystallization increases to ~ 31 and 36 h, respectively (see Fig. 5.3(b)). Moreover, the XRD pattern shown in Fig. 5.4(b) signifies the reduced ratio of α - / β - Si_3N_4 as compared to the XRD pattern of the completely crystallized ceramic containing 3.7 at.% B (Fig. 5.4(a)). As exhibited in Fig. 5.4(c), Si_3N_4 nanocrystallites only form in the β modification in the case of the ceramic including 8.3 at.% B. In addition, the complete crystallization course in $\text{SiC}_{1.6}\text{N}_{1.0}\text{B}_{0.36}$ lasts much longer as compared to $\text{SiC}_{1.5}\text{N}_{0.9}\text{B}_{0.15}$ and $\text{SiC}_{1.5}\text{N}_{0.9}\text{B}_{0.24}$ (see Fig. 5.3). To obtain a certainty about the thermal stability of the ceramic samples in the time period of isothermal heat treatment at $T = 1700^\circ\text{C}$, the chemical analysis was carried out for the fully crystallized samples. The obtained results are given in Table 5.1. As observed, the average values of nitrogen (wt. %) measured for the heat treated samples are comparable with the corresponding values measured for the as-thermolized samples.

This finding proves the chemical stability of the ceramic samples during the Si_3N_4 crystallization process.

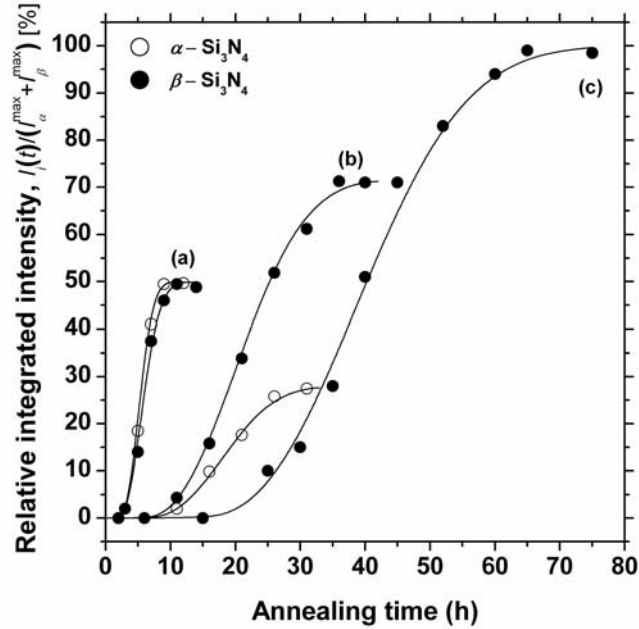


Fig. 5.3. Relative integrated intensity of the characteristic XRD peaks corresponding to α (\circ) and β (\bullet) modifications of Si_3N_4 growing with increasing the annealing time at the constant temperature of $T = 1700^\circ\text{C}$ in the Si-B-C-N ceramics with various boron content: (a) 3.7 at.% , (b) 6.0 at. % and (c) 8.3 at.%. Solid lines correspond to fit of the data by Eq. (5.2).

Table 5.1. Elemental analysis of nitrogen in the Si-B-C-N ceramics with various thermal histories.

Ceramic	$\text{SiC}_{1.5}\text{N}_{0.9}\text{B}_{0.15}$	$\text{SiC}_{1.5}\text{N}_{0.9}\text{B}_{0.24}$	$\text{SiC}_{1.6}\text{N}_{1.0}\text{B}_{0.36}$ [21]
Nitrogen content (wt. %) in the as-thermolyzed sample at 1100°C	20.7 ± 0.8	20.9 ± 1.2	20.8 ± 0.8
Nitrogen content (wt. %) after the complete crystallization at 1700°C	21.3 ± 0.5	21.0 ± 0.5	21.2 ± 0.5

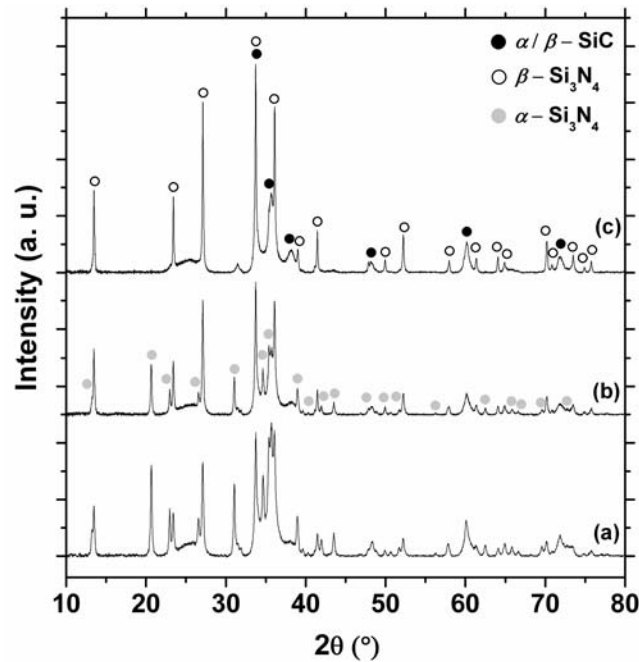


Fig. 5.4. XRD patterns of the Si-B-C-N ceramics including (a) 3.7 at.% B, (b) 6.0 at.% B and (c) 8.3 at.% B after the complete crystallization of Si₃N₄ at constant annealing temperature of $T = 1700^\circ\text{C}$. The annealing time of the corresponding ceramics is 11, 36 and 65 h, respectively.

The isothermal crystallization course of Si₃N₄ at $T = 1700^\circ\text{C}$ was described above in details. The growing amount of crystalline Si₃N₄ was also studied at other temperatures. The corresponding results are summarized in Table 5.2 where the times required for the complete Si₃N₄ crystallization are estimated at various temperatures. The results for SiC_{1.6}N_{1.0}B_{0.36} [21] are also included.

5.3.1.2. Crystallite size analysis

In order to analyze the time dependence of the Si₃N₄ crystallite dimensions as well as the influence of boron on the crystallite size, the average dimensions of β-Si₃N₄ crystallites $\langle d \rangle$ in the time period of crystallization at constant temperature $T = 1700^\circ\text{C}$ were studied. For this purpose, the XRD data were applied to investigate the values of $\langle d \rangle$ using the Scherrer formula [22]:

Table 5.2. The annealing times estimated at various temperatures for the complete crystallization of Si₃N₄ in the Si-B-C-N PDCs.

Ceramic	Temp. (°C)	Annealing time (h)
SiC _{1.5} N _{0.9} B _{0.15}	1550 ± 15	475
	1625 ± 15	60
	1700 ± 15	11
SiC _{1.5} N _{0.9} B _{0.24}	1625 ± 15	170
	1700 ± 15	36
	1775 ± 15	5
SiC _{1.6} N _{1.0} B _{0.36} [21]	1700 ± 15	65
	1775 ± 15	12
	1850 ± 15	0.83

$$\langle d \rangle = \frac{0.9\lambda}{B(2\theta)\cos(\theta)}, \quad (5.1)$$

where $\lambda=0.1540$ nm is the wave length of the applied Cu-K α_1 radiation, B is the full-width at half maximum (FWHM) of the corresponding peak, and θ is Bragg angle at the position of peak. The same peak as selected for the analysis of the β -Si₃N₄ phase volume fraction ($2\theta = 27.06^\circ$) was also used for the calculation of the crystallite dimensions. FWHM of the diffraction line was calculated with fit of the XRD data by the Pseudo-Voigt function. The instrumental peak broadening was subtracted from the calculated data estimated using LaB₆ as a standard sample. The obtained results are shown in Fig. 5.5 where the average crystallite size of β -Si₃N₄, which forms at $T = 1700^\circ\text{C}$ in the Si-B-C-N ceramics including various boron contents, is plotted versus the time.

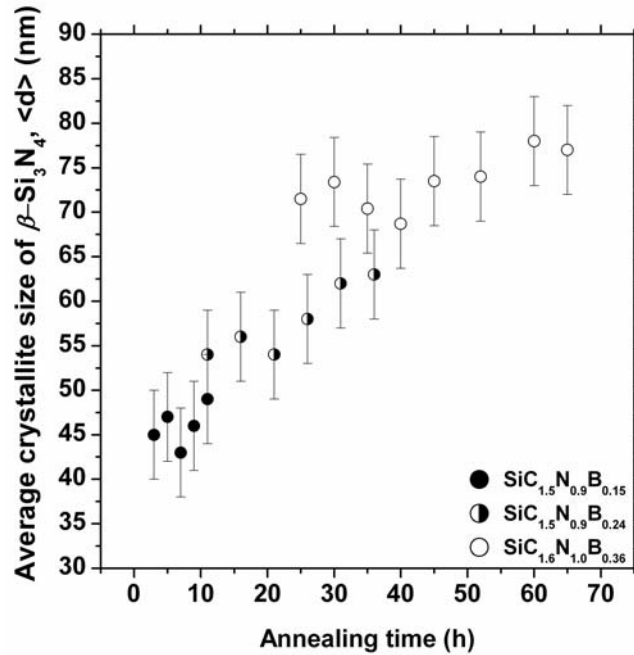


Fig. 5.5. Average crystallite size of β - Si_3N_4 forming within the Si-B-C-N ceramics with various boron content during the isothermal crystallization course at $T = 1700^\circ\text{C}$.

Accordingly, the average crystallite dimensions were calculated to be $\langle d \rangle \approx 43 - 49$ nm for $\text{SiC}_{1.5}\text{N}_{0.9}\text{B}_{0.15}$ and $\langle d \rangle \approx 54 - 63$ nm for $\text{SiC}_{1.5}\text{N}_{0.9}\text{B}_{0.24}$. In addition, the average β - Si_3N_4 crystallite size, $\langle d \rangle \approx 69 - 78$ nm, obtained for $\text{SiC}_{1.6}\text{N}_{1.0}\text{B}_{0.36}$ at the same annealing temperature is also presented in Fig. 5.5. These results reveal that the values of $\langle d \rangle$ do not remarkably increase within the crystallization period at constant temperature whereas a significant increase of $\langle d \rangle$ with increasing boron content is observed. It is worth to note that the evaluation of the single diffraction peaks by XRD single-line analysis method [23] yielded a negligible contribution of micro-strain to profile broadening and also justifies using the Scherrer formula for the crystallite size analysis.

5.3.2. Kinetic analysis of crystallization

The nucleation and growth kinetics of Si_3N_4 in $\text{SiC}_{1.5}\text{N}_{0.9}\text{B}_{0.15}$ and $\text{SiC}_{1.5}\text{N}_{0.9}\text{B}_{0.24}$ were investigated using the classical kinetic theory developed by Johnson, Mehl, Avrami and Kolmogorov (JMAK-theory) [24-28]. Accordingly, the volume fraction of crystalline Si_3N_4 X_i ($i = \alpha, \beta$) as a function of time t is expressed as

$$X_i(t) = \frac{I_i}{I_i^{\max}} = 1 - \exp\left(- (k(t - \tau))^n\right), \quad (5.2)$$

where t is the isothermal annealing time, τ is the incubation time required for the initiation of the Si_3N_4 crystallization, k is a temperature dependent effective rate constant of the crystallization process comprising both nucleation of the crystallites and the crystal growth and n is the JMAK exponent which effectively depends on the type of crystallite nucleation (site saturation or continuous), dimensionality of growth and growth controlling mechanism. Also, the term $t - \tau$ in Eq. (5.2) represents an effective time of the crystallization process. Fitting Eq. (5.2) with the obtained data corresponding to the growing fraction of crystallized Si_3N_4 at the temperature $T = 1700^\circ\text{C}$ (see Fig. 5.3) gives the sigmoid curves plotted in Fig. 5.3. The kinetic analysis for the ceramic including 3.7 at.% B yields the values of JMAK exponent $n = 2.4 \pm 0.1$ for α - Si_3N_4 and $n = 2.2 \pm 0.1$ for β - Si_3N_4 . Additionally, the rate constants of $k_\alpha = (7.2 \pm 0.4) \times 10^{-5} \text{ s}^{-1}$ and $k_\beta = (6.1 \pm 0.3) \times 10^{-5} \text{ s}^{-1}$ were determined for the formation course of crystalline phases α - and β - Si_3N_4 , respectively. For the ceramic with 6.0 at.% B, the values $n = 2.5 \pm 0.1$ and $n = 2.3 \pm 0.1$ were obtained for the α , β modifications, respectively. Moreover, the rate constants of $k_\alpha = (1.9 \pm 0.5) \times 10^{-5} \text{ s}^{-1}$ and $k_\beta = (1.6 \pm 0.3) \times 10^{-5} \text{ s}^{-1}$ were achieved. Considering the kinetic data presented above, crystallization of the phases α - and β - Si_3N_4 proceed simultaneously and can be described with nearly the same kinetic parameters. Hence, further kinetic analysis is restricted to the crystallization behavior of β - Si_3N_4 . For this reason, a linear formula derived from Eq. (5.2) has been used. Accordingly, the term $\ln(-\ln(1 - X_\beta(t)))$ plotted versus $\ln(t - \tau)$ at different annealing temperatures for the ceramics including various boron content have been fitted yielding the straight lines as shown in Fig. 5.6. The parameters (k and n) derived from the kinetic investigation are given in Table 5.3. For $\text{SiC}_{1.5}\text{N}_{0.9}\text{B}_{0.15}$, the same values of JMAK exponent, $n = 2.4 \pm 0.1$, were obtained in the case of isothermal heat treatment at $T = 1550$ and 1625°C . For $\text{SiC}_{1.5}\text{N}_{0.9}\text{B}_{0.24}$, $n = 2.2 \pm 0.1$ and 2.3 ± 0.1 were determined for annealing at $T = 1625$ and 1775°C , respectively. Furthermore, the recently reported kinetic analysis for $\text{SiC}_{1.6}\text{N}_{1.0}\text{B}_{0.36}$ gives almost the same values ($n = 2.4 \pm 0.1$ and $n = 2.5 \pm 0.2$ derived at $T = 1775$ and 1850°C , respectively) [21].

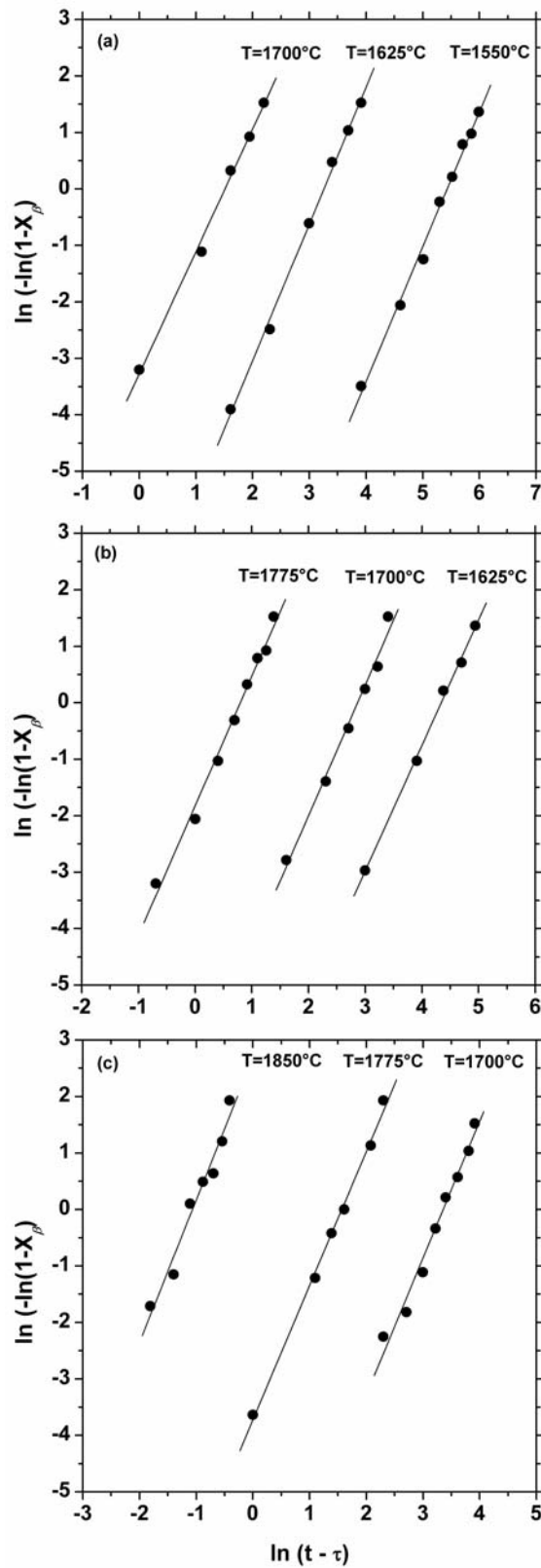


Fig. 5.6. Plot of the term $\ln(-\ln(1-X_\beta(t)))$ versus $\ln(t - \tau)$ based on the linear formula derived from Eq. (5.2) at various temperatures for (a) $\text{SiC}_{1.5}\text{N}_{0.9}\text{B}_{0.15}$, (b) $\text{SiC}_{1.5}\text{N}_{0.9}\text{B}_{0.24}$ and (c) $\text{SiC}_{1.6}\text{N}_{1.0}\text{B}_{0.36}$. Solid straight lines correspond to the linear fit of the data.

Table 5.3. Rate constants k , JMAK exponents n , and effective activation energies Q^c of β -Si₃N₄ crystallization within the Si-B-C-N ceramics including nearly the same Si/C/N ratio and variable boron content. The obtained values were derived from the kinetic analysis of the experimental data using Eqs. (5.2) and (5.3).

Ceramic	Annealing temperature (°C)	Incubation time (h)	k (s ⁻¹)	n	Q^c (eV)
	1550 ± 15	75	(1.2 ± 0.2) × 10 ⁻⁶	2.4 ± 0.1	
SiC _{1.5} N _{0.9} B _{0.15}	1625 ± 15	10	(1.1 ± 0.1) × 10 ⁻⁵	2.4 ± 0.1	7.8 ± 0.4
	1700 ± 15	2	(6.1 ± 0.3) × 10 ⁻⁵	2.2 ± 0.1	
	1625 ± 15	30	(2.6 ± 0.5) × 10 ⁻⁶	2.2 ± 0.1	
SiC _{1.5} N _{0.9} B _{0.24}	1700 ± 15	6	(1.6 ± 0.3) × 10 ⁻⁵	2.3 ± 0.1	9.0 ± 0.5
	1775 ± 15	1	(1.3 ± 0.1) × 10 ⁻⁴	2.3 ± 0.1	
	1700 ± 15	15	(9.5 ± 1.5) × 10 ⁻⁶	2.4 ± 0.1	
SiC _{1.6} N _{1.0} B _{0.36}	1775 ± 15	2	(5.8 ± 0.3) × 10 ⁻⁵	2.4 ± 0.1	11.5 ± 0.6
[21]	1850 ± 15	0.17	(8.0 ± 0.6) × 10 ⁻⁴	2.5 ± 0.2	

For further analysis, the natural logarithms $\ln k$ of the obtained rate constants k for the β -Si₃N₄ crystallization are plotted versus the reciprocal temperature, $1/T$, in Fig. 5.7. These data revealing apparent linear relation can be analyzed by an Arrhenius equation:

$$k = k_0 \exp\left(-\frac{Q^c}{RT}\right), \quad (5.3)$$

where k_0 is a pre-exponential factor, Q^c is an effective activation energy of crystallization, and R is the gas constant. As illustrated in Fig. 5.7, the data are

satisfactory described by Eq. (5.3). The obtained values of activation energies are $Q^c = 7.8 \pm 0.4$, 9.0 ± 0.5 and 11.5 ± 0.6 eV corresponding to the ceramics including 3.7, 6.0 and 8.3 at.% B, respectively.

5.4. Discussion

The kinetics analysis of β -Si₃N₄ crystallization for three ceramics with compositions of SiC_{1.5}N_{0.9}B_{0.15}, SiC_{1.5}N_{0.9}B_{0.24} and SiC_{1.6}N_{1.0}B_{0.36} was presented in section 5.3.2. As a result, the average values for the JMAK exponent $n \approx 2.3$, 2.3 and 2.4 corresponding to the ceramics with 3.7, 6.0 and 8.3 at.% B, respectively, were estimated. These nearly equal values of n imply that the controlling mechanisms of the Si₃N₄ crystallization are not essentially influenced by the amount of boron. Using the formal theory of transformation kinetics [29], the value $n = 2.5$ suggests mechanism of continuous nucleation followed with a three dimensional growth of the crystallites controlled by the volume diffusion of the constituent elements. Despite the crystallization mechanisms which appear to be independent on the boron content, really

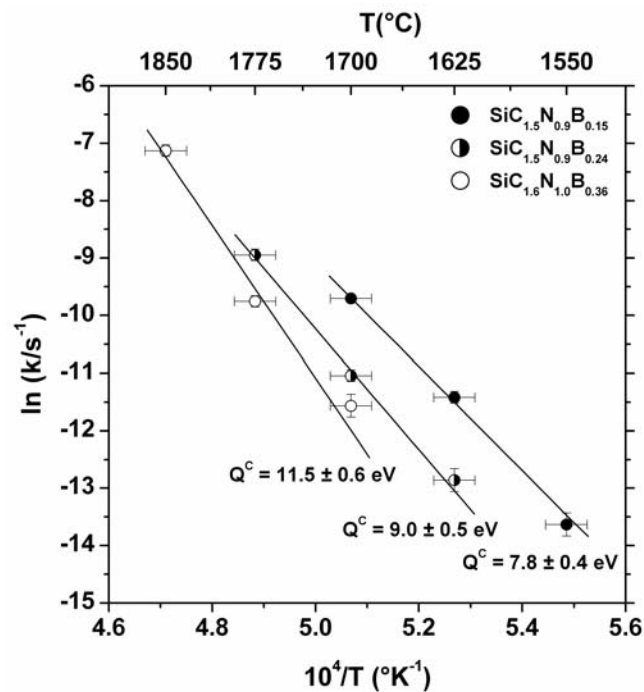


Fig. 5.7. Plot of the term $\ln(k)$ versus reversible temperature for the Si–B–C–N ceramics including nearly the same Si/C/N ratio and variable boron content. Solid straight lines are associated with fit of the data by Eq. (5.3).

different energy barriers for the Si_3N_4 crystallization have been estimated for the investigated ceramics. As displayed in Fig. 5.7, the fitted values of Q^c increases from 7.8 to 11.5 eV with the increase of boron content from 3.7 to 8.3 at.%. The obtained results allow to determine the individual activation energies corresponding to the nucleation and growth processes using the recent developments on the analysis of solid state phase transformations [30]. Accordingly, the effective activation energy of crystallization Q^c can be defined as

$$Q^c = \frac{(n - d/m)Q^N + (d/m)Q^G}{n}, \quad (5.4)$$

where d is the dimensionality of growth (1, 2, 3), m is the growth mode parameter ($m = 1$: interface-controlled growth; $m = 2$: diffusion-controlled growth), Q^N and Q^G are the activation energies for processes of nucleation and growth, respectively. For the particular case of continuous nucleation and a three dimensional diffusion controlled growth ($n = 2.5$, $d = 3$ and $m = 2$) as deduced above, Eq. (5.4) can be written as follows:

$$Q^c = \frac{2}{5}Q^N + \frac{3}{5}Q^D, \quad (5.5)$$

where Q^D is the activation energy of diffusion. In recent years, the extensive studies on the self diffusion of Si, C and N in similar amorphous Si-B-C-N ceramics including ~ 9.0 at.% B were carried out with the stable isotopes using ion mass spectroscopy. The obtained results revealed that the activation energies of diffusion Q^D for all the investigated elements are within the range 5.5-7.2 eV [31-34]. Additionally, the measurements of the self diffusion of Si in amorphous Si-C-N PDCs yield the value of $Q^D = 5.7$ eV [35]. These results demonstrate that the addition of boron does not generate any noticeable change in the activation energy of the Si diffusion within Si-C-N domains separated in Si-B-C-N ceramics. Hence, the activation energy of the N diffusion during the growth of Si_3N_4 crystallites can also be supposed as independent of the boron content. Consequently, to estimate the activation energies of nucleation using Eq. (5.5), a common average value $Q^D \approx 6.3$ eV has been assumed for the activation

energy of volume diffusion of the constituent elements in Si–C–N domains. Taking the values $Q^c \approx 7.8, 9.0$ and 11.5 eV as obtained for the ceramics containing 3.7, 6.0 and 8.3 at.% B, respectively, the corresponding values for the activation energy of nucleation Q^N were calculated to be $\approx 10.6, 13.3$ and 19.3 eV. The estimated values $Q^N \gg Q^G$ signify that the nucleation process is a main factor determining crystallization kinetics of Si_3N_4 in the Si–B–C–N ceramics. Moreover, the strong dependence of Q^N on the boron content indicates also the influence of boron on the nucleation kinetics of Si_3N_4 and consequently can be used to explain the observed impact on crystallization.

A simple way to explain the apparent role of boron on the nucleation kinetics of Si_3N_4 seems to consider an impact of boron on the structural transformations of the amorphous state as caused by interaction with components of the Si–C–N domains. Since the results of the extended structural investigations performed by means of NMR and wide angle X-ray / neutron scattering [5,11,12] have not indicated so far the existence of boron within the amorphous Si–C–N domains, the interfaces between B–N–C domains, emerging in form of turbostratic BNC_x layers, and Si–C–N domains can be regarded as the only origin of postulated interaction. This interaction should be presumably associated with existence of the Si–N–B bonds at the interface between turbostratic BNC_x layers and SiN_4 tetrahedra as schematically illustrated in Fig. 5.8. Thus the cleavage of Si–N–B bonds between B- and Si-containing structures would be necessary for the nucleation of Si_3N_4 crystallites. As a result, the energy required for the cleavage of these bonds play a role for the actual activation energy of nucleation. On the other hand, the increase of boron content at constant Si/C/N ratios in the investigated ceramics leads to the growing fraction of B–N–C domains within the ceramics microstructure [36] which means the increased interface area between B- and Si-containing domains and the growing fraction of Si–N–B bonds at the interface area as well. Therefore, for the formation of Si_3N_4 crystallites, a larger number of Si–N–B bonds should be cleaved for the ceramic including 8.3 at.% B as compared to the ceramic including 3.7 at.% of B. In other words, the increased value of Q^N for the formation of Si_3N_4 crystallites with increasing the boron content as estimated in this

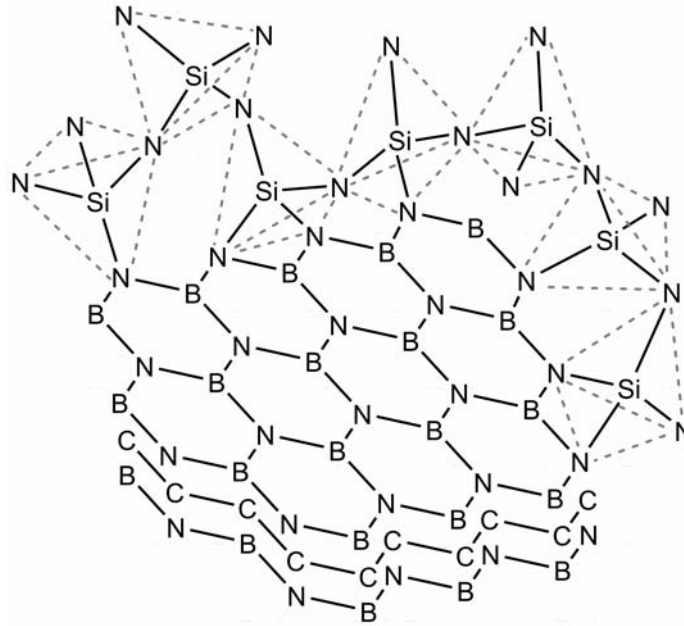


Fig. 5.8. Schematic illustration exhibiting the Si-N-B bonds which presumably form at the interface between BNC_x turbostratic layers (B-N-C domains) and Si-containing domains (SiN_4 tetrahedras) within the amorphous microstructure of Si-B-C-N PDCs.

work can be explained as a result of the growing value of the energy required for the cleavage of the developed Si-N-B bonds at the domains interfaces.

The results reported in section 5.3.1.2 reveal the increase of the Si_3N_4 average crystallite size with increasing the boron content despite the inconsiderable change of the average crystallite diameters in the time period of the isothermal crystallization (see Fig. 5.5). The nearly constant crystallite size during the progress of the crystallization process has been interpreted as a consequence of the continuous Si_3N_4 nucleus formation followed by a rapid growth of as-nucleated crystallites [21]. This conclusion also justifies the nucleation mechanism as deduced above based on the JMAK exponent values $n \approx 2.5$ obtained from the kinetic analysis of the crystallization process. The increased crystallite dimensions of Si_3N_4 with addition of boron at the constant temperature in the Si-B-C-N PDCs reflects the decreased average number of the Si_3N_4 nuclei per unit volume $N(T,t)$ with increasing the boron content. According to the classical theory of nucleation in condensed materials [29,37], $N(T,t)$, which continuously increases during the crystallization course, is significantly affected by the

term $\exp\left(-\frac{\Delta G^* + Q^N}{RT}\right)$ where ΔG^* is the free activation energy of formation of a supercritical nuclei, and R is the gas constant. Hence, the decreased value of N with addition of the boron content at constant temperature as deduces above can be regarded as a consequence of the increased value of Q^N as resulted in this work (Fig. 5.7). Moreover, the increased value of ΔG^* with increasing the boron content could also result in the decreased value of N . Since the value of ΔG^* is determined using two thermodynamic parameters (driving energy for nucleation, $\Delta\mu$, and crystalline/amorphous interface energy, γ), the decreased value of N can also be supposed as connected with the influence of boron on the thermodynamics of the Si_3N_4 nucleation.

5.5. Summary and conclusions

In this work, the crystallization course of Si_3N_4 for two Si-B-C-N polymer-derived ceramics with nearly the same Si/C/N atomic ratio and the different boron content (3.7 and 6.0 at.%) was investigated using the quantitative XRD analysis for determination of the phase fraction and dimensions of crystallites which form during isothermal heat treatment of the samples. Subsequently, the formation kinetics of Si_3N_4 crystallites was analyzed using JMAK approach widely applied for the description of isothermal phase transformations. The main aim of this attempt was to clarify the kinetic impact of boron on the crystallization of Si_3N_4 . Therefore, the recently published data concerning the crystallization kinetics of Si_3N_4 in a Si-B-C-N PDC containing 8.3 at.% B [21] was also considered for the final analysis. The findings of this study can be summarized as follows:

- For the ceramic including 3.7 at.% B, the complete crystallization lasts for ~ 475, 60 and 11 h at temperatures of 1550, 1625 and 1700°C, respectively. The corresponding crystallization times for the ceramic comprising 6.0 at.% B are estimated as ~ 170, 36 and 5 h at temperatures of 1625, 1700 and 1775°C, respectively.
- The average crystallite size of Si_3N_4 does not significantly change during the course of isothermal crystallization. However, the results of investigations at

the constant annealing temperature of 1700°C show that the increase of the boron content from 3.7 to 6.0 and 8.3 at.% leads to a considerable increase of the average nanocrystallite size from 43-49 to 54-63 and 69-78 nm, respectively.

- The crystallization process for α and β modifications of Si_3N_4 , which form in the investigated ceramics, follows almost the same kinetic behavior.
- The kinetic analysis of the β - Si_3N_4 crystallization results in the JMAK exponent values of $n \approx 2.3$, 2.3 and 2.4 for to the ceramics with 3.7, 6.0 and 8.3 at.% B, respectively. Moreover, the corresponding values for the effective activation energy of the crystallization Q^c were obtained to be ~ 7.8 , 9.0 and 11.5 eV, respectively.

Using the formal theory of phase transformation kinetics, continuous nucleation and a three dimensional diffusion controlled growth were concluded as the mechanisms of the crystallization process. Since the values of n were obtained nearly the same for the ceramics investigated, these mechanisms seem to be independent of the boron content. Further analysis allowed estimation of the approximate values Q^N and Q^G corresponding to the activation energies for the process of nucleation and growth, respectively. The values $Q^N \gg Q^G$ point to the crucial role of the nucleation kinetics in the progress of the Si_3N_4 crystallization process. The later analysis also demonstrates the significant increase of Q^N with increasing the boron content in the Si-B-C-N ceramics. This effect was attributed to the increased number of Si-N-B bonds, which presumably form at the interface between B- and Si-containing domains, with further addition of boron. The insignificant change in the crystallite dimensions during the process of crystallization signifies the continuous nucleation of Si_3N_4 nanocrystallites in accordance with the interpretation of the kinetic parameters obtained in this investigation. The dependence of the Si_3N_4 crystallite size on the boron content was suggested as a consequence of the boron influence on either the kinetics or the thermodynamics of the Si_3N_4 nucleation process.

Acknowledgements

The authors would like to thank Peter Gerstel for preparation of the polymer precursors, M. Dudek for XRD measurements and R. Mager for technical support. Comments of Dr. Udo Welzel for evaluation of the X-ray diffraction patterns are greatly appreciated. Financial support by the European Community's Sixth Framework Program through a Marie Curie Research Training Network and International Max Planck Research School for Advanced Materials is highly acknowledged.

References

- [1] K. Su, E.E. Remsen, G.A. Zank, L.G. Sneddon, *Chem. Mater.* 5 (1993) 547.
- [2] H.P. Baldus, M. Jansen, O. Wagner, *Key Eng. Mater.* 89-91 (1994) 75.
- [3] J. Bill, F. Aldinger, *Adv. Mater.* 7 (1995) 775.
- [4] R. Riedel, A. Kienzle, W. Dressler, L. Ruwisch, J. Bill, F. Aldinger, *Nature* 382 (1996) 796.
- [5] J. Schuhmacher, F. Berger, M. Weinmann, J. Bill, F. Aldinger, K. Müller, *App. Organometal. Chem.* 15 (2001) 809.
- [6] A. Zern, J. Mayer, N. Janakiraman, M. Weinmann, J. Bill, M. Rühle, *J. Eur. Ceram. Soc.* 22 (2002) 1621.
- [7] N. Janakiraman, M. Weinmann, J. Schuhmacher, K. Müller, J. Bill, F. Aldinger, *J. Am. Ceram. Soc.* 85 (2002) 1807.
- [8] M.A. Schiavon, G.D. Soraru, I.V.P. Yoshida, *J. Non-Crystalline Solids* 348 (2004) 156.
- [9] S. Bernard, M. Weinmann, P. Gerstel, P. Miele, F. Aldinger, *J. Mater. Chem.* 15 (2005) 289.
- [10] H.J. Seifert, J. Peng, J. Golczewski, F. Aldinger, *Appl. Organometal. Chem.* 15 (2001) 794.
- [11] J. Haug, P. Lamparter, M. Weinmann, F. Aldinger, *Chem. Mater.* 16 (2004) 83.
- [12] F. Berger, A. Müller, F. Aldinger, K. Müller, *Z. Anorg. Allg. Chem.* 631 (2005) 355.
- [13] A. Müller, A. Zern, P. Gerstel, J. Bill, F. Aldinger, *J. Eur. Ceram. Soc.* 22 (2002) 1631.

- [14] A. Müller, P. Gerstel, M. Weinmann, J. Bill, F. Aldinger, *J. Eur. Ceram. Soc.* 20 (2000) 2655.
- [15] A. Müller, P. Gerstel, M. Weinmann, J. Bill, F. Aldinger, *J. Eur. Ceram. Soc.* 21 (2001) 2171.
- [16] J.A. Golczewski, F. Aldinger, *J. Non-Cryst. Solids* 347 (2004) 204.
- [17] A.H. Tavakoli, P. Gerstel, J.A. Golczewski, J. Bill, *J. Non-Cryst. Solids* 355 (2009) 2381.
- [18] J.A. Golczewski, *Int. J. Mater. Res.* 97 (2006) 729.
- [19] J.A. Golczewski, *J. Ceram. Soc. Japan* 114 (2006) 950.
- [20] A.H. Tavakoli, P. Gerstel, J.A. Golczewski, J. Bill, *J. Am. Ceram. Soc.* 93 (2010) 1470.
- [21] A.H. Tavakoli, P. Gerstel, J.A. Golczewski, J. Bill, *J. Mater. Res.*, in press (DOI:10.1557/JMR.2010.0282).
- [22] P. Scherrer, *Göttinger. Nachr. Math. Phys.* 2 (1918) 98.
- [23] R. Delhez, Th.H. de Keiser, E.J. Mittemeijer, *Fresenius Z. Anal. Chem.* 312 (1982) 1.
- [24] M. Avrami, *J. Chem. Phys.* 7 (1939) 1103.
- [25] M. Avrami, *J. Chem. Phys.* 8 (1940) 212.
- [26] M. Avrami, *J. Chem. Phys.* 9 (1941) 177.
- [27] W.A. Johnson, R.F. Mehl, *Trans. AIME* 135 (1939) 416.
- [28] A.N. Kolmogorov, *Izv. Akad. Nauk SSSR Ser. Mat.* 3 (1937) 355.
- [29] J.W. Christian, *The Theory of Transformations in Metals and Alloys*, Pergamon, Oxford, 2002.
- [30] A.T.W. Kempen, F. Sommer, E.J. Mittemeijer, *J. Mater. Sci.* 37 (2002) 1321.
- [31] H. Schmidt, G. Borchardt, S. Weber, S. Scherrer, H. Baurmann, A. Müller, J. Bill, *J. Appl. Phys.* 88 (2000) 1827.
- [32] H. Schmidt, G. Borchardt, H. Baurmann, S. Weber, S. Scherrer, , A. Müller, J. Bill, *Def. and Diff. For.* 194-199 (2001) 941.
- [33] H. Schmidt, *Diff. Fundamentals* 2 (2005) 59.1.
- [34] H. Schmidt, G. Borchardt, O. Kaïtasov, B. Lesage, *J. Non-Cryst. Solids* 353 (2007) 4801.

-
- [35] H. Schmidt, G. Borchardt, S. Weber, H. Scherrer, H. Baumann, A. Müller, J. Bill, *J. Non-Cryst. Solids* 298 (2002) 232.
- [36] J.A. Golczewski, F. Aldinger, *Int. J. Mater. Res.* 97 (2006) 114.
- [37] M.E. Fine, *Introduction to Phase Transformations in Condensed Systems*, Macmillan series in Mater. Sci., New York, 1964.

Kinetic effect of boron on the thermal stability of Si-(B-)C-N polymer-derived ceramics

A.H. Tavakoli, J.A. Golczewski, J. Bill

Abstract

The isothermal mass loss of two polymer-derived ceramics with compositions $\text{SiC}_{1.4}\text{N}_{0.9}$ and $\text{SiC}_{1.5}\text{N}_{1.0}\text{B}_{0.05}$ were measured as a function of time using thermal gravimetric analysis at various temperatures ranging between 1580 and 1720°C. The process of mass loss attributed to the reaction $\text{Si}_3\text{N}_4 + 3\text{C} \rightarrow 3\text{SiC} + 2\text{N}_2^\uparrow$ takes substantially more time for the boron-containing ceramic as compared to the boron free one. The continuous formation of SiC crystallites as the product of the reaction between Si_3N_4 and C was revealed through X-ray diffraction measurements during the reaction course. The kinetics of this reaction has been studied using a generalized model for the analysis of chemical reaction kinetics. Consequently, the effective activation energies for the Si_3N_4 degradation were estimated to be 11.6 ± 0.5 eV and 17.1 ± 0.7 eV for the Si-C-N and Si-B-C-N ceramics, respectively. Moreover, the obtained results indicate that the dominant mechanisms of the Si_3N_4 degradation are strongly influenced by the presence of boron. For the Si-C-N ceramic, the chemical reaction at interfaces of the reactants and the crystallization of SiC as the reaction product were proposed to be the main probable stages controlling the progress of the investigated reaction. However, the local diffusion of C out of BNC_x turbostratic layers surrounding the Si_3N_4 nanocrystals and the gas (N_2) release from the reaction zone have been suggested to be the most plausible processes limiting the progress of the Si_3N_4 degradation for the Si-B-C-N ceramic.

6.1. Introduction

The structural and chemical stability at high temperatures [1-4], good oxidation resistance [5,6] and great creep resistance [7,8] are the main characteristics of ternary Si–C–N polymer-derived ceramics (PDCs). These properties, pointing to potential applications of these solids, have triggered the intensive research on this type of materials in the past two decades. Apparently, the temperature stability of the Si–C–N PDCs is limited and strongly depends on the particular ceramic composition. For the ceramic structures containing free carbon, the thermodynamically-controlled degradation of Si_3N_4 is expected to start at temperatures above $T = 1484^\circ\text{C}$ (at $P_{\text{N}_2} = 1 \text{ bar}$) due to the Si_3N_4 carbothermal reduction [9]:



This reaction leads to the formation of SiC and a mass loss due to the gas (N_2) evolution. For the Si–C–N PDCs with an atomic ratio of $\text{C}/\text{Si} < 1$, further degradation of Si_3N_4 is expected due to the decomposition reaction at temperatures above $T = 1841^\circ\text{C}$ (at $P_{\text{N}_2} = 1 \text{ bar}$) [9,10]:



This reaction results in the formation of molten silicon and nitrogen gas. For the Si–C–N ceramics without free carbon, the degradation of Si_3N_4 occurs only due to the thermal decomposition reaction (Eq. (6.2)).

It was found out in the middle of 90s that the Si–B–C–N PDCs containing ~ 8-10 at.% of boron reveal an extraordinary high temperature stability up to 2000°C without any noticeable sign of the Si_3N_4 degradation [2,11,12]. Moreover, the correlation between the boron content of the Si–B–C–N PDCs and the onset of the degradation temperature was denoted [13,14]. Despite the intensive structural studies using various analysis techniques e.g. X-ray and neutron scattering [15]; HRTEM [16,17] and NMR [18,19], the main reason of the increased thermal stability in the Si–B–C–N PDCs is not well understood yet. However, a number of effects have been discussed as plausible explanations of the hindering role of boron on the Si_3N_4 degradation. The widely

accepted hypotheses are generally based on the unique microstructural feature of Si-B-C-N PDCs as exemplarily shown in Fig. 1.4 (chapter 1) [16]. Considering the HRTEM image (Fig. 1.4), the Si_3N_4 and SiC crystallites are separated by the stacked layers including boron, nitrogen and carbon (turbostratic BNC_x layers). Encapsulation of Si_3N_4 crystallites by BNC_x turbostratic layers is one of the proposed explanations for the increased thermal stability [9]. In this scenario, an increase of the partial pressure of nitrogen affects the reaction temperature (Eq. 6.1). Considering the following equilibrium condition:

$$\frac{a_{\text{SiC}}^3 \cdot P_{\text{N}_2}^2}{a_{\text{Si}_3\text{N}_4} \cdot a_{\text{C}}^3} = \exp\left(-\frac{\Delta G^0}{RT_e}\right), \quad (6.3)$$

where a_i is the activity of compound i , P_{N_2} is the nitrogen partial pressure, ΔG^0 is the standard Gibbs free energy of the reaction, R is the gas constant and T_e represents the equilibrium temperature of the corresponding reaction, the value T_e will increase with increasing the value P_{N_2} . Another proposed explanation takes into account a possibility of the chemical interactions between carbon and the other two elements of BNC_x turbostratic layers (boron and nitrogen) regardless of the atomic arrangement of the constituent elements within BNC_x layers [20]. As a consequence of such an assumption, a reduced carbon activity should be considered which also results in the enhancement of the temperature T_e according to Eq. (6.3). Moreover, the hindering of the Si_3N_4 degradation can occur due to the kinetic effect of boron on the degradation process. In this connection, it was proposed that BNC_x turbostratic layers can play the role of a diffusion barrier for the reaction of Si_3N_4 and carbon [9]. This effect implies a decreased mobility of the constituent elements and consequently, the temperature of the degradation reaction (Eq. (6.1)) is shifted to a higher temperature.

Up to now, no systematic study has been reported on the impact of boron on the kinetics of the Si_3N_4 degradation in Si-(B-)C-N PDCs. Thus, this study was aimed to determine an impact of 1.3 at.% boron addition to a PDC with the composition $\text{SiC}_{1.4}\text{N}_{0.9}$ on the kinetics of the Si_3N_4 degradation. For this purpose, the mass loss resulting in the course of isothermal annealing at different temperatures was measured

by high temperature thermal gravimetric analysis (HT-TGA) for the boron free and boron-containing ceramic. Moreover, the structural evolution of the ceramics in the course of annealing was studied by means of X-ray diffraction (XRD) measurements. The obtained results were analyzed using a classical kinetic theory of isothermal chemical reactions and the kinetic parameters of the degradation process are discussed.

6.2. Experimental Procedures

6.2.1. Precursors synthesis and thermolysis

The polymer precursor for the Si–C–N ceramic, poly(methylvinylsilazane), was synthesized by ammonolysis of dichloromethylvinylsilane according to the literature [21]. The boron-containing precursor was synthesized via hydroboration of poly(methylvinylsilazane) with a $[-\text{H}_3\text{CSi}(\text{Vi})\text{NH}-] / \text{H}_3\text{B.S}(\text{CH}_3)_2$ molar ratio of 20:1 (Vi: $-\text{CH}=\text{CH}_2$). The detailed information on the hydroboration process can be found in Ref. [13]. Thermolysis of the as-obtained precursors was carried out at 1100°C in quartz Schlenk tubes in a flowing argon atmosphere (heating rate $25-1100^\circ\text{C}$: $1^\circ\text{C}/\text{min}$ followed by a dwell time of 4h). The thermolysis products with a particle size in the range of 250-500 μm were used for the further analysis.

6.2.2. Measurement techniques

6.2.2.1. Chemical composition

Chemical analysis of nitrogen, hydrogen, oxygen, and carbon was performed using a combination of different types of analysis equipment (Elemental Vario EL, ELTRA CS 800 C/S, and LECO TC-436 N/O) based on combustion techniques. Furthermore, inductively coupled plasma – atomic emission spectroscopy (ICP-AES) using a ISA Jobin Yvon JY70 Plus system was employed for the chemical analysis of silicon and boron.

6.2.2.2. Mass loss measurements

High temperature thermal gravimetric analysis (HT-TGA) was carried out employing a Bähr STA 501 equipment at constant temperatures $T = 1580, 1615, 1650, 1685, 1720^\circ\text{C}$ in 1 bar nitrogen using carbon crucibles. To avoid any mass loss before reaching the selected temperature, a two step procedure with two different heating rates

was applied (the first step at temperatures $T \leq 1100^\circ\text{C}$ with a low heating rate of $25^\circ\text{C}/\text{min}$ followed by the second step at temperatures $T > 1100^\circ\text{C}$ with a much higher heating rate of $250^\circ\text{C}/\text{min}$).

6.2.2.3. Microstructure examination

XRD measurements were carried out with a Siemens D5000/Kristalloflex unit using Cu-K α radiation (40 kV, 30 mA) equipped with a quartz primary monochromator and a position-sensitive proportional counter as diffractometer. A step size of $\sim 0.01^\circ$ and a counting time of 20 sec./step were used for a better precision.

Scanning electron microscopy (SEM) investigations were performed using a field-emission scanning electron microscope model ZEISS DSM 982 Gemini.

6.3. Results and analysis

6.3.1. Characteristics of the as-thermolized ceramics

Chemical analysis of the as-thermolized ceramics is given in Table 6.1. The main difference between the chemical composition of two ceramics is related to the boron content and as expected, the Si-B-C-N ceramic includes a slight amount of boron (0.9 ± 0.1 wt.%). Nevertheless, the Si/C/N atomic ratio is almost identical in both ceramics. XRD patterns measured for the as-thermolized ceramics are shown in Fig. 6.1. The absence of evident diffraction lines indicates a complete lack of long range atomic ordering and thus corresponds to an amorphous character of the investigated materials.

Table 6.1. Elemental analysis of the as-thermolized materials^{a,b}.

Ceramic	Si	C	N	B	O	H
Si-C-N	48.9 ± 0.8 (27.5)	28.5 ± 0.6 (37.5)	21.8 ± 0.5 (24.6)	---	0.8 ± 0.2 (0.8)	0.6 ± 0.2 (9.5)
Si-B-C-N	45.8 ± 0.4 (25.5)	28.8 ± 0.5 (37.5)	22.5 ± 0.8 (25.1)	0.9 ± 0.1 (1.3)	1.3 ± 0.3 (1.3)	0.6 ± 0.1 (9.5)

^a wt.%, at.% in parenthesis

^b The error values were calculated using the standard deviation of several (at least 5) separate measurements.

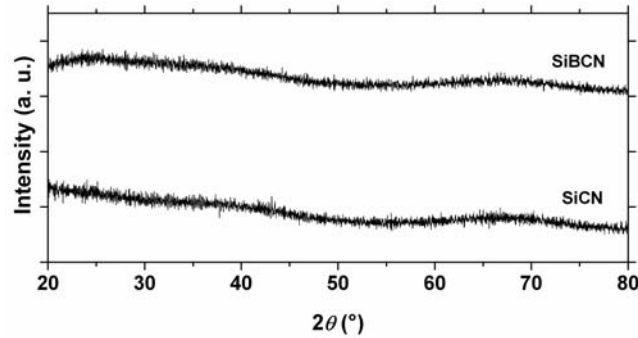


Fig. 6.1. XRD patterns of the as-thermolyzed ceramics.

6.3.2. Phase equilibria and reactions expected during thermal treatment

The phase equilibria in course of the performed thermal treatment were estimated using the available thermodynamic assessment of the Si–C–N and Si–B–C–N systems [9,10]. The resulting phase fraction diagrams computed by Thermo-Calc software [22] for the composition of the investigated ceramics (Table 6.1) are presented in Fig. 6.2. In these calculations, the hydrogen content of the ceramics was ignored assuming hydrogen exists in the form of H₂ gas at temperatures above 1050°C [10]. As shown in Fig. 6.2(a), the equilibrium state of the investigated Si–C–N ceramic (SiC_{1.4}N_{0.9}) consists at low temperatures ($T < 1484^{\circ}\text{C}$) of three phases SiC, Si₃N₄ and C, and its thermal stability is limited by the reaction of Si₃N₄ with C at the temperature $T = 1484^{\circ}\text{C}$ according to Eq. (6.1). As expressed before, this reaction results in the formation of SiC and a mass loss of the solid phase due to the gas (N₂) evolution. Consequently, the new phase equilibrium is obtained at temperatures $T > 1484^{\circ}\text{C}$ including SiC, C and N₂ as shown in the corresponding phase fraction diagram (Fig. 6.2(a)). This equilibrium state remains unchanged up to the maximum temperature of calculation $T = 2000^{\circ}\text{C}$. The phase fraction diagram computed for the investigated Si–B–C–N ceramic (SiC_{1.5}N_{1.0}B_{0.05}) is exhibited in Fig. 6.2(b). The main difference between the phase fraction diagrams computed for the both ceramics is the emergence of the additional phase (BN) and the formation of the four phase equilibrium including SiC, Si₃N₄, C and BN in the case of the boron-containing ceramic. However, the same reaction as explained above for SiC_{1.4}N_{0.9} (Eq. (6.1)) determines also the stability of

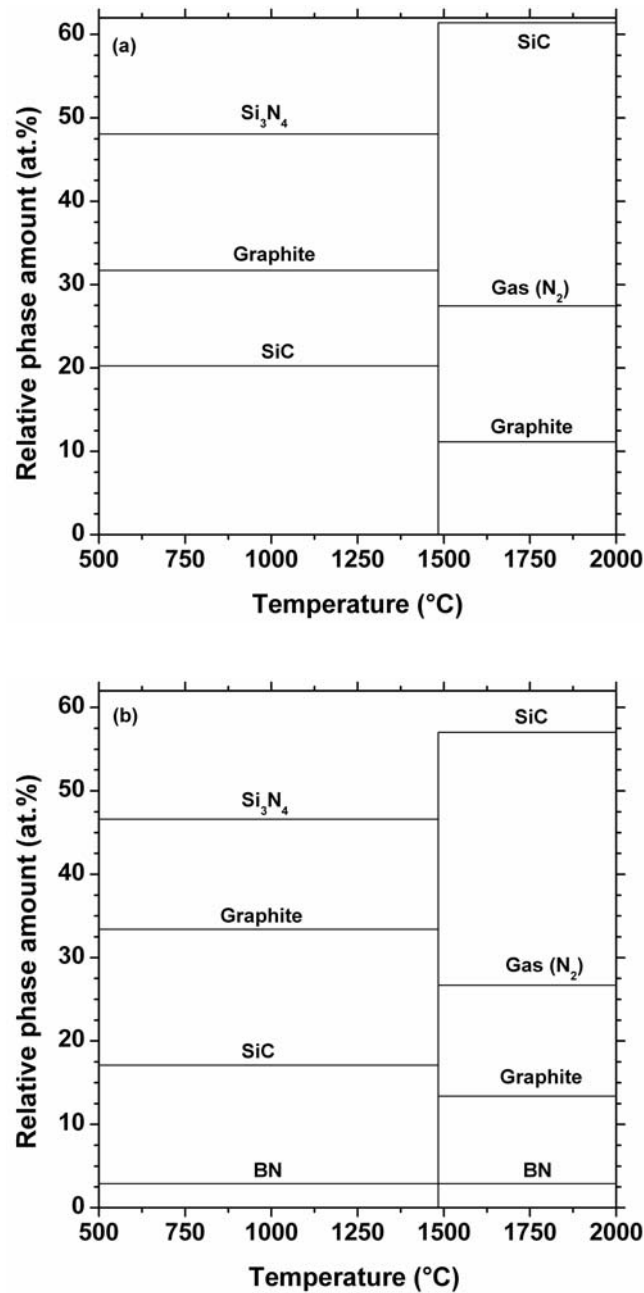


Fig. 6.2. Phase fraction diagrams computed for the Si-C-N (a) and Si-B-C-N (b) ceramics.

SiC_{1.5}N_{1.0}B_{0.05}. Since BN does not interact with the other phases within the temperature range of the computation, the BN phase amount remains unchanged and consequently, the three phase equilibrium including SiC, C, and BN is anticipated at the temperature range between 1484 and 2000°C for the boron-containing material.

6.3.3. Course of isothermal Si₃N₄ degradation

6.3.3.1. Isothermal mass loss

The isothermal mass loss of the ceramic samples ascribed to the isothermal degradation of Si_3N_4 has been measured for various temperatures $T = 1580^\circ\text{C}$, 1615°C , 1650°C , 1685°C , and 1720°C . The results are exhibited in Fig. 6.3. For the Si–C–N ceramic, the Si_3N_4 degradation saturates at all temperatures and the total mass loss was determined to be 22.5 ± 0.2 wt.% (see Fig. 6.3(a)). This value is consistent with the

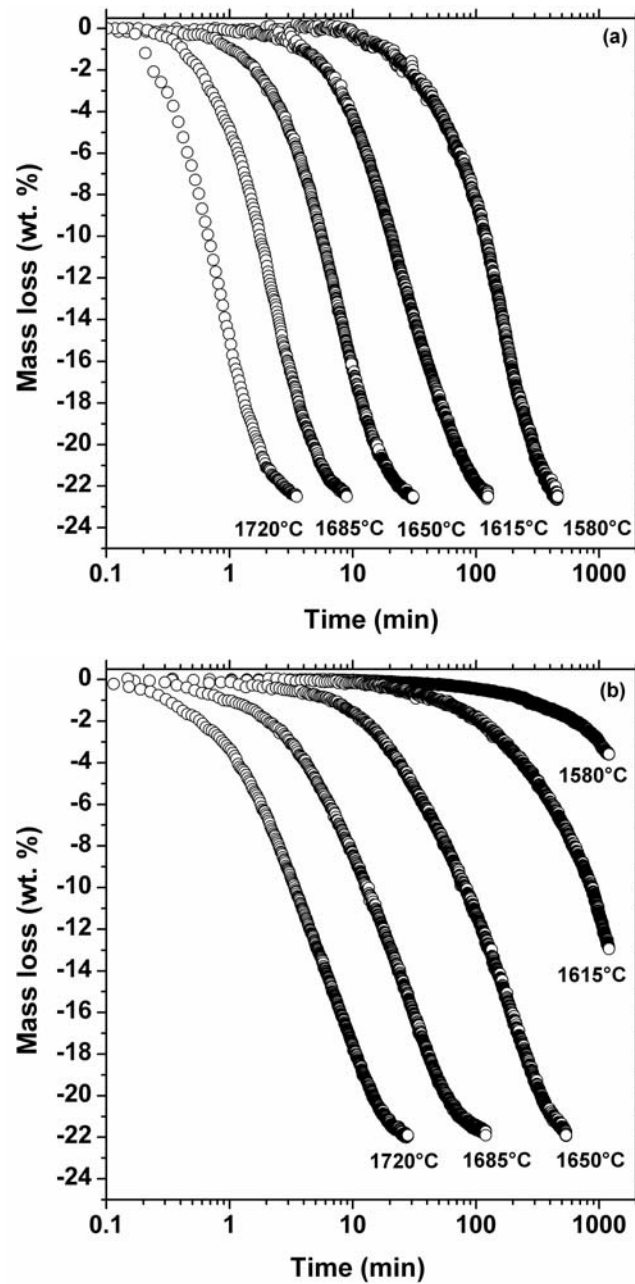


Fig. 6.3. Isothermal high temperature thermal gravimetric analysis (HT-TGA) of the Si–C–N (a) and Si–B–C–N (b) ceramics for various temperatures.

amount of nitrogen (21.8 ± 0.5 wt.%) determined by the elemental analysis of the as-thermolyzed Si-C-N ceramic (see Table 6.1). As shown in Fig. 6.3(a), the time period required for the complete degradation of Si_3N_4 decreases with increasing temperature. The reaction times were estimated to be ~ 460 min at 1580°C , ~ 125 min at 1615°C , ~ 31 min at 1650°C , ~ 9 min at 1685°C and ~ 3 min at 1720°C . The same series of measurements were carried out for the Si-B-C-N ceramic samples. However, the complete mass loss has been obtained only for temperatures $T \geq 1650^\circ\text{C}$ and consequently, the entire mass loss of 21.9 ± 0.2 wt.% was determined (see Fig. 6.3(b)). This value of the mass loss is a little less than the nitrogen content of the ceramic (22.5 ± 0.8 wt.%). It is presumably caused by bonding of a small portion of nitrogen with boron due to the formation of BN phase as illustrated by the corresponding phase fraction diagram (Fig. 6.2(b)). The degradation of the Si-B-C-N PDC shows a very slow rate at the temperatures $T = 1580$ and 1615°C (Fig. 6.3(b)). Accordingly, the heat treatment of the sample for 1200 min (20 h) results in the mass loss of 3.6 and 12.9 wt.%, respectively, which corresponds to the progress of the degradation process by $\sim 17\%$ at 1580°C and $\sim 60\%$ at 1615°C within this time period. The complete degradation of Si_3N_4 has been reached after annealing for ~ 540 min at 1650°C , ~ 120 min at 1685°C , and ~ 28 min at 1720°C . Considering the results obtained for both ceramics as shown in Fig. 6.3, the Si-B-C-N ceramic with a boron content of only 1.3 at.% exhibits significantly lower rates for the degradation of Si_3N_4 as compared to the boron-free Si-C-N ceramic at the same temperatures.

6.3.3.2. Structural transformations

To get some more details, XRD analysis was applied to trace the structural transformations within the ceramic samples during course of the degradation process at a single temperature $T = 1650^\circ\text{C}$. For this purpose, the ceramic samples were heated at $T = 1650^\circ\text{C}$ for the specified time periods required for the progress of the Si_3N_4 degradation by 0, 25, 50, 75 and 100%. Using the results of HT-TGA presented in section 6.3.3.1, the corresponding annealing times were estimated to be 0.0, 3.5, 6.2, 10.5 and 31.0 min for the Si-C-N ceramic and respectively 1, 35, 95, 205 and 540 min for the Si-B-C-N ceramic. To avoid the further progress of the Si_3N_4 degradation at the specified degradation fractions, the samples were rapidly cooled (cooling rate $T >$

1100°C: - 250°C/min). The results obtained for $\text{SiC}_{1.4}\text{N}_{0.9}$ are exhibited in Fig. 6.4. The XRD pattern shown in Fig. 6.4(a) reveals the amorphous structure of the Si–C–N ceramic before the initiation of the degradation. After the progress of Si_3N_4 degradation by 25%, the broad peaks corresponding to α/β -SiC were identified (Fig. 6.4(b)). Moreover, the emergence of the small peaks corresponding to α - Si_3N_4 shown in Fig. 6.4(b) indicates the crystallization of Si_3N_4 within the amorphous $\text{SiC}_{1.4}\text{N}_{0.9}$ despite the simultaneous degradation of this phase. As expected, the proceeding of the degradation process by 50 and 75% leads to the enlargement of the SiC peaks (see Fig. 6.4(c) and 6.4(d)). In addition, very weak Si_3N_4 peaks can also be identified. Fig. 6.4(e) indicates the existence of crystalline α/β -SiC after the complete degradation of Si_3N_4 . The XRD measurements displayed in Fig. 6.5 respectively reveal the structural changes of the Si–B–C–N ceramic. Generally, the structural evolution during the degradation process of $\text{SiC}_{1.5}\text{N}_{1.0}\text{B}_{0.05}$ is similar to that observed for $\text{SiC}_{1.4}\text{N}_{0.9}$. It includes the continuous

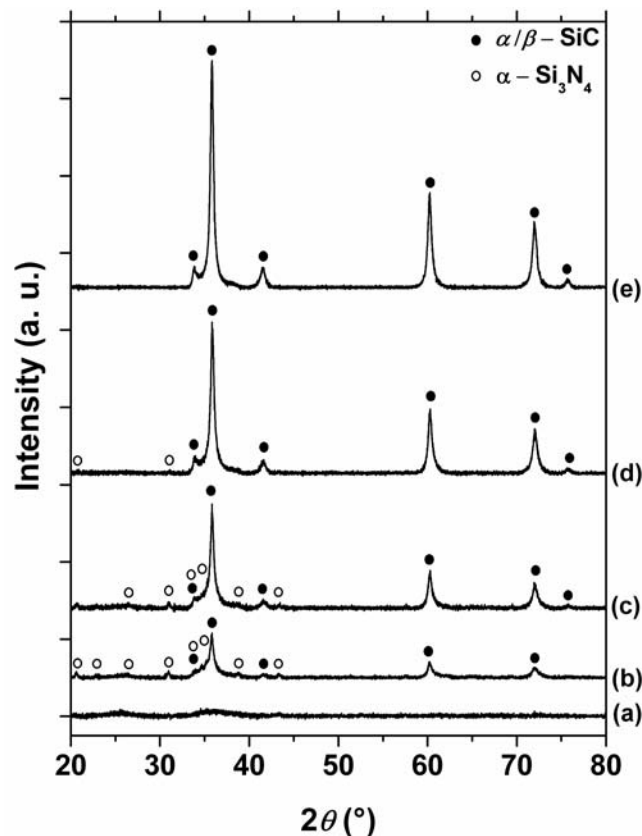


Fig. 6.4. XRD patterns of the Si–C–N ceramic samples annealed at 1650°C for various fractions (%) of the Si_3N_4 degradation: (a) ~ 0% (without dwell time), (b) ~ 25% ($t = 3.5$ min), (c) ~ 50% ($t = 6.2$ min), (d) ~ 75% ($t = 10.5$ min) and (e) ~ 100% ($t = 31.0$ min).

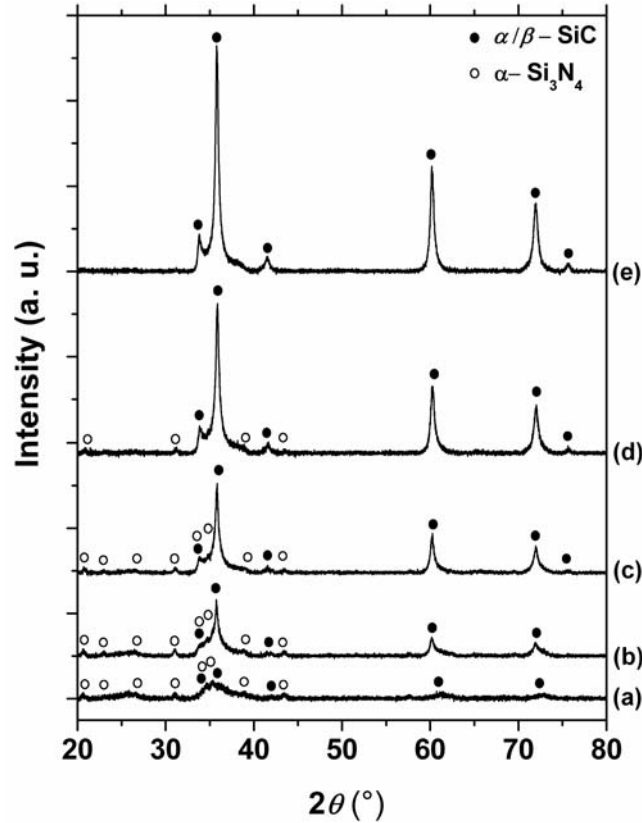


Fig. 6.5. XRD patterns of the Si-B-C-N ceramic samples annealed at 1650°C for various fractions (%) of the Si_3N_4 degradation: (a) $\sim 0\%$ ($t = 1$ min), (b) $\sim 25\%$ ($t = 35$ min), (c) $\sim 50\%$ ($t = 95$ min), (d) $\sim 75\%$ ($t = 205$ min) and (e) $\sim 100\%$ ($t = 540$ min).

increase of SiC crystallites, and also the presence of a small fraction of crystalline Si_3N_4 is observed after the proceeding of the Si_3N_4 degradation by 25% (Fig. 6.5(b)), 50% (Fig. 6.5(c)) and 75% (Fig. 6.5(d)). As expected, the ceramic material contains only α/β -SiC within the crystalline structure after the entire degradation of Si_3N_4 (see Fig. 6.5(e)). However, as shown in Fig. 6.5(a), the crystallization of both phases SiC and Si_3N_4 initiates prior to the start of the Si_3N_4 degradation. This feature is different from the XRD pattern of the Si-C-N ceramic (Fig. 6.4(a)) which shows the existence of the fully amorphous structure before the initiation of the degradation process.

6.3.4. Kinetic analysis of the Si_3N_4 degradation

The kinetic analysis of the HT-TGA curves (Fig. 6.3) was carried out using the JMAK-Erofeev model. This model was initially developed for the kinetic study of phase

transformations [23-27] and subsequently generalized by Erofeev for the kinetic analysis of chemical reactions [28]. Accordingly, the fraction of the degradation process $\alpha(t)$ after a time t at a constant temperature T is given by the following equation:

$$\alpha(t) = \frac{\Delta m(t)}{\Delta m^{\max}} = 1 - \exp(-(kt)^n), \quad (6.4)$$

where $\Delta m(t)$ is the measured mass loss, Δm^{\max} is the maximum value of the mass loss, k is a temperature-dependent rate constant of the degradation process and n is the exponent value which in fact depends on the order of the degradation reaction, the controlling mechanism of the chemical reaction (Eq. (6.1)), the nucleation and growth mechanisms of SiC crystallites (the reaction product) as well as their growth dimensionality (1, 2 or 3). Using the experimental data (see Fig. 6.3), the values $\alpha(t)$ can be estimated. The term $\ln(-\ln(1 - \alpha(t)))$ is plotted versus $\ln(t)$ at five different temperatures for the Si-C-N (Fig. 6.6(a)) and Si-B-C-N (Fig. 6.6(b)) ceramics. Eq. (6.4) can be well fitted with these data yielding the straight lines as shown in Fig. 6.6. The correlation coefficient values > 0.99 point to the excellent consistency between the applied model and the experimental data. The parameters obtained from this kinetic analysis are given in Table 6.2. For the Si-C-N ceramic, the values $n = 1.4, 1.3, 1.4, 1.4$ and 1.5 were calculated for temperatures $1580, 1615, 1650, 1685$ and 1720°C , respectively. For the Si-B-C-N ceramic, correspondingly, the values $n = 0.9, 0.9, 1.0, 0.9$ and 1.0 were determined at the same temperatures. Considering a thermally activated process, the correlation of the rate constant k and temperature T can be described with an Arrhenius equation:

$$k = k_0 \exp\left(-\frac{Q^\circ}{RT}\right), \quad (6.5)$$

where k_0 is a pre-exponent parameter, Q° represents the effective activation energy of the process and R is the gas constant. Fig. 6.7 exhibits a plot of the term $\ln k(T)$ versus the reverse temperature $1/T$ for the both ceramics based on the data given in Table 6.2.

Using Eq. (6.5), the straight lines with different slopes are well fitted for $\text{SiC}_{1.4}\text{N}_{0.9}$ and $\text{SiC}_{1.5}\text{N}_{1.0}\text{B}_{0.05}$ as seen in Fig. 6.7. Accordingly, the value $Q^\circ = 11.6 \pm 0.5 \text{ eV}$ was obtained as the effective activation energy of the Si_3N_4 degradation for the Si-C-N ceramic, and significantly larger value $Q^\circ = 17.1 \pm 0.7 \text{ eV}$ was estimated for the Si-B-C-N ceramic.

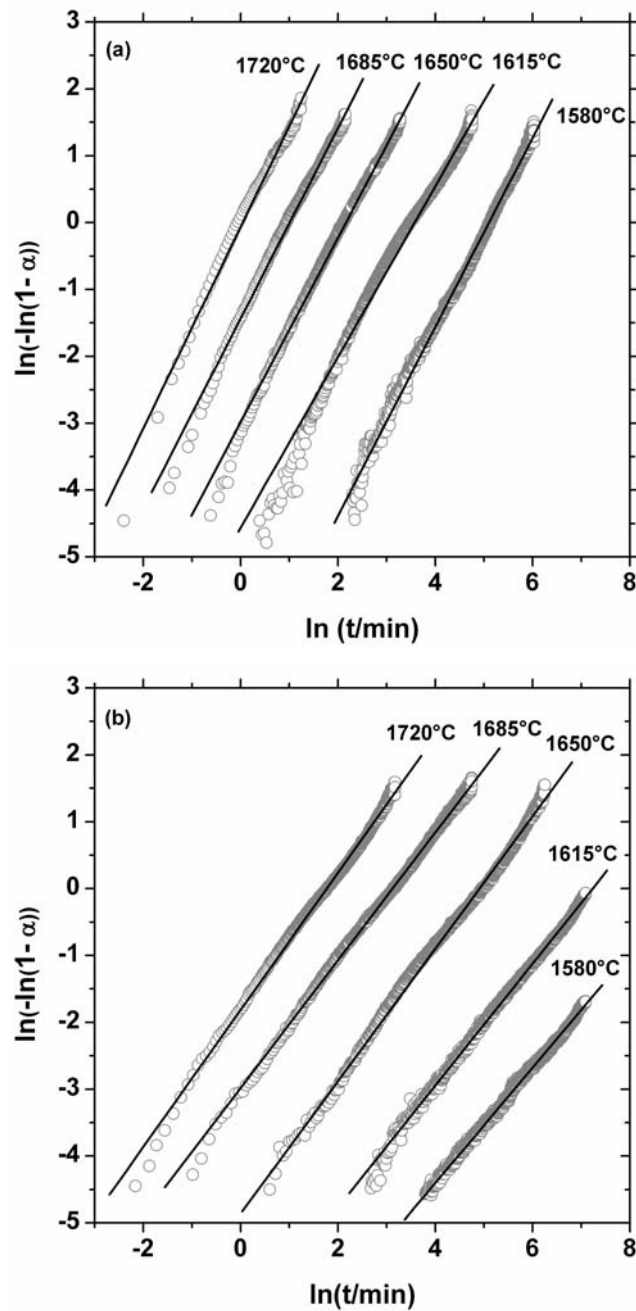


Fig. 6.6. Plot of the term $\ln(-\ln(1-\alpha(t)))$ versus $\ln(t)$ at various temperatures for the Si-C-N (a) and Si-B-C-N (b) ceramics. Solid straight lines correspond to a linear fit of the data according to Eq. (6.4).

Table 6.2. Rate constants k , exponent values n and correlation coefficients obtained by fit of the data shown in Fig. 6.6 by Eq. (6.4) at various temperatures for the Si–C–N and Si–B–C–N ceramics.

Temperature (°C)	Si–C–N			Si–B–C–N		
	n^a	k (s ⁻¹) ^b	Correlation coefficient	n^a	k (s ⁻¹) ^b	Correlation coefficient
1580	1.4	1.0×10^{-4}	0.999	0.9	1.8×10^{-6}	0.998
1615	1.3	4.5×10^{-4}	0.994	0.9	1.2×10^{-5}	0.999
1650	1.4	1.8×10^{-3}	0.998	1.0	1.2×10^{-4}	0.997
1685	1.4	6.2×10^{-3}	0.997	0.9	7.2×10^{-4}	0.999
1720	1.5	1.6×10^{-2}	0.994	1.0	2.8×10^{-3}	0.998

^a The error values are in the range ± 0.02 and negligible.

^b The error values are very small and negligible (e.g. $\pm 2.0 \times 10^{-4}$ s⁻¹ at $T = 1720^\circ\text{C}$ for the Si–C–N ceramic and $\pm 2.0 \times 10^{-8}$ s⁻¹ at $T = 1580^\circ\text{C}$ for the Si–B–C–N one).

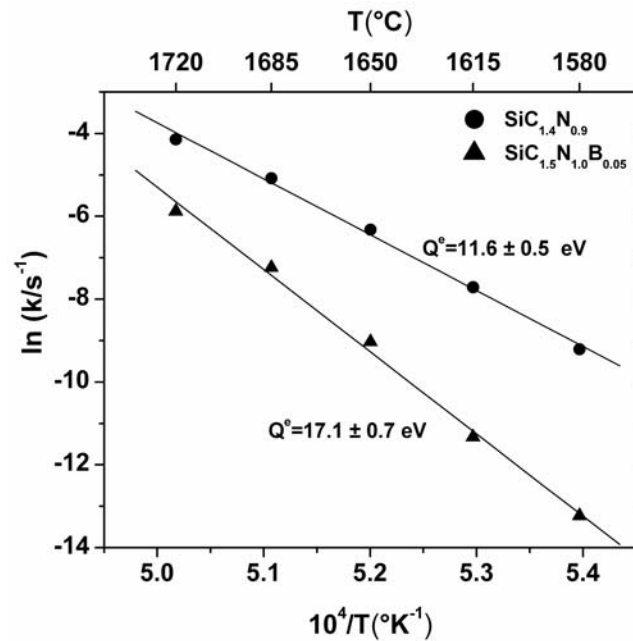


Fig. 6.7. Plot of the term $\ln(k)$ versus reversible temperature for the Si–C–N and Si–B–C–N ceramics. Solid straight lines represent a linear fit of the data according to Eq. (6.5).

6.4. Discussion

All the observations presented above prove that for the both ceramics ($\text{SiC}_{1.4}\text{N}_{0.9}$ and $\text{SiC}_{1.5}\text{N}_{1.0}\text{B}_{0.05}$), the investigated degradation process is due to the carbothermal reduction of Si_3N_4 (Eq. (6.1)). In the following, a detailed description of this reaction will be given.

Taking into account the amorphous structure of the as-thermolyzed ceramics (see Fig. 6.1), the degradation of Si_3N_4 (Eq. (6.1)) can be considered through two possible ways: (a) the reaction of amorphous Si_3N_4 with carbon, (b) the crystallization of Si_3N_4 and its subsequent reaction with carbon. As demonstrated by the XRD analysis (see Fig. 6.4 and 6.5), the crystallization of Si_3N_4 occurs for $\text{SiC}_{1.5}\text{N}_{1.0}\text{B}_{0.05}$ and $\text{SiC}_{1.4}\text{N}_{0.9}$ prior and during the degradation course, respectively. Recent quantitative XRD analyses have shown that the crystallization of Si_3N_4 in the amorphous Si-(B)-C-N PDCs advances continuously with time [29-33]. However, considering the XRD peaks corresponding to α - Si_3N_4 (see Fig. 6.4 and 6.5), the fraction of crystalline Si_3N_4 at the beginning of the degradation process does not noticeably grow with increasing time and starts to diminish while the degradation proceeds. The most probable reason for this observation is the reaction of crystalline Si_3N_4 with carbon. In other words, the degradation process follows the crystallization of Si_3N_4 and indeed, Si_3N_4 crystallites are consumed by the reaction with carbon. In spite of that, the findings in the present work do not yield any evidence to deny the reaction of amorphous Si_3N_4 and carbon. Hence, the degradation process is supposed to proceed generally by the reaction of crystalline Si_3N_4 and carbon; however, the simultaneous reaction of carbon with amorphous Si_3N_4 is also plausible.

In principle, the progress of the Si_3N_4 carbothermal reduction (Eq. (6.1)) including solid reactants (Si_3N_4 and C) and solid / gas products (SiC and N_2) can be considered as a four-stage process: (a) diffusion of the reactant elements, (b) chemical reaction at interfaces of the reactants, (c) nucleation and growth of SiC as the solid product and (d) Gas (N_2) outflow from the system. Obviously, each stage individually possesses a progress rate. In general, the stage with the slowest rate determines the reaction kinetics and represents the controlling mechanism of the reaction. When the rates of two or more steps are comparable, a mixed mechanism controls the development of the reaction. The kinetic analysis of the Si_3N_4 degradation expressed in section 6.3.4 suggests two distinct values for the parameter $n \approx 1.4$ and $n \approx 0.94$ in the investigated ceramics $\text{SiC}_{1.4}\text{N}_{0.9}$ and

$\text{SiC}_{1.5}\text{N}_{1.0}\text{B}_{0.05}$, respectively. In principle, the value n can be considered as an indication for the controlling mechanism of chemical reactions. Therefore, these different values of n obtained for the degradation kinetics of Si_3N_4 suggests the domination of a mechanism for this reaction in $\text{SiC}_{1.4}\text{N}_{0.9}$ different from the one valid for $\text{SiC}_{1.5}\text{N}_{1.0}\text{B}_{0.05}$. Moreover, the different values $Q^\circ = 11.6 \pm 0.5 \text{ eV}$ and $Q^\circ = 17.1 \pm 0.7 \text{ eV}$ estimated for the effective activation energies of the degradation process for the Si–C–N and Si–B–C–N ceramics, respectively, evidently reveal the kinetic impact of boron on the thermal stability.

Recently, the kinetics of the SiC formation as the product of the reaction between Si_3N_4 and C was studied by quantitative XRD measurements for two Si–C–N PDCs and consequently, the effective activation energy of the crystallization was calculated to be 12.5 and 13 eV [32,33]. These values are almost consistent with the value $Q^\circ = 11.6 \pm 0.5 \text{ eV}$ determined in the present study for the Si–C–N ceramic. Accordingly, the crystallization of SiC (stage (c)) can be deduced as the controlling step for the progress of the Si_3N_4 carbothermal reduction. Considering the dominant controlling by the crystallization of SiC and regarding the description used for the phase transformation kinetics [34], the obtained value $n \approx 1.4$ signifies a three-dimensional diffusion controlled growth of the pre-existing nucleus as the dominant mechanisms of the SiC crystallization. In this connection, the SEM micrographs taken from a surface and a fractured section of the samples after the complete degradation of the Si–C–N ceramic (Fig. 6.8(a) and 6.8(b)) do not exhibit any sign of one- or two-dimensional growth for SiC crystallites despite the huge difference of the dimensions between the crystallites grown on the surface ($\langle d \rangle \approx 0.2 - 1 \mu\text{m}$) and those grown within the bulk ($\langle d \rangle \leq 50 \text{ nm}$). In addition to the plausible dominant mechanism of the Si_3N_4 degradation deduced above for the Si–C–N ceramic, the values $n > 1$ can indicate the occurrence of a chemically controlled reaction according to the literature [35-39]. Therefore, the chemical reaction at interfaces between Si_3N_4 and C (stage (b)) and the formation of SiC crystallites as the reaction product (stage (c)) are two most plausible processes which one or both of them can control the kinetics of the degradation process for the investigated Si–C–N ceramic.

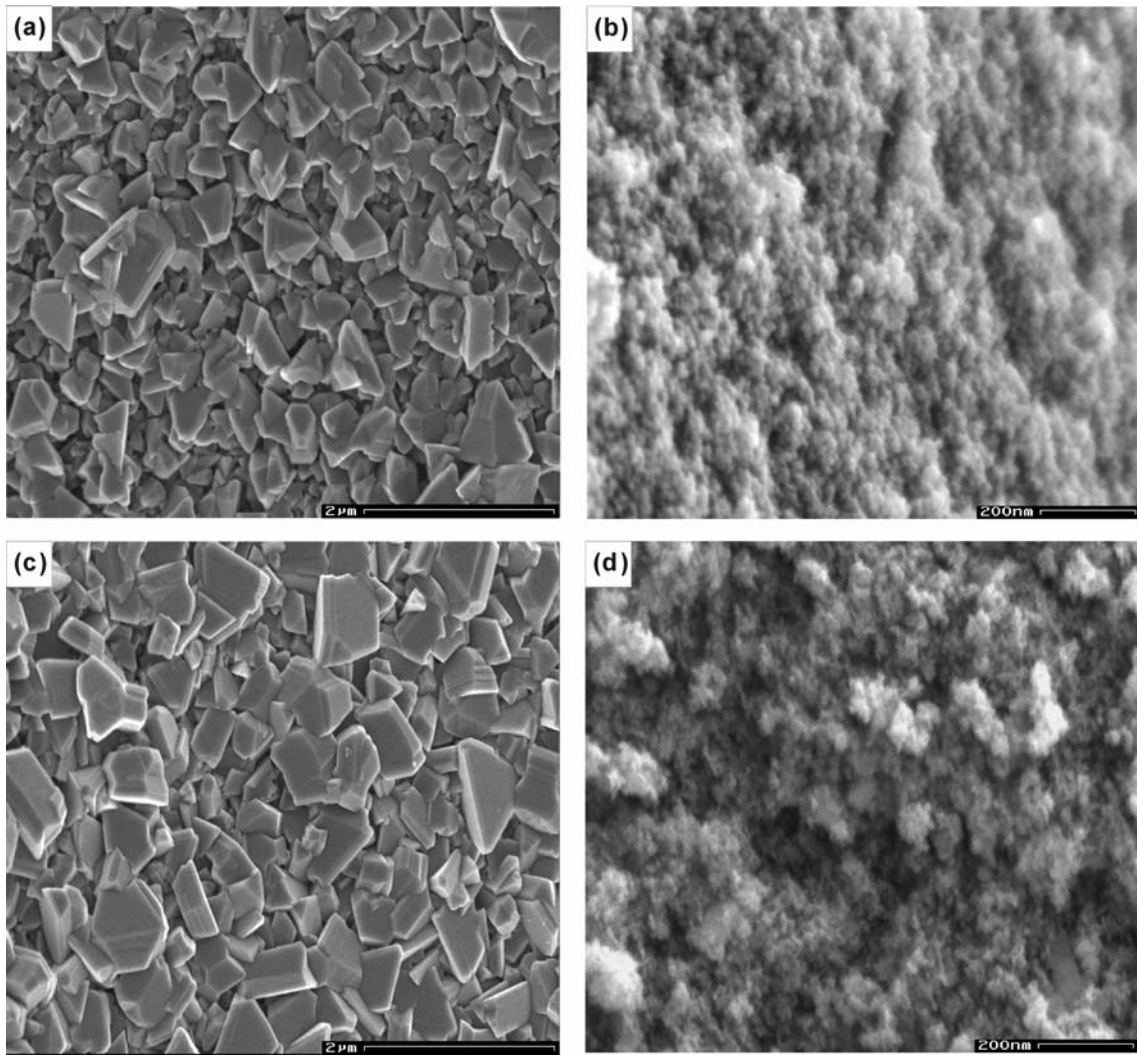


Fig. 6.8. SEM images of the ceramics after the accomplishment of the degradation process at $T = 1650^{\circ}\text{C}$. The images (a) and (c) exhibit SiC crystallites grown on surfaces of the as-obtained particles from the Si-C-N and Si-B-C-N ceramics, respectively. The images (b) and (d) were taken through the bulk using fractured surfaces of the as-obtained particles from the Si-C-N and Si-B-C-N ceramics, respectively.

Assuming the SiC crystallization (stage (c)) as the controlling stage of the Si_3N_4 degradation for the Si-B-C-N ceramic, $n \approx 0.94$ obtained from the kinetic investigations implies a one- or two-dimensional growth of the crystallites according to Ref. [34]. However, the SEM images taken from a surface and a fractured section of the ceramic particles (Fig. 6.8(c) and 6.9(d)) exhibit a three-dimensional growth of SiC crystallites comparable to the crystallite morphology shown for the Si-C-N ceramic in Fig. 6.8(a) and 6.8(b). Therefore, the Si_3N_4 degradation process for the Si-B-C-N

ceramic is less likely to be controlled by the kinetics of the SiC crystallization. On the other hand, the values $n < 1$ can be interpreted as evidence which points to a reaction controlled by the diffusion process (stage (a)) [35-39]. Therefore, the degradation rates determined for the Si-B-C-N ceramics substantially slower than those obtained for the Si-C-N ones at the same temperatures (Table 6.2) can be ascribed to a significant slowdown of the diffusion process in the Si-B-C-N ceramic. This deduction indeed concedes a proposed model in which the hindering effect of boron on the Si₃N₄ degradation in Si-B-C-N PDCs was supposed to be owing to the existence of BNC_x turbostratic layers as a diffusion barrier [9]. Using this approach, the value $Q^e = 17.1 \pm 0.7$ eV corresponding to the effective activation energy of the degradation process for the Si-B-C-N ceramic can be attributed to the activation enthalpy for the diffusion of one or all of the contributing elements (Si, N and C). In this connection, the recent studies on the self diffusion of Si and N into the amorphous Si-B-C-N PDCs using tracer isotopes yield the values for the activation energy of diffusion Q^D in the range between 5.5-7.2 eV [39-42] which are strikingly smaller than the value $Q^e \approx 17$ eV suggested above to be considered the diffusion barrier. Consequently, it is more accurate to attribute the obtained value of the activation energy to the activation enthalpy for the diffusion of carbon out of BNC_x turbostratic layers. The deriving energy for this phenomenon is the decrease of the system's free energy through the reaction of carbon with Si₃N₄ at the BNC_x / Si₃N₄ interface. It is worth noting that $Q^D = 4.2$ eV reported in Ref. [43] for the diffusion of a implanted radioisotope ¹¹C within one Si-B-C-N PDC can not account as the diffusion enthalpy of the element C out of BNC_x turbostratic layers due to the fact that the chemical and structural environment of a implanted carbon or even a tracer carbon within the ceramic is essentially dissimilar to that of carbon within BNC_x turbostratic layers. In addition to the governing mechanism suggested above, a limiting role of BNC_x layers in the rate of the gas (N₂) discharge from the reaction environment can also be a reason for the slow kinetics of the Si₃N₄ degradation in the Si-B-C-N ceramic. Hence, the diffusion of carbon outside of the BNC_x structure (stage (a)) and the gas outflow (stage (d)) are most probable steps which one or both of them can act as a controlling stage of the Si₃N₄ degradation for the Si-B-C-N ceramic.

6.5. Summary and conclusions

In this study, the isothermal mass loss of two polymer-derived ceramics with compositions $\text{SiC}_{1.4}\text{N}_{0.9}$ and $\text{SiC}_{1.5}\text{N}_{1.0}\text{B}_{0.05}$ was investigated using high temperature thermal gravimetric analysis for various temperatures ranging from 1580 to 1720°C in order to analyze the influence of boron on the kinetics of the reaction between Si_3N_4 and C (Si_3N_4 degradation). Furthermore, the structural changes of the ceramics during the degradation course were studied by XRD measurements. Accordingly, the following results were obtained:

- The Si-B-C-N ceramic shows remarkably longer time period for the Si_3N_4 degradation as compared to the Si-C-N ceramic at the same temperatures.
- The structural analysis indicates the continuous formation of SiC crystallites as the product of the reaction between Si_3N_4 and C with increasing time. Moreover, the existence of crystalline Si_3N_4 was observed before and during the degradation course for the Si-B-C-N and Si-C-N ceramics, respectively.
- As the outcome of the kinetic analysis, the exponent values n were obtained in the range between 1.3-1.5 and 0.9-1.0 for the Si-C-N and Si-B-C-N ceramics, respectively. Moreover, $Q^\circ = 17.1 \pm 0.7$ eV was obtained as the effective activation energy of the Si_3N_4 degradation for the Si-B-C-N ceramic. This value is significantly larger than $Q^\circ = 11.6 \pm 0.5$ eV attained for the Si-C-N ceramic.

The interpretation of the structural analysis leads to this conclusion that the degradation process mainly occurs by the reaction of crystalline Si_3N_4 and carbon for both ceramics. Nevertheless, the reaction of amorphous Si_3N_4 and carbon is also likely. Based on the interpretation of the kinetic data in the case of the Si-C-N ceramic, the chemical reaction at the interface of the reactants and the formation kinetics of SiC as the reaction product are two potential processes which individually or together conduct the progress of the Si_3N_4 degradation. However, two other mechanisms are suggested for the control of the Si_3N_4 degradation kinetics in the Si-B-C-N ceramic: (a) the local diffusion of free carbon outside of BNC_x turbostratic layers, (b) flow of the reaction gas product (N_2) out of the reaction area. Depending on the rate of these processes, one or both of them limits the development of the reaction between Si_3N_4 and carbon.

It should be taken into account that this work only addressed the kinetic impact of boron on the thermal stability of Si-(B)-C-N PDCs and any possible thermodynamic effect of boron on the reaction between Si_3N_4 and carbon is still a matter of debate.

Acknowledgements

The authors would like to thank Peter Gerstel for synthesis of the polymer precursors, Gerhard Kaiser for elemental analysis of the Ceramic materials and Felicitas Predel for her contribution in the SEM analysis. Financial supports by the European Community's Sixth Framework Program through a Marie Curie Research Training Network and International Max Planck Research School for Advanced Materials are highly appreciated.

References

- [1] D. Mocaer, R. Pailler, R. Naslain, C. Richard, J.P. Pillot, J. Dunogues, C. Gerardin, F. Taulelle, *J. Mater. Sci.* 28 (1993) 2615.
- [2] J. Bill, F. Aldinger, *Adv. Mater.* 7 (1995) 9.
- [3] M. Monthieux, O. Delverdier, *J. Eur. Ceram. Soc.* 16 (1996) 721.
- [4] H.J. Kleebe, D. Suttor, H. Müller, G. Ziegler, *J. Am. Ceram. Soc.* 81 (1998) 2971.
- [5] R. Riedel, H.J. Kleebe, H. Schönfelder, F. Aldinger, *Nature* 374 (1995) 526.
- [6] R. Riedel, W. Dressler, *Ceram. Int.* 22 (1996) 233.
- [7] R. Riedel, L.M. Ruswisch, L. An, R. Raj, *J. Am. Ceram. Soc.* 81 (1998) 3341.
- [8] G. Thurn, J. Canel, J. Bill, F. Aldinger, *J. Eur. Ceram. Soc.* 19 (1999) 2317.
- [9] H.J. Seifert, H.L. Lukas, F. Aldinger, *Ber. Bunsenges. Phys. Chem.* 102 (1998) 1309.
- [10] H.J. Seifert, J. Peng, J. Golczewski, F. Aldinger, *Appl. Organometal. Chem.* 15 (2001) 794.
- [11] H.P. Baldus, M. Jansen, O. Wagner, *Key Eng. Mater.* 89-91 (1994) 75.
- [12] R. Riedel, A. Kienzle, W. Dressler, L. Ruwisch, J. Bill, F. Aldinger, *Nature* 382 (1996) 796.
- [13] A. Müller, P. Gerstel, M. Weinmann, J. Bill, F. Aldinger, *J. Eur. Ceram. Soc.* 20 (2000) 2655.

- [14] A. Müller, P. Gerstel, M. Weinmann, J. Bill, F. Aldinger, *J. Eur. Ceram. Soc.* 21 (2001) 2171.
- [15] J. Haug, P. Lamparter, M. Weinmann, F. Aldinger, *Chem. Mater.* 16 (2004) 83.
- [16] A. Jalowiecki, J. Bill, F. Aldinger, *Composites Part A* 27 (1996) 717.
- [17] A. Müller, A. Zern, P. Gerstel, J. Bill, F. Aldinger, *J. Eur. Ceram. Soc.* 22 (2002) 1631.
- [18] J. Schumacher, F. Berger, M. Weinmann, J. Bill, F. Aldinger, K. Müller, *Appl. Organometal. Chem.* 15 (2001) 809.
- [19] F. Berger, A. Müller, F. Aldinger, K. Müller, *Z. Anorg. Allg. Chem.* 631 (2005) 355.
- [20] M. Weinmann, J. Schuhmacher, H. Kummer, S. Prinz, J. Peng, H. J. Seifert, M. Christ, K. Müller, J. Bill, F. Aldinger, *Chem. Mater.* 12 (2000) 623.
- [21] M. Peuckert, T. Vaahs, M. Brück, *Adv. Mater.* 2 (1990) 398.
- [22] B. Sundman, B. Jansson, J.O. Anderson, *CALPHAD* 6 (1985) 153.
- [23] M. Avrami, *J. Chem. Phys.* 7 (1939) 416.
- [24] M. Avrami, *J. Chem. Phys.* 8 (1940) 212.
- [25] M. Avrami, *J. Chem. Phys.* 9 (1941) 177.
- [26] W.A. Johnson, R. Mehl, *Trans. AIME* 135 (1939) 416.
- [27] A.N. Kolmogorov, *Isz. Akad. Nauk SSR, Ser. Fiz.* 3 (1937) 355.
- [28] B.V. Erofeev, *C.R. Acad. Sci. USSR* 52 (1946) 511.
- [29] A.H. Tavakoli, P. Gerstel, J.A. Golczewski, J. Bill, *J. Non-Cryst. Solids* 355 (2009) 2381.
- [30] A.H. Tavakoli, P. Gerstel, J.A. Golczewski, J. Bill, *J. Am. Ceram. Soc.* 93 (2010) 1470.
- [31] A.H. Tavakoli, P. Gerstel, J.A. Golczewski, J. Bill, *J. Mater. Res.*, in press (DOI:10.1557/JMR.2010.0282).
- [32] H. Schmidt, G. Borchardt, A. Müller, J. Bill, *J. Non-Cryst. Solids* 341 (2004) 133.
- [33] H. Schmidt, G. Borchardt, *Adv. Eng. Mater.* 7 (2005) 221.
- [34] J.W. Christian, *The Theory of Transformations in Metals and Alloys*, Pergamon, Oxford, 2002.
- [35] A.K. Baev, V.Y. Mishin, I.L. Gaidym, M.E. Rubtzov, *Radiokhimiya* 3 (1979) 383.
- [36] K.I. Patrilyak, V.G. Motorni, *Zh. Fiz. Khim.* 56 (1982) 582.

-
- [37] A.K. Baev, Y.L. Gubar, K.S. Gasanov, *Zh. Fiz. Khim.* 56 (1982) 2432.
- [38] L.T. Vlaev, G.G. Gospodinov, S.D. Genieva, *Thermochimica Acta* 417 (2004) 13.
- [39] H. Schmidt, G. Borchardt, S. Weber, S. Scherrer, H. Baurmann, A. Müller, J. Bill, *J. Appl. Phys.* 88 (2000) 1827.
- [40] H. Schmidt, G. Borchardt, H. Baurmann, S. Weber, S. Scherrer, , A. Müller, J. Bill, *Def. and Diff. For.* 194-199 (2001) 941.
- [41] H. Schmidt, *Diff. Fundamentals* 2 (2005) 59.1.
- [42] H. Schmidt, G. Borchardt, O. Kaïtasov, B. Lesage, *J. Non-Cryst. Solids* 353 (2007) 4801.
- [43] T. Voss, A. Strohm, W. Frank, *Int. J. Mater. Res. (Z. Metallkd.)* 94 (2003) 419.

Summary

7.1. Introduction

The term "Thermal Stability" is used for polymer-derived ceramics (PDCs) to describe the temperature range of stability against the crystallization and chemical degradation of these amorphous materials. Si-(B-)C-N PDCs reveal an attractive capability of high temperature stability ranging up to 2000 °C. The thermal stability can drastically change with the chemical composition. For instance, the incorporation of boron within the Si-C-N PDCs leads to a substantial increase. The high temperature stability of these ceramics also depends on structural transformations due to phase separations in consequence of annealing. Thus, the understanding of this separation process is essential for developing PDCs with outstanding thermal stability. According to the quantitative description of the phase separation, an amorphous ceramic with a composition SiC_aN_b located within the three-phase region C-SiC-Si₃N₄ separates into a fraction of amorphous carbon balanced by a composition SiC_xN_b of the amorphous domains located along the line SiC-Si₃N₄ as shown in Fig. 7.1. Correspondingly, the Si-B-C-N amorphous ceramic with a composition of $\text{SiC}_a\text{N}_b\text{B}_c$ located within the four-phase region SiC-Si₃N₄-BN-C is separated into the amorphous domains $(\text{BN})_c\text{C}_y$ and $\text{SiC}_{a-y}\text{N}_{b-c}$. Their compositions are located along the C-BN and SiC-Si₃N₄ lines, respectively (see Fig. 7.1). In fact, the phase separation present in the microstructure of amorphous Si-(B-)C-N PDCs appears as a generic feature tightly connected with the content of the separated components, and boron is the key element in this connection. As explained above, the predominant features are separated amorphous Si-C-N domains. These domains consist of $\text{SiC}_i\text{N}_{4-i}$ ($i = 0 - 4$) tetrahedral structural units as suggested by means of NMR and scattering experiments. Such ternary atomic configurations cannot be obtained in crystalline Si-C-N ceramics

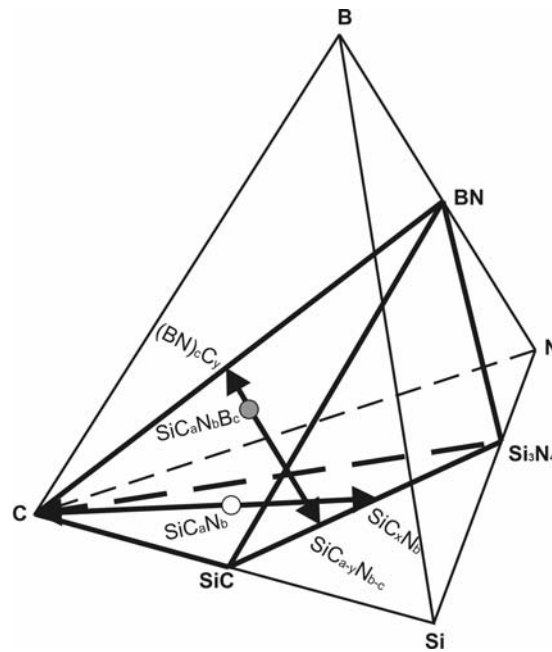


Fig. 7.1. Schematic illustration of the phase separations corresponding to amorphous SiC_aN_b and $\text{SiC}_a\text{N}_b\text{B}_c$ PDCs.

through conventional high-temperature sintering of ceramic powders. They are the essence of the polymer precursor route and result from covalent bonds, which are already pre-existing in the polymers or are formed during thermolysis. The Si–B–C–N PDCs indicate a particular crystallization behavior including the formation of SiC nanocrystallites at much lower temperature than that of Si_3N_4 nanocrystallites. The tetrahedral structural units which constitute the amorphous Si–C–N domains, as noted above, affect extraordinary resistance against crystallization. For the simple reason that $\text{SiC}_i\text{N}_{4-i}$ mixed tetrahedra cannot be incorporated in crystalline structures of neither silicon nitride nor silicon carbide, their full decomposition is a necessary precondition for complete crystallization of these materials. Despite the reported attempts aimed at a better understanding of the thermal stability in Si–(B–)C–N PDCs, fundamental investigations with focus on the thermodynamic and kinetic aspects of the structural transformations in these materials are lacking.

In this Ph.D. thesis, thermodynamics and kinetics of the crystallization of amorphous Si–(B–)C–N PDCs as well as the degradation of these materials by the carbothermal reaction ($\text{Si}_3\text{N}_4 + 3\text{C} \rightarrow 3\text{SiC} + 2\text{N}_2\uparrow$) were comprehensively studied for the first time. The focus is on the influence of the boron content on the structural evolution within these materials. The obtained results are presented in 5 chapters

(chapters 2 to 6). Chapters 2 to 5 are associated with the thermodynamic and kinetic aspects of the crystallization process and chapter 6 corresponds to the kinetic impact of boron on the degradation process.

7.2. Thermodynamic calculations

Thermodynamic calculations for Si-(B)-C-N PDCs were computed using the Thermo-Calc software in order to estimate the equilibrium phases together with the temperature range of their stability, the thermodynamic impact of boron on the driving energy of the crystallization and the sequence of crystallite formation within the amorphous state. These computations contain the phase fraction diagrams based on the stable phase equilibria (chapters 2, 3 and 6), Gibbs energies of the amorphous states (chapters 2 and 3), driving energies for the crystallization (chapter 2) and modeling of the metastable phase equilibria* (chapter 3).

7.3. Experimental procedures

In order to carry out the experimental investigations, a polysilazane which leads to the ceramic with the composition $\text{SiC}_{1.4}\text{N}_{0.9}$ was used as a base material. Within this polymer, different amounts of boron were introduced in order to provide materials with a constant atomic Si/C/N ratio and various boron contents. Accordingly, Si-B-C-N ceramics with boron contents of 1.3, 3.7, 6.0 and 8.3 at.% B were obtained by thermolysis of the corresponding polymer precursors at 1100°C for 4 h under argon atmosphere. The thermodynamic computation of stable phase equilibria reveals that the compositions of the boron-free and boron-containing ceramics are located within the limits of the three-phase region C-SiC-Si₃N₄ and the four-phase region SiC-Si₃N₄-BN-C of the ternary Si-C-N and the quaternary Si-B-C-N system, respectively. Moreover, X-ray diffraction (XRD) measurements reveal an amorphous character of the as-obtained ceramics.

* This model is based on a new approach including a thermodynamic description of nanocrystalline SiC and Si₃N₄ dependant on dimensions. In the applied model, the Gibbs energy of a nanocrystalline phase is derived introducing an excess energy term $\Delta G^{\text{ex}} = A/\langle d \rangle$, where A is a maximum value of the excess energy corresponding to the minimum average nanocrystallite dimensions and $\langle d \rangle$ is an average crystallite size changing with temperature at a constant heating rate.

The major part of the experimental investigations is dedicated to XRD measurements of the heat treated samples in order to analyze the volume fraction of the crystallized phases growing within the amorphous PDCs during the crystallization course as a function of annealing time and temperature (chapters 3 to 5). In addition to the XRD measurements, further experimental investigations were carried out using high temperature thermal gravimetric analysis (HT-TGA), transmission electron microscopy (TEM), energy-filtering TEM (EFTEM) and field-emission scanning electron microscopy (SEM). For the chemical analysis of the samples, inductively coupled plasma-atomic emission spectroscopy together with a combination of various analysis equipment based on the combustion techniques were applied.

7.4. Results and discussion

In chapter 2, the crystallization behavior of four amorphous PDCs containing 0, 3.7, 6.0 and 8.3 at.% B is described. Thermodynamic modeling of the amorphous Si-C-N domains proves that the addition of boron increases the driving energy of the crystallization. The experimental results of this study demonstrate that the increase of the boron content promotes the formation of the nanocrystallites (SiC) in accordance with the thermodynamic computations. The XRD patterns of the heat treated samples for the boron-containing ceramics exhibit that SiC nanocrystallites form at lower temperatures ($1300 \leq T \leq 1400^\circ\text{C}$) after a considerably short annealing time ($t < 2$ h) as compared to Si_3N_4 nanocrystallites which emerge at significantly higher temperature ($T = 1650^\circ$) after heat treatment for 16 - 32 h, depending on the boron content*. On the contrary, the crystallization of Si_3N_4 and SiC in the amorphous boron-free material is detected after annealing at $T = 1400^\circ\text{C}$ for 2 h. A further result of this study corresponds to the role of boron on the fraction of α and β modifications of Si_3N_4 in the boron-containing ceramics. The ratio α / β is reduced with increasing the boron content.

Chapter 3 is associated with the isochronal crystallization behavior of the amorphous ceramic including 8.3 at.% B at various heating rates (1, 5 and $25^\circ\text{C}/\text{min}$) using quantitative analysis of the XRD patterns and the model of metastable phase equilibria. It is demonstrated that the crystallization process according to the

* It is already known that the crystallization of Si_3N_4 is significantly retarded with increasing the boron content up to ~ 10 at. %.

experimental analysis is to a large extent in agreement with the formation sequence of the nanocrystalline phases within the amorphous state anticipated by the model of metastable phase equilibria. According to the experimental investigations, the crystallization of SiC is initiated at temperatures above 1300°C. This stage of crystallization is followed by the second stage of crystallization including the formation of Si₃N₄ nanocrystallites in addition to the evolution of further SiC nanocrystallites. Depending on the heating rate, this second period of crystallization occurs at temperatures in the range between 1800 and 1900°C. The two-stage crystallization behavior for the Si–B–C–N ceramic isochronally annealed with the heating rate of 25°C/min is illustrated in Fig. 7.2. Metastable phase fraction diagrams as the outcome of the modeling demonstrate a two-stage crystallization process. As exemplarily shown in Fig. 7.3, the formation of nanocrystalline SiC at the first stage is followed by the eutectoid-like transformation of the remaining Si-containing amorphous state to the nanocrystalline phases Si₃N₄ and SiC.

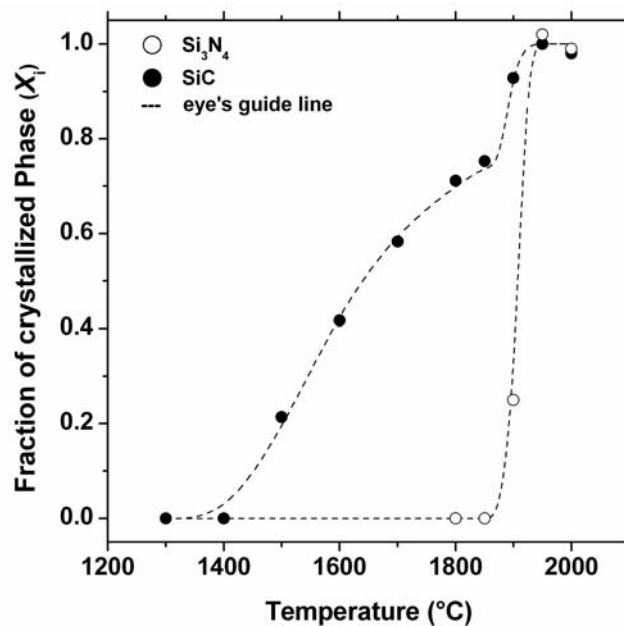


Fig. 7.2. Volume fraction of the crystallized phases SiC and Si₃N₄ versus temperature determined by quantitative XRD analysis after isochronal annealing of the Si–B–C–N (8.3 at.% B) ceramic with a heating rate of 25°C/min. A typical error value is estimated to be ± 0.05.

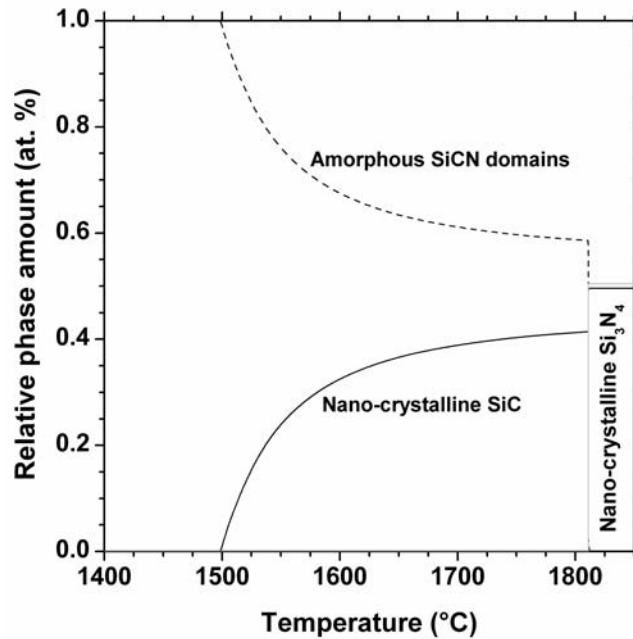


Fig. 7.3. Metastable phase fraction diagram including amorphous Si-C-N domains together with the nanocrystalline phases SiC and Si₃N₄ computed by the Thermo-Calc software for the Si-B-C-N (8.3 at.% B) ceramic using a heating rate of 25°C/min.

In chapters 4 and 5, a comprehensive kinetic analysis* of the Si₃N₄ crystallization in Si-B-C-N PDCs is provided. Using the ceramics with various boron contents gives a further opportunity to figure out the kinetic impact of boron on the Si₃N₄ crystallization. The growing volume fraction of the crystallized Si₃N₄ in the isothermally annealed samples was determined using quantitative XRD analysis. As a result, the continuous nucleation of the crystallites was identified as the dominant mechanism of the nucleus formation followed by a three-dimensional growth process, which is controlled by the volume diffusion of the elements Si and N in the amorphous state. Moreover, the obtained results imply that the determined crystallization mechanisms are independent on the boron content. However, the significant role of boron on the activation energy of the Si₃N₄ crystallization was revealed. The corresponding values for the activation energies were determined to be 7.8, 9.0 and 11.5 eV for the ceramics including 3.7, 6.0 and 8.3 at.% B, respectively (Fig. 7.4). Furthermore, the obtained results indicate that

* The kinetic analysis was performed by the classical theory for the investigation of isothermal phase transformation kinetics developed by Johnson, Mehl, Avrami and Kolmogorov (JMAK-theory).

the crystallization process for the α and β modifications of Si_3N_4 follows almost the same kinetic behavior. Further analyses indicate that the values corresponding to the activation energies for the process of nucleation are much larger than the anticipated values attributed to the activation energies of the growth process. This finding points to the crucial role of the nucleation kinetics in the progress of the crystallization course and also demonstrates the significant increase of the energy barrier for the nucleation process with increasing the boron content.

In chapter 6, the kinetic effect of boron on the chemical stability of the Si-(B)-C-N PDCs is discussed. The chemical instability of these materials corresponds to the carbothermal reduction of Si_3N_4 (Si_3N_4 degradation) according to the reaction $\text{Si}_3\text{N}_4 + 3\text{C} \rightarrow 3\text{SiC} + 2\text{N}_2\uparrow$ which results in a mass loss of the ceramics. Therefore, the isothermal mass loss of the boron-free ceramic and the ceramic containing 1.3 at.% B was measured as a function of time using thermal gravimetric analysis at various

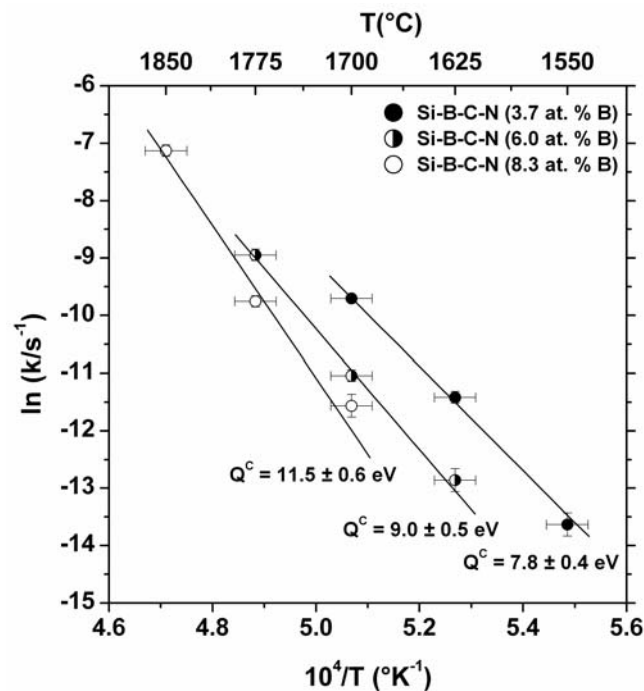


Fig. 7.4. Plot of the term $\ln(k)$, natural logarithm of the crystallization rate constant, versus the reversible temperature for the Si-B-C-N ceramics including the various boron contents. Solid straight lines are associated with a linear fit of the data. The slope of the fitted lines is proportional to the value of the activation energy for crystallization Q^c .

temperatures. The results of the kinetic analysis* prove that the effective activation energy and the controlling mechanisms of the Si_3N_4 degradation are strongly influenced by the presence of boron. In this connection, the values of activation energies for the degradation process were estimated to be 11.6 ± 0.5 and 17.1 ± 0.7 eV for the Si–C–N and Si–B–C–N ceramic, respectively, as shown in Fig. 7.5. Based on the obtained kinetic parameters, the chemical reaction at the interface of the reactants (Si_3N_4 and C) and the formation kinetics of SiC as the reaction product are two potential processes which individually or together conduct the progress of the Si_3N_4 degradation for the boron-free ceramic. In the case of the boron-containing ceramic, the local diffusion of C out of BNC_x turbostratic layers, surrounding the Si_3N_4 nanocrystals, and the gas (N_2) outflow from the reaction zone have been concluded to be the most plausible processes limiting the progress of the Si_3N_4 degradation.

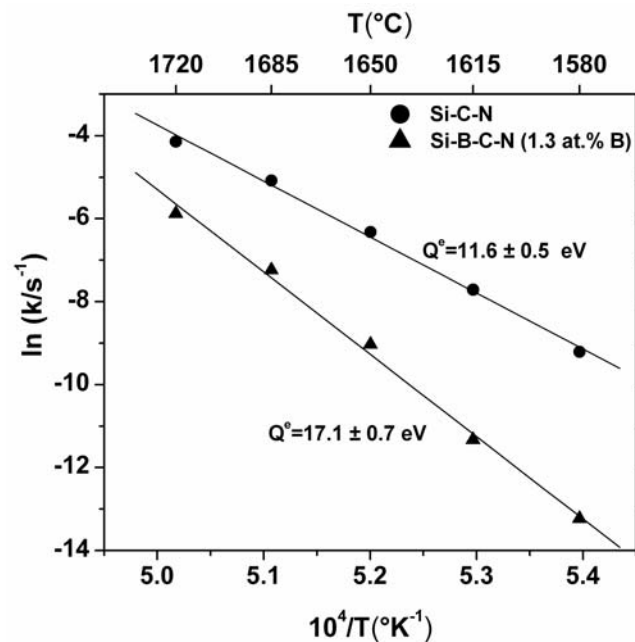


Fig. 7.5. Plot of the term $\ln(k)$, natural logarithm of the degradation rate constant, versus the reversible temperature for the Si–C–N and the Si–B–C–N (1.3 at.% B) ceramic. Solid straight lines represent a linear fit of the data. The slope of the fitted lines is proportional to the value of the effective activation energy Q° for the Si_3N_4 degradation.

* The kinetics of the Si_3N_4 degradation has been studied using a generalized model for the analysis of chemical reaction kinetics.

Zusammenfassung

8.1. Einleitung

Amorphe Festkörper in den Systemen Si-C-N und Si-B-C-N weisen eine herausragende thermische Beständigkeit gegen Kristallisation und chemische Zersetzung bis zu Temperaturen um 2000 °C auf. Diese Festkörper lassen sich aus polymeren Vorstufen erzeugen und werden in der angelsächsischen Literatur als Polymer-Derived Ceramics (PDCs) bezeichnet. Ein wesentlicher Parameter, der die thermische Beständigkeit dieser Materialien bestimmt, ist deren chemische Zusammensetzung. Dabei wird die thermische Beständigkeit durch den Einbau von Bor in ternäre Si-C-N-Festkörper wesentlich erhöht. Die Hochtemperaturstabilität dieser Keramiken hängt ebenfalls von strukturellen Umwandlungen ab. Dabei handelt es sich in erster Linie um Phasentrennungen, die bei Glühbehandlungen auftreten. Für eine Entwicklung von PDCs mit einer sehr guten thermischen Beständigkeit ist es demnach von großer Bedeutung, diese Separationen zu verstehen. Für eine quantitative Beschreibung dieser Phasentrennungen eignet sich das in Abb. 8.1 dargestellte Diagramm. Eine amorphe Si-C-N-Keramik mit einer Zusammensetzung SiC_aN_b innerhalb des Gebietes C-SiC-Si₃N₄ separiert demnach in Anteile aus amorphem Kohlenstoff und amorphen Domänen mit einer Zusammensetzung SiC_xN_b auf der Verbindungslinie SiC-Si₃N₄. Analog dazu separiert eine amorphe Si-B-C-N Keramik mit einer Zusammensetzung in der Region SiC-Si₃N₄-BN-C in die amorphen Phasen $(\text{BN})_c\text{C}_y$ und $\text{SiC}_{a-y}\text{N}_{b-c}$ mit Zusammensetzungen auf der C-BN- beziehungsweise SiC-Si₃N₄-Linie, was ebenfalls in Abb. 8.1 dargestellt ist. Diese Phasentrennung in der Mikrostruktur der Si-(B-)C-N PDCs stellt ein wesentliches Charakteristikum dieser Materialklasse dar und ist eng mit dem Anteil der einzelnen Komponenten verbunden. Bor ist dabei eine Schlüsselrolle zuzusprechen. Wie bereits erwähnt, finden sich in

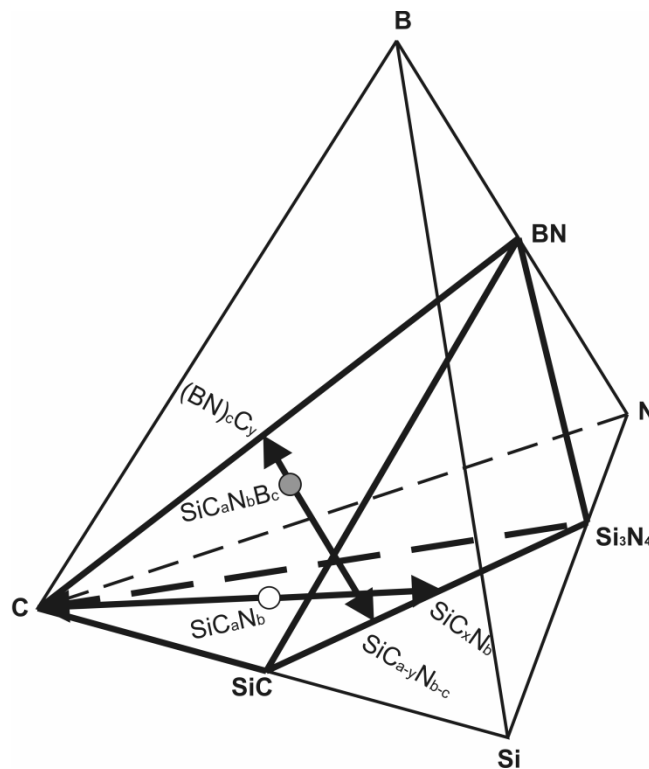


Abb. 8.1. Schematische Darstellung der Phasentrennungen in amorphen SiC_aN_b - und $\text{SiC}_a\text{N}_b\text{B}_c$ -PDCs.

diesen Materialien Si-C-N-Domänen, die aus $\text{SiC}_i\text{N}_{4-i}$ ($i = 0 - 4$) Struktureinheiten aufgebaut sind, in denen Siliciumatome sowohl an Kohlenstoff- als auch an Stickstoffatome gebunden sind. Der tetraedrische Aufbau dieser Struktureinheiten wurde mit Hilfe der NMR-Spektroskopie und der Röntgendiffraktometrie nachgewiesen. Eine solche Anordnung der Atome kann nicht durch übliches Sintern von keramischen Pulvern erreicht werden und ist damit das Hauptmerkmal von Polymer abgeleiteten Keramiken, die durch die Pyrolyse polymerer Vorstufen erhalten werden. Der Grund dafür sind kovalente Bindungen, welche entweder bereits im Polymer vorhanden sind oder sich während der Pyrolyse bilden.

Si-B-C-N PDCs zeigen außerdem ein besonderes Kristallisationsverhalten. Hierbei bilden sich SiC-Nanokristalle bei viel niedrigeren Temperaturen als die von Si_3N_4 . Die bemerkenswerte thermische Beständigkeit dieser amorphen Festkörper gegenüber einer Umwandlung in kristalline Phasen ist wesentlich durch die tetraedrischen Struktureinheiten, aus denen die separierten amorphen Si-C-N-Bereiche aufgebaut sind, bedingt. Der Grund für dieses Verhalten ist, dass die gemischten $\text{SiC}_i\text{N}_{4-i}$ -Tetraeder, aus denen diese Bereiche bestehen, weder in kristallines Siliciumnitrid noch

in Siliciumcarbid eingebaut werden können. Deswegen ist die vollständige Zersetzung dieser tetraedrischen Baueinheiten eine notwendige Bedingung für eine vollständige Kristallisation solcher Materialien. Trotz der Versuche, die thermische Beständigkeit von Si-(B-)C-N PDCs zu verstehen, fehlt es bislang an grundlegenden Untersuchungen, deren Hauptaugenmerk auf der Thermodynamik und der Kinetik der strukturellen Umwandlungen dieser Materialien liegt.

In dieser Doktorarbeit wurde zum ersten Mal die Thermodynamik und die Kinetik der Kristallisation der amorphen Si-(B-)C-N PDCs sowie die Zersetzung dieser Materialien, die nach der carbothermischen Reaktion ($\text{Si}_3\text{N}_4 + 3\text{C} \rightarrow 3\text{SiC} + 2\text{N}_2\uparrow$) abläuft, umfassend untersucht. Dabei wurde vor allem der Einfluss des Borgehaltes auf die strukturellen Veränderungen dieser Materialien betrachtet. Die erhaltenen Ergebnisse sind in 5 Kapiteln zusammengefasst (Kapitel 2 bis 6). Die Kapitel 2 bis 5 beschäftigen sich mit der Thermodynamik und der Kinetik der Kristallisationsvorgänge und in Kapitel 6 ist der Einfluss von Bor auf den Zersetzungsvorgang erläutert.

8.2. Thermodynamische Berechnungen

Thermodynamischen Berechnungen zum Hochtemperaturverhalten der Si-(B-)C-N PDCs wurden mit Hilfe der Software Thermo-Calc durchgeführt, um das Auftreten von Gleichgewichtsphasen abzuschätzen und den Temperaturbereich zu bestimmen, in dem diese Keramiken stabil sind. Desweiteren wurde der thermodynamische Einfluss von Bor auf die Triebkraft der Kristallisation sowie die Abfolge der einzelnen Zwischenstufen bei der Kristallisation aus dem amorphen Zustand betrachtet. Die Berechnungen beinhalten Phasenmengendiagramme, die die Gleichgewichtsphasen anzeigen (Kapitel 2, 3 und 6), die Gibbs Energien der amorphen Zustände, die Triebkräfte der Kristallisation (Kapitel 2) und eine Modellierung der metastabilen Phasengleichgewichte* (Kapitel 2).

* Dieses Modell basiert auf einer neuen Methode, die eine thermodynamische Beschreibung von SiC- und Si_3N_4 -Nanokristallen in Abhängigkeit von deren Größe ermöglicht. In dem hier verwendeten Modell wird zur Ableitung der freien Enthalpie einer nanokristallinen Phase eine Exzessenergie $\Delta G^{\text{ex}} = A/\langle d \rangle$ eingeführt, wobei A der Maximalwert der Exzessenergie ist, der mit der kleinsten mittleren nanokristallinen Dimension übereinstimmt. $\langle d \rangle$ ist die mittlere Kristallitgröße, die bei konstanter Heizrate von der Temperatur abhängt.

8.3. Experimentaltteil

Als Ausgangsmaterial für die experimentellen Untersuchungen wurde ein Polysilazan verwendet, das zu einer Keramik mit der Zusammensetzung $\text{SiC}_{1,4}\text{N}_{0,9}$ führt. In dieses Polymer wurden unterschiedliche Mengen Bor eingebracht. Diese Polymere wurden bei 1100 °C für 4 Stunden unter konstantem Argonfluss pyrolysiert, wodurch Si-B-C-N-Keramiken mit gleichem Si/C/N Verhältnis und einem Borgehalt von 1,3, 3,7, 6,0 und 8,3 at.% erhalten wurden. Laut den thermodynamischen Berechnungen liegt die Zusammensetzung des ternären Si-C-N-Materials innerhalb des 3-Phasengebietes C-SiC-Si₃N₄ und diejenige der quaternären Si-B-C-N-Keramik innerhalb des 4-Phasenraumes SiC-Si₃N₄-BN-C des ternären Si-C-N- bzw. quaternären Si-B-C-N-Systems. Die mittels Röntgendiffraktometrie durchgeführten Messungen zeigten zudem den amorphen Charakter der so erhaltenen Keramiken.

Der größte Teil dieser Arbeit beschäftigt sich mit röntgendiffraktometrischen Messungen der wärmebehandelten Proben. Anhand dieser Ergebnisse wurde der Volumenanteil der entstandenen kristallinen Phasen als Funktion der Glühzeit und der Temperatur bestimmt (Kapitel 3 bis 5). Zusätzlich zu der Röntgendiffraktometrie wurden weitere Untersuchungen mittels der Hochtemperaturthermogravimetrie (HT-TGA), Transmissionselektronenmikroskopie (TEM), energiegefilterten TEM (EFTEM) sowie der Rasterelektronenmikroskopie mit einer Feldemissionsquelle (REM) durchgeführt. Für die Elementaranalyse wurde die Plasma-Atomemissionsspektroskopie verwendet. Weitere Analysen beruhten auf dem Verbrennen des Materials und anschließender Quantifizierung der Produkte.

8.4. Ergebnisse und Diskussion

In Kapitel 2 ist das Kristallisationsverhalten von vier amorphen PDCs mit einem Borgehalt von 0, 3,7, 6,0 und 8,3 at.% beschrieben. Die thermodynamische Modellierung der amorphen Si-C-N Bereiche beweist, dass der Einbau von Bor die Triebkraft für die Kristallisation erhöht. Die experimentellen Ergebnisse befinden sich in Übereinstimmung mit den Resultaten der thermodynamischen Berechnungen und zeigen, dass der Borgehalt die Bildung von Nanokristalliten (SiC) fördert. Die Röntgendiffraktogramme der wärmebehandelten Proben verdeutlichen, dass sich SiC-

Nanokristallite in den borhaltigen Keramiken bei weitaus niedrigeren Temperaturen ($1300\text{ °C} \leq T \leq 1400\text{ °C}$) und geringeren Glühzeiten ($t \leq 2\text{ h}$) als Si_3N_4 -Nanokristallite ($T = 1650\text{ °C}$ und $t = 16\text{-}32\text{ h}$) bilden. Dieses Verhalten ist vom Borgehalt abhängig*. Die Kristallisation von Si_3N_4 und SiC tritt bei dem amorphen Material, das kein Bor enthält, bei 1400 °C nach 2 h auf. In dieser Arbeit konnte zusätzlich der Einfluss des Bors auf den Volumenanteil der α - und β -Modifikation des Si_3N_4 nachgewiesen werden. Das α/β -Verhältnis sinkt mit steigendem Borgehalt.

Kapitel 3 beschäftigt sich mit dem isochronen Kristallisationsverhalten der amorphen Keramik mit $8,3\text{ at.}\%$ B bei verschiedenen Heizraten ($1, 5$ und 25 K/min). Zur Analyse dieser Proben wurden die Röntgendiffraktogramme quantitativ analysiert und ein Modell, das eine Betrachtung der metastabilen Phasengleichgewichte beinhaltet, angewendet. Die Vorhersagen dieses Modells konnten in Bezug auf die Abfolge der nanokristallinen Zwischenstufen bei der Kristallisation aus dem amorphen Zustand experimentell bestätigt werden. Die Experimente zeigen, dass die Kristallisation von SiC bei Temperaturen oberhalb von 1300 °C beginnt. In der nächsten Stufe bilden sich Si_3N_4 -Nanokristallite zusammen mit weiteren SiC-Nanokristalliten. Diese zweite Stufe ist, je nach Heizrate, in dem Temperaturbereich zwischen 1800 °C und 1900 °C zu finden. Das zweistufige Kristallisationsverhalten der Si-B-C-N Keramik, die mit einer Heizrate von 25 K/min gegläht wurde, ist in Abb. 8.2 dargestellt. Metastabile Phasengendiagramme, welche aus dem oben genannten Modell erhalten wurden, zeigen ebenfalls einen zweistufigen Kristallisationsprozess. Als Beispiel sei hier Abb. 8.3 aufgeführt. Nach der Bildung von nanokristallinem SiC folgt eine eutektoid(artige) Umwandlung der restlichen Silicium haltigen amorphen Phase zu nanokristallinem SiC und Si_3N_4 .

Gegenstand der Kapitel 4 und 5 ist die umfangreiche kinetische Analyse[†] der Kristallisation von Si_3N_4 in Si-B-C-N-PDCs. Die Verwendung von Keramiken mit unterschiedlichen Borgehalten bietet hier die Möglichkeit, den Einfluss von Bor auf die

* Es ist bereits bekannt, dass die Kristallisation von Si_3N_4 mit steigendem Borgehalt bis $\sim 10\text{ at.}\%$ stark verzögert wird.

† Für die kinetische Analyse wurde die klassische Theorie für die Untersuchung von isothermen Phasenumwandlungen nach Johnson, Mehl, Avrami and Kolmogorov (JMAK-Theorie) verwendet.

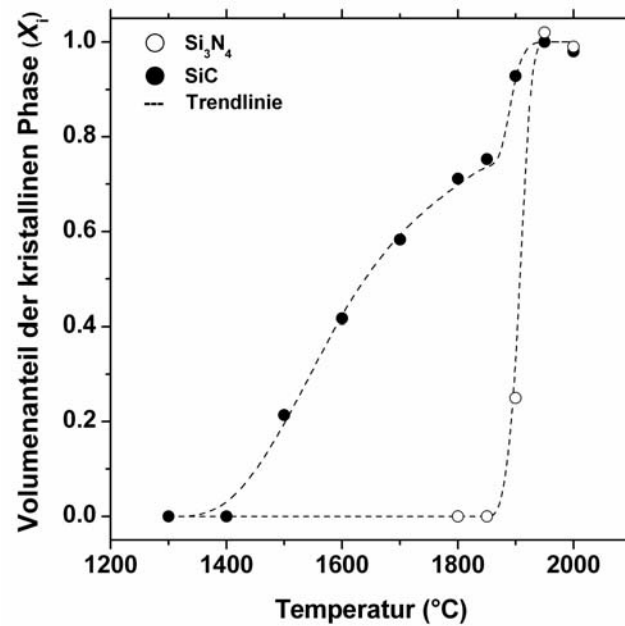


Abb. 8.2. Volumenanteil der kristallinen SiC und Si₃N₄ Phasen in Abhängigkeit von der Temperatur. Die Werte wurden mittels der quantitativen Röntgendiffraktometrie bestimmt. Bei der Probe handelt es sich um eine Si-B-C-N-Keramik mit einem Borgehalt von 8,3 at.%, die mit einer Heizrate von 25 K/min isochron gegläht wurde. Der Fehler wurde auf ±0,5 abgeschätzt.

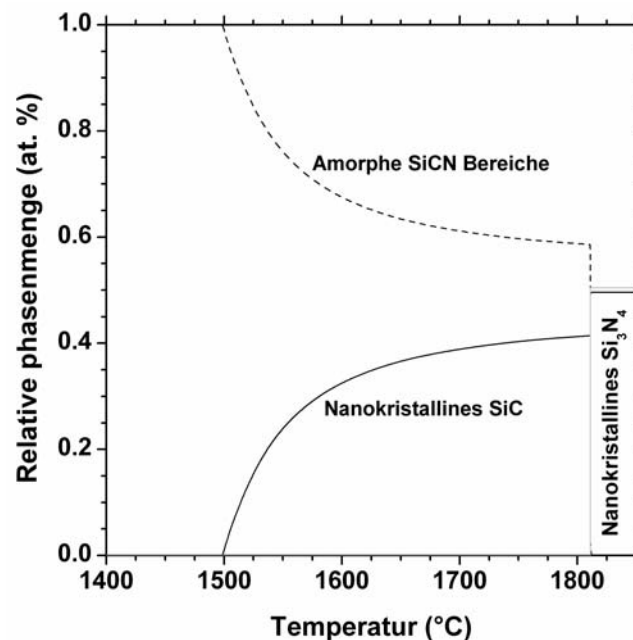


Abb. 8.3. Metastabiles Phasenmengendiagramm mit amorphen Si-C-N-Anteilen und den nanokristallinen Phasen SiC und Si₃N₄. Dieses Diagramm wurde mit dem Programm Thermo-Calc für eine Si-B-C-N Keramik mit einem Borgehalt von 8,3 at.% berechnet, welche mit einer Heizrate von 25 K/min gegläht wurde.

Kristallisationskinetik von Si_3N_4 zu untersuchen. Der wachsende Volumenanteil von kristallisiertem Si_3N_4 in den isotherm geglühten Proben wurde mittels Röntgendiffraktometrie bestimmt. Dabei konnte herausgefunden werden, dass die kontinuierliche Keimbildung der Kristallite der vorherrschende Mechanismus ist. Die gebildeten Kristallite wachsen anschließend 3-dimensional, wobei die Wachstumsgeschwindigkeit von der Volumendiffusion der Elemente Si und N in der amorphen Phase abhängig ist. Obwohl die erhaltenen Ergebnisse den Eindruck erwecken, dass der Kristallisationsvorgang unabhängig vom Borgehalt ist, zeigt sich der sehr große Einfluss dieses Elementes an den Aktivierungsenergien der Si_3N_4 -Kristallisation. Die jeweiligen Aktivierungsenergien wurden jeweils zu 7,8, 9,0 und 11,5 eV für die Keramiken mit einem Borgehalt von 3,7, 6,0 bzw. 8,3 at.% bestimmt (Abb. 8.4). Zusätzlich zeigen die erhaltenen Ergebnisse das annähernd gleiche Kristallisationsverhalten der α - und β -Modifikation von Si_3N_4 . Weiterhin wird deutlich, dass die Werte für die Aktivierungsenergien, die der Keimbildung zugeordnet werden können, weitaus größer als die Werte sind, die zum Wachstumsprozess gehören.

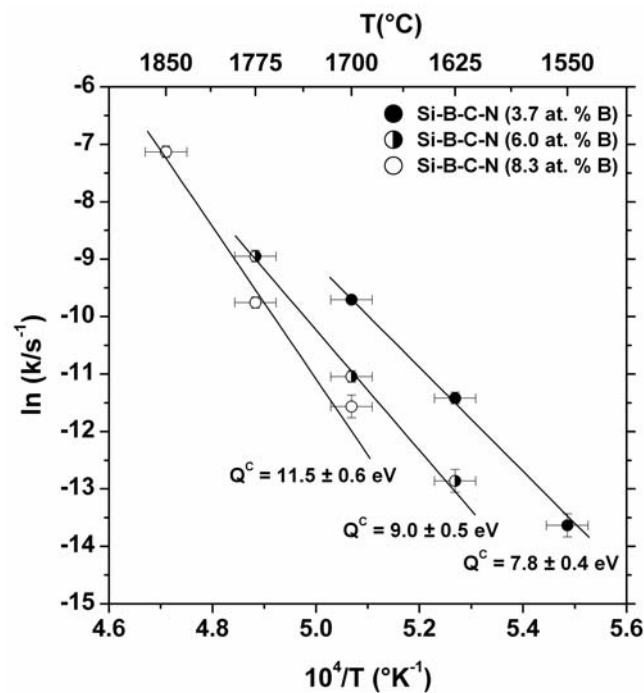


Abb. 8.4. In diesem Diagramm ist der natürliche Logarithmus der Kristallisationskonstante ($\ln(k)$) gegen den Kehrwert der Temperatur für Keramiken mit unterschiedlichen Borgehalten aufgetragen. Die Steigungen der angepassten Linien sind proportional zu der Aktivierungsenergie der Kristallisation Q^c .

Damit ist der Keimbildung eine wichtige Rolle für das Fortschreiten der Kristallisation zuzuschreiben, deren Aktivierung mit zunehmendem Borgehalt auch mehr Energie benötigt.

In Kapitel 6 ist der kinetische Einfluss von Bor auf die chemische Stabilität von Si-(B-)C-N-PDCs diskutiert. Die chemische Stabilität hängt ausschließlich von der carbothermischen Reaktion von Si_3N_4 (Si_3N_4 -Zersetzung, s. o.) ab. Diese Reaktion führt demnach zu einem Masseverlust der Keramiken. Deswegen wurde der isotherme Masseverlust der Keramik ohne Bor und der Keramik, die 1,3 at.% Bor enthält, als Funktion der Zeit gemessen. Die Messungen wurden mittels der thermogravimetrischen Analyse bei verschiedenen Temperaturen durchgeführt. Die Ergebnisse der kinetischen Analyse* beweisen, dass Bor sowohl die effektive Aktivierungsenergie als auch den Mechanismus der Zersetzung stark beeinflusst. In diesem Zusammenhang wurde die Aktivierungsenergie des Zersetzungsvorganges bei der Si-C-N Keramik auf $11,6 \pm 0,5$ eV und für die Si-B-C-N Keramik auf $17,1 \pm 0,7$ eV abgeschätzt, was in Abb. 8.5

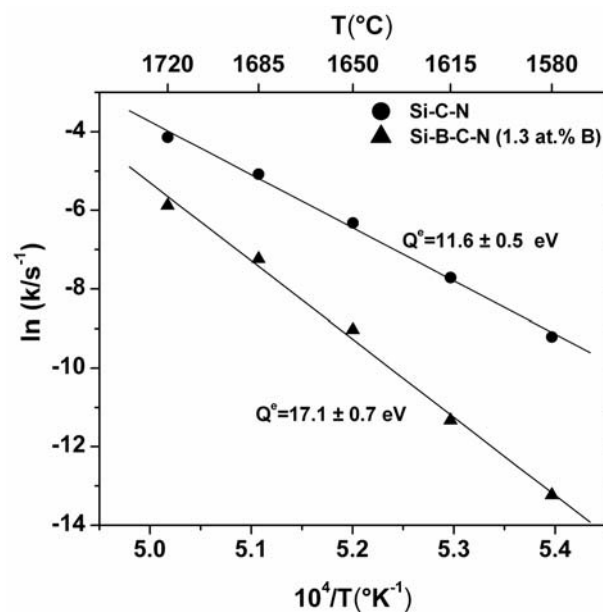


Abb. 8.5. In diesem Diagramm ist der natürliche Logarithmus der Zersetzungskonstante ($\ln(k)$) gegen den Kehrwert der Temperatur für die Si-C-N Keramik und der Si-B-C-N Keramik mit einem Borgehalt von 1,3 at.% aufgetragen. Die Steigungen der angepassten Linien sind proportional zu der effektiven Aktivierungsenergie Q° der Zersetzung von Si_3N_4 .

* Die Geschwindigkeit der Zersetzung von Si_3N_4 wurde mit einem allgemeinen Modell untersucht, das für die Beschreibung von chemischen Reaktionsgeschwindigkeiten verwendet wird.

dargestellt ist. Die Daten legen nahe, dass in dem Bor freien Material die Reaktion an der Oberfläche zwischen Si_3N_4 und C oder/und die Bildung von SiC geschwindigkeitsbestimmend für die Zersetzung von Si_3N_4 sind. In der Bor haltigen Keramik sind die lokale Diffusion von Kohlenstoff aus den turbostratischen BNC_x -Strukturen, welche die Si_3N_4 Nanokristalle umgeben sowie das Entweichen des Gases (N_2) aus der Reaktionszone die wahrscheinlichsten Prozesse, die die Zersetzung von Si_3N_4 vorantreiben.

Acknowledgements

The research presented in this thesis has been carried out at the Institute for Materials Science in the University of Stuttgart and at the Max Planck Institute for Metals Research. I wish to take this opportunity to thank those who have been involved and contributed toward the accomplishment of this work.

I would like to express my sincere gratitude to my supervisor Prof. Dr. J. Bill who introduced me to the field of polymer-derived ceramics and continuously supported me throughout this work. His insights and constructive comments have provided a good basis for this research. It has been an honor to work with him.

Beside my supervisor, I wish to express my deep appreciation to two other members of my PhD examination: Prof. Dr. G.D. Sorarù and Prof. Dr. E.J. Mittemeijer for reviewing my PhD thesis and making constructive comments on this research.

My cordial gratitude goes to my co-supervisor Dr. J.A. Golczewski for supporting and encouraging me at every stage of my challenging research even after his retirement. His broad knowledge and his logical way of thinking have been of great value for me. I warmly acknowledge his stimulating scientific discussions as well as his substantial help for the thermodynamic computations.

I am also grateful to Tobias Lehman for translating the summary of this thesis to German.

I would like to extend my thanks to all the friends and colleagues at the Max Planck Institutes in Stuttgart and all the coworkers who helped me with my work in the past three years.

Financial supports by the European Community's Sixth Framework Program through a Marie Curie Research Training Network and International Max Planck Research School for Advanced Materials are highly appreciated.

Finally, I would like to express special thanks to my beloved wife Mona, my parents and my sisters. The encouragement and support from them is a powerful source of inspiration and energy.

List of publications

1. A.H. Tavakoli and M. Goodarzi, “*Effect of Mechanical Activation on Carbothermic Synthesis of Titanium Carbide from Ilmenite Concentrate*”, Iranian J. Mater. Sci. and Eng. 1[3] (2004) 22.
2. A.H. Tavakoli, S.M. Seyed Reihani and A. Simchi, “*Effect of Cyclic Compaction on Consolidation of Al/SiC Composite Powders*”, Proceeding of 4th World Congress of Powder Metallurgy (PM 2004), Vienna–Austria (2004) 599.
3. A.H. Tavakoli, S.M. Seyed Reihani and A. Simchi, “*Forming of Metal Matrix Powder Composites with Cyclic Loading*”: in Persian, Proceeding of 2nd Iranian Congress of Metals & Materials Forming (Matform’83), Tehran–Iran (2004) 293.
4. A.H. Tavakoli, A. Simchi and S.M. Seyed Reihani, “*Study of the Compaction Behavior of Composite Powders under Monotonic and Cyclic Loading*”, Composites Sci. and Tech., 65 (2005) 2094.
5. A.H. Tavakoli, J.A. Golczewski, J. Bill, “*Decomposition and Crystallization: Thermal Stability*”, in “*Polymer Derived Ceramics*: P. Colombo, R. Riedel, G.D. Soraru, A. Kleebe (Eds.)”, 1st edition, DEStech Publications, USA, 2010 (chapter 1 of the thesis).
6. A.H. Tavakoli, P. Gerstel, J.A. Golczewski and J. Bill, “*Effect of Boron on Crystallization of Amorphous Si–(B–)C–N Polymer-Derived Ceramics*”, J. Non-Cryst. Solids 355 (2009) 2381 (chapter 2 of the thesis).
7. A.H. Tavakoli, P. Gerstel, J.A. Golczewski and J. Bill, “*Quantitative X-ray Diffraction Analysis and Modeling of Crystallization in Amorphous Si–B–C–N Polymer-Derived Ceramics*”, J. Am. Ceram. Soc. 93 (2010) 1470 (chapter 3 of the thesis).
8. A.H. Tavakoli, P. Gerstel, J.A. Golczewski and J. Bill, “*Crystallization Kinetics of Si₃N₄ in Si–B–C–N Polymer-Derived Ceramics*”, J. Mater. Res. in press, DOI:101557/JMR.2010.0282 (chapter 4 of the thesis).
9. A.H. Tavakoli, J.A. Golczewski and J. Bill, “*Kinetic Effect of Boron on the Crystallization of Si₃N₄ in Si–B–C–N Polymer-Derived Ceramics*”, Accepted for publication in J. Mater. Res. (chapter 5 of the thesis).
10. A.H. Tavakoli, J.A. Golczewski and J. Bill, “*Kinetic Effect of Boron on the Thermal Stability of Si–(B–)C–N Polymer-Derived Ceramics*”, Acta Mater. 58 (2010) 6002 (chapter 6 of the thesis).

Curriculum Vitae

Personal information

Name: Amir Hossein Tavakoli
Date and Place of Birth: 19.09.1980, Tehran, Iran
Nationality: Iran
E-mail: a.h.tavakoli@mf.mpg.de, a.h.tavakoli@gmail.com

Education

July 2007 – Oct. 2010 **Ph.D. in Materials Science**
Institute for Materials Science, University of Stuttgart and Max
Planck Institute for Metals Research, Stuttgart, Germany

Sept. 2002 – March 2004 **M.S. in Materials Science and Engineering**
Sharif University of Technology, Tehran, Iran
GPA: 18.03 of 20

Sept. 1998 – Sept. 2002 **B.S. in Materials Science and Engineering**
Iran University of Science and Technology, Tehran, Iran
GPA: 16.74 of 20

July 1998 **Diploma of High School in Mathematical and Physical
Sciences**
Shahid Motahari High School, Tehran, Iran

